

WASHINGTON UNIVERSITY IN ST. LOUIS
Department of Physics

Dissertation Examination Committee:
Kater Murch, Chair
James Buckley
Erik Henriksen
Zohar Nussinov
Jung-Tsung Shen

Partial Measurements of Quantum Systems
by
Jonathan Tyler Monroe

A dissertation presented to
The Graduate School
of Washington University in
partial fulfillment of the
requirements for the degree
of Doctor of Philosophy

May 2021
St. Louis, Missouri

© 2021, Jonathan Tyler Monroe

Table of Contents

List of Figures	v
List of Tables	vii
Acknowledgments	viii
Abstract	xi
Chapter 1: Introduction	1
1.1 Motivation.....	1
1.2 Quantum Mechanics with Circuits	4
1.2.1 Quantizing the cavity	4
1.2.2 Quantizing the LC Circuit	7
1.2.3 Quantizing the Nonlinear LC	8
1.3 Readout Physics	9
1.3.1 Jaynes-Cummings Interaction.....	10
1.3.2 Partial Measurements	14
Chapter 2: Direct-Write Qubits	18
2.1 Introduction.....	18
2.2 Fabrication Theory.....	20
2.2.1 Josephson Junction Nonlinearity	20
2.2.2 Josephson Relations from BCS Theory.....	22
2.2.3 Cabrera-Mott Oxidation Model	23
2.3 Recipe Development	28
2.3.1 Design-of-Experiment Philosophy.....	28
2.3.2 Resist Exposure Tuning	29
2.3.3 Junction Consistency Tests.....	35

2.3.4	Full Recipe	39
2.4	Devices	43
2.4.1	Structure of Large-Area Junctions	44
2.4.2	Circuit Spectroscopy	48
2.4.3	Time Domain Measurements	52
2.4.4	Additional Noise Sources	56
2.4.5	Limits on Loss Tangents.....	57
Chapter 3:	Entropic Uncertainty Relations.....	58
3.1	Introduction.....	58
3.1.1	Problems with Variance-based Uncertainty Relations	59
3.1.2	Entropic Uncertainty Relations.....	60
3.2	Theory.....	63
3.2.1	Trivial Bound	64
3.2.2	Deutsch Bound	65
3.2.3	Maassen-Uffink Bound	66
3.2.4	Tomamichel Bound	67
3.2.5	Weak Measurement Bound	67
3.3	Experiment	70
3.3.1	Entropies of the Entropic Uncertainty Relation.....	71
3.3.2	Bound of the Entropic Uncertainty Relation.....	81
3.3.3	Combing Elements of the RHS	85
Chapter 4:	Time-Reversed Feedback	88
4.1	Introduction.....	88
4.2	Stochastic Thermodynamics	90
4.2.1	Classical Fluctuation Theorems	90
4.2.2	Thermodynamics of Quantum Trajectories.....	96
4.3	Experiment	98
4.3.1	Setup	98
4.3.2	Trajectory probabilities.....	101
4.3.3	Fluctuation Theorems.....	103

4.4 Conclusion.....	107
Bibliography	108

List of Figures

Figure 1.1: Jaynes-Cummings Hamiltonian Eigenenergies	12
Figure 2.1: Cabrera Theory	26
Figure 2.2: Exposure Test for S1805	30
Figure 2.3: Resist Stack Imaging	32
Figure 2.4: Codename Sandwich Factorial Design.....	33
Figure 2.5: Resistance Variation from Area Variation.....	35
Figure 2.6: Variation in Manhattan Evaporation	36
Figure 2.7: Wafer Variation with Improved Softbaking	38
Figure 2.8: SEM image of a Large-area Junction	44
Figure 2.9: Preparing TEM Sample.....	45
Figure 2.10: EDXS Data for Multi-layer Junction	46
Figure 2.11: Resistance Scaling with Oxide Thickness.....	47
Figure 2.12: High Power Spectroscopy	49
Figure 2.13: TLS in Spectroscopy	51
Figure 2.14: T_1 vs Flux and Time.....	53
Figure 2.15: Quality Factor Histograms	55
Figure 2.16: Quality Factor Aging	56
Figure 3.1: Pulse sequence for measuring entropies	71
Figure 3.2: Measurement Angles.....	72
Figure 3.3: Projective measurement entropies.....	74
Figure 3.4: Entropy in the Presence of Weak Measurement	76

Figure 3.5: Entropy Under the Influence of Weak Measurement	78
Figure 3.6: Entropies of the Entropic Uncertainty Relation	80
Figure 3.7: RHS Components.....	82
Figure 3.8: Weak Value Measurement Protocol.....	83
Figure 3.9: Weak Values	84
Figure 3.10: RHS of Entropic Uncertainty Relation.....	87
Figure 4.1: Readout Distributions.....	99
Figure 4.2: Correlated Tomography.....	101
Figure 4.3: Feedback Protocol.....	105
Figure 4.4: Entropy Histograms.....	106

List of Tables

Table 3.1: Select values of $H(AF)_\rho$	81
--	----

Acknowledgments

I am delighted to thank the many people who have guided and supported me during my graduate studies. The bountiful support of those close to me filled my experience with joy.

I begin with the central driver of my success: Kater Murch. I count myself exceptionally fortunate to have been mentored by such a personable and passionate advisor as Kater. Kater's example has instilled the virtue of clear explanations.

I feel honored to have worked among such great colleagues in the Murch lab. I thank Dian Tan for his patient tutelage of fabrication techniques and Mahdi Naghiloo for his willing explanation of every aspect of our lab, especially as codified in his dissertation. Patrick Harrington has been an inspiring figure in my life. I admire his profound insights, and I feel deep appreciation to have worked and played with him for four years. I appreciate the varied insights and passions of Maryam Abassi, Taeho Lee, Xingrui Song, Yungzhao Wang, and Weijian Chen. Working closely with Daria Kowsari, Chandrashekhar Gaikwad, and Kaiwen Zheng has engendered passion and devotion. Thank you all for being such excellent scientists and sharing your experiences.

I am grateful for my committee's helpful guidance and feedback. I particularly thank Henric Krawczynski and Zohar Nussinov for their continued mentorship throughout my graduate

tenure. I thank Jim Buckley, Erik Henricksen, and JT Shen for their eager willingness to read my dissertation.

I thankfully acknowledge the critical roles of Todd Hardt, Linda Trowler, and Sarah Akin played in supporting my graduate work. Thank you for maintaining infrastructure that makes the ship run smoothly. I thank Rahul Gupta for training me on equipment and working hard to maintain high cleanroom standards.

I am grateful for a cohort of colleagues who have enriched life during grad school. Kiandohkt Amiri, Jesse Balgley, Natália Calleya, Furqan Dar, and Kainen Utt have been dear friends to commensurate and celebrate with.

Finally, I would not have thrived during my graduate career without the endless love and support of Esther. Thank you for keeping me happy and healthy; I am elated for our future.

Thank you all.

Jonathan Tyler Monroe

Washington University in Saint Louis

May 2021

Dedicated to E. Monroe

ABSTRACT OF THE DISSERTATION

Partial Measurements of Quantum Systems

by

Jonathan Tyler Monroe

Doctor of Philosophy in Physics

Washington University in St. Louis, 2021

Professor Kater Murch, Chair

Projective measurement is a commonly used assumption in quantum mechanics. However, advances in quantum measurement techniques allow for partial measurements, which accurately estimate state information while keeping the wavefunction intact. We employ partial measurements to study two phenomena. First, we investigate an uncertainty relation—in the style of Heisenberg’s 1929 thought experiment—which includes partial measurements in addition to projective measurements. We find that a weak partial measurement can decrease the uncertainty between two incompatible (non-commuting) observables. In the second study, we investigate the foundation of irreversible dynamics resulting from partial measurements. We do so by comparing the forward and time-reversed probabilities of measurement outcomes resulting from post-selected feedback protocols with both causal and reversed-causal order. We find that the statistics of partial measurements produce entropy in accordance with generalized second laws of thermodynamics.

We perform these experiments using superconducting qubits. We describe the fabrication process for these devices and detail a novel fabrication technique that allows fast, single-step lithography of Josephson-junction-based superconducting circuits. The technique simplifies processing by utilizing a direct-write photolithography system, in contrast to traditional

electron-beam lithography. Despite their large lithographic area, Josephson junctions made with this method have low critical currents and high coherence times.

Chapter 1

Introduction

1.1 Motivation

Quantum mechanics offers a strange view of reality when compared to the classical world. Particles can occupy distinct states simultaneously, and measuring a system changes what the system does. These phenomena would be bizarre in an everyday setting, but they are routine in quantum mechanics.

The concept of measurement backaction is especially intriguing. In our everyday experience, our measurements do not disturb the quantity we're measuring: No table has ever been widened by measuring its length. Yet monitoring a quantum particle's trajectory irrevocably changes its momentum, injecting fundamental uncertainty about the particle's dynamics.

Introductory quantum mechanics posits that particles are described by a wavefunction composed of complex amplitudes. Yet when we measure one of the particle's properties, say

its position, we get a single, real number. This classical information neglects a great deal of the particle's state.

What is so special about measurement that forces us to discard so much in bridging the quantum-classical divide? The measurement apparatus must have been made up of particles described by their own quantum wavefunctions. The measurement process must have involved an interaction between the apparatus and the system. Both of these statements are well described by quantum mechanics. Where did the quantum information go?

The answer, in part, is that decoherence often rapidly distributes the quantum information throughout a wavefunction with many possible outcomes [1]. The system-apparatus interaction can cause the system's information to dissociate into distant components of the apparatus. After the apparatus has completed the measurement, it continues to interact with its environment, and the state's information quickly erodes completely. But decoherence is not an insurmountable challenge.

In systems with manageable decoherence, the quantum nature of measurement emerges. Optics experiments were among the first to directly observe the continuous collapse of a system's wavefunction [2]. With modern circuit quantum electrodynamics (cQED) experiments, quantum trajectories under the influence of measurement have been directly observed [3, 4, 5, 6], even under the influence of multiple, non-commuting measurements [7, 8].

In cQED, the microwave frequency range provides a timescale that is arguably as slow as possible to provide a view of quantum dynamics. If the dynamics were slower (corresponding to lower frequencies), the thermal energy at 10 mK (the coldest temperature readily achieved with dilution refrigerators) would dominate the quantum energy scale.

With this in mind, the cQED platform has provided a remarkable view of quantum phenomena. In particular, cQED experiments have directly observed quantum jumps, especially during spontaneous emission [9, 10, 11, 12]. Moreover, in some situations, these jumps provide warning signs before they occur so that low-latency feedback controllers can reverse a jump while it is occurring [13].

Access to the continuous measurement process often comes with the ability to turn the measurement off. In such a case, the quantum system may be partially measured. A system's free-evolution can be interrupted by a partial interrogation before continuing its free evolution. Combined with unitary control of the system, partial measurements provide an excellent tool for control [14, 15], measurement-based feedback both in real-time [16, 17], and autonomously [18, 19].

A particularly fascinating use case for partial measurements is when the partial measurement occurs between two fully projective measurements. The state begins in a pre-selected eigenstate (i.e. protectively measured) and evolves under the presence of a weakly coupled apparatus. The system is then fully projected onto a different eigenstate. The pre- and post-selected expectation value called a weak value [20]. The weak value has excited debate across theory and experiment [21, 22, 23, 24, 25]. Most remarkably, the magnitude of weak values can exceed the spectrum of the measurement operator [26]. For example, a spin-1/2 operator (whose spectrum is $[-1, 1]$) can have an anomalous weak value of greater than 1.

Thus, weak measurements provide unique views into quantum dynamics. In this thesis, we explore the statistics of weak measurement from two perspectives. First, we look at how weak measurements affect uncertainty relations governing incompatible observables, similar to position and momentum. We find that a weak measurement can reconcile the two observables, through the action of the weak value. Second, we look at the reversibility (or lack thereof) of

the wavefunction collapse process. In the process, we identify essential features of entropy generation in accordance with a generalization of the second law of thermodynamics.

1.2 Quantum Mechanics with Circuits

In this section, we describe the quantum nature of superconducting circuits. We begin by first quantizing the electromagnetic fields of a microwave cavity, then we quantize the modes of a linear and a nonlinear LC oscillator.

1.2.1 Quantizing the cavity

In this section, we describe the quantization of a single mode of the electromagnetic (EM) field. The quantum mechanical analysis of the classical equations of motion results in the quantum harmonic oscillator.

Classical EM theory centers on Maxwell's equations, which can be written using the vector potential, \vec{A} :

$$\left(\nabla^2 - \frac{1}{c^2}\partial_t^2\right)\vec{A} = 0. \quad (1.1)$$

We have chosen the Coulomb gauge, $\nabla \cdot \vec{A} = 0$ so that the magnetic and electric fields may be written as:

$$\vec{E} = -\partial_t \vec{A} \quad (1.2a)$$

$$\vec{B} = \nabla \times \vec{A}. \quad (1.2b)$$

The EM mode we focus on is the fundamental mode of a three-dimensional microwave cavity [27]. The linearity of this system and EM theory allows us to perform separation of variables on the vector potential: $A(\vec{r}, t) = f(\vec{r}) \alpha(t)$. Considering a single mode of frequency ω allows us to calculate $\vec{E} = -i\omega f(\vec{r}) \alpha(t)$. The spatial extent of the fields is set by $f(\vec{r})$, while the temporal variation is set by $\alpha(t)$.

Quantizing EM fields involves quantizing their Hamiltonian. Consider the pseudo¹ position and momentum coordinates,

$$p(t) = -\omega\epsilon_0(\alpha(t) + \alpha^*(t)) \quad (1.3)$$

$$q(t) = -i(\alpha(t) - \alpha^*(t)), \quad (1.4)$$

defined so that $p = \epsilon_0 \partial_t q$. We suppress the time-dependence for notational compactness. We can use these conjugate variables to transform the classical EM Hamiltonian:

$$\begin{aligned} H_{\text{EM,c}} &= \frac{\epsilon_0}{2} \int dV \left(|\vec{E}|^2 + \omega^2 |\vec{A}|^2 \right) \\ &= 2\epsilon_0 \omega^2 |\alpha|^2 \\ &= \frac{p^2}{2\epsilon_0} + \frac{\epsilon_0}{2} \omega^2 q^2. \end{aligned} \quad (1.5)$$

To more easily represent the above harmonic oscillator Hamiltonian, we use the creation and annihilation operators:

$$\begin{aligned} p &= i\sqrt{\frac{\epsilon_0 \hbar \omega}{2}} (a^\dagger - a) \\ q &= \sqrt{\frac{\hbar}{2\epsilon_0 \omega}} (a + a^\dagger). \end{aligned} \quad (1.6)$$

¹The term pseudo refers to the fact that the effective mass which links p and q is the permittivity of free space, ϵ_0 , and that the spatial extent of the field (given by $f(\vec{r})$) is independent of p and q .

Comparing to the quantum harmonic oscillator (QHO) Hamiltonian allows us to identify a quantization procedure to translate from classical to quantum descriptions:

$$\alpha(t) \rightarrow i\sqrt{\frac{\hbar}{2\epsilon_0\omega}} a, \quad (1.7)$$

where a is the typical creation operator whose explicit time dependence is understood in the Heisenberg picture [28].

The Hamiltonian of a single mode of the quantum mechanical EM fields thus becomes the QHO Hamiltonian:

$$H_{\text{EM,q}} = H_{\text{QHO}} = \hbar\omega\left(a^\dagger a + \frac{1}{2}\right) \quad (1.8)$$

We can also use Equation [1.7] and Equations [1.2] to identify the EM field operators:

$$\begin{aligned} E &= -\sqrt{\frac{\hbar\omega}{2\epsilon_0}} f(\vec{r}) (a + a^\dagger) \\ B &= i\sqrt{\frac{\hbar}{2\epsilon_0\omega}} [\nabla \times f(\vec{r})] (a - a^\dagger) \end{aligned} \quad (1.9)$$

The spatial extent of the fields retains its classical component unaffected. Thus, standard classical EM calculations lead to the spatial extent of quantum mechanical EM fields. In particular, quantum mechanical modes of complex EM structures are readily simulated with finite element modeling [29]. Our analysis will primarily focus on the Hamiltonian form of the field from Equation [1.8].

1.2.2 Quantizing the LC Circuit

Having quantized the EM field inside the cavity, we now describe how to attain a qubit out of a quantized circuit. Circuit quantization, like EM field quantization, has the structure of the quantum harmonic oscillator.

The central circuit of interest is an LC oscillator. The state of the LC oscillator is defined in terms of the circuit's current, I , and voltage, V . We transform these variables to get a canonically conjugate pair of variables. The voltage relates to the total charge, q , on the capacitor (with capacitance C):

$$V = \frac{q}{C}, \quad (1.10)$$

The current relates to the branch flux, ϕ , passing through the inductor (with inductance L):

$$\phi = \int_{-\infty}^t V(t') dt' = I L. \quad (1.11)$$

The capacitor contributes charging energy $q^2/2C$, while the inductor contributes inductive energy $\phi^2/2L$. Thus the Hamiltonian is given by:

$$H = \frac{q^2}{2C} + \frac{\phi^2}{2L}. \quad (1.12)$$

The connection between the classical harmonic oscillator Hamiltonian above and the QHO Hamiltonian from Section 1.2.1 suggests a similar variable transformation as Equation 1.7. We define raising and lowering operators for the quantized LC oscillator via:

$$\begin{aligned} \phi &= \phi_{\text{ZPF}} (a + a^\dagger) \\ q &= i q_{\text{ZPF}} (a^\dagger - a), \end{aligned} \quad (1.13)$$

where $\phi_{\text{ZPF}} = \frac{\hbar Z}{2}$ and $q_{\text{ZPF}} = \frac{\hbar}{2Z}$ are the magnitudes of quantum zero-point fluctuations for the two operators with $Z = \sqrt{\frac{L}{C}}$. The operators obey the commutation relation $[\phi, q] = i\hbar$. With this representation, the LC oscillator also obeys the QHO Hamiltonian (Eqn. [1.8]).

1.2.3 Quantizing the Nonlinear LC

The LC oscillator described in the previous section has evenly spaced energy levels. To obtain a uniquely addressable qubit, the harmonic spacing must be broken. The non-linearity of a Josephson junction (JJ) provides a circuit with anharmonic energy levels.

A Josephson junction is composed of two superconductors separated by an insulating barrier. As described in Section 2.2.2, JJs have a nonlinear inductance given by

$$L_{\text{JJ}} = \frac{I_0}{2\pi\Phi_0 \cos \phi}, \quad (1.14)$$

where ϕ is the difference between the two superconductors' phases, I_0 is a fabrication-dependent critical current, and $\Phi_0 = h/2e$ is the flux quantum.

The JJ contributes inductive energy

$$U_{\text{JJ}} = \int V(t') I dt' = \frac{\Phi_0 I_0}{2\pi} (1 - \cos \phi) = E_J (1 - \cos \phi), \quad (1.15)$$

where we have defined the Josephson energy as $E_J = \frac{\Phi_0 I_0}{2\pi}$. The JJ also contributes small capacitive energy which depends on the JJ's geometry. So the Hamiltonian of the nonlinear LC circuit is:

$$H = \frac{q^2}{2C} - \frac{\Phi_0 I_0}{2\pi} \cos \phi = 4E_C n^2 - E_J \cos \phi. \quad (1.16)$$

We have represented the charge variable with the number of cooper pairs, n , (each having charge $2e$). We have defined $E_C = \frac{e^2}{2C_\Sigma}$ as the charging energy per electron with capacitance $C_\Sigma = C_{\text{shunt}} + C_{\text{JJ}}$ is the contribution from both the shunt capacitance as well as the JJ's capacitance.

Equation [1.16] has an exact solution that depends on Mathieu's characteristic value [30]. Because we will focus on the lowest energy levels where the ϕ variable is well-localized, we can Taylor expand the cosine potential:

$$H = 4E_C n^2 + \frac{E_J}{2}\phi^2 - \frac{E_J}{24}\phi^4. \quad (1.17)$$

The first two terms recreate the LC Hamiltonian, and the last term provides the required anharmonicity. In the transmon limit, $E_J/E_C \gg 1$, the first transition frequency is $\omega_{01} = \sqrt{8E_J E_C} - E_C$, the anharmonicity is $-E_C$, and charge noise is exponentially suppressed in E_J/E_C . The anharmonicity allows us to truncate the energy levels to the first two, which we use as our qubit.

1.3 Readout Physics

This section describes the measurement process for our quantum circuits. The cQED architecture utilizes cavity (or generic EM resonator) modes as an auxiliary quantum system to readout the qubit state. To measure the qubit, the qubit's state information first imprints onto the cavity's state, and then the cavity's state is measured.

1.3.1 Jaynes-Cummings Interaction

The Jaynes-Cummings (JC) Hamiltonian describes a common interaction between an atom and a cavity. The cavity state is described by creation and annihilation operators, a and a^\dagger . We consider two levels of the atom and adopt the familiar pseudo-spin-1/2 notation where the operator σ_z acts on the state in the energy basis. With this, the atom may be treated as a qubit. The total Hamiltonian is composed of three constituent Hamiltonians:

$$H_{\text{cav}} = \hbar\omega_c \left(a^\dagger a + \frac{1}{2} \right) \quad (1.18)$$

$$H_{\text{atom}} = \hbar \frac{\omega_q}{2} \sigma_z \quad (1.19)$$

$$H_{\text{int}} = \vec{E} \cdot \vec{d} \quad (1.20)$$

In the JC model, the cavity and atom couple with a dipole interaction between the cavity's electric field, \vec{E} , and the atom's dipole operator, \vec{d} .

The cavity's electric field operator was calculated in Section 1.2.1. The result is

$$\vec{E} = -\sqrt{\frac{\hbar\omega_c}{2\epsilon_0}} [f(\vec{r}) a + \text{h.c.}] \quad (1.21)$$

The spatial dependence, $f(\vec{r})$ is classical and presumed real, but the time dependence (through the Heisenberg picture of a) is quantum mechanical [27].

The atom's dipole operator is

$$\vec{d} = \vec{d}_{01} (|0\rangle \langle 1| + |1\rangle \langle 0|) = \vec{d}_{01} (\sigma + \sigma^\dagger), \quad (1.22)$$

where $\vec{d}_{01} = \langle 0|(-e)\vec{r}|1\rangle$ is the dipole matrix element which depends on the dipole's position vector, \vec{r} , the fundamental charge e , and is presumed real. The coupling operates on the atom with $\sigma = \sigma_x + i\sigma_y$, which merely exchanges ground and excited states. Evaluating the dot product between \vec{E} and \vec{d} produces a coupling rate, $\hbar g = -\sqrt{\frac{\hbar\omega_c}{2\epsilon_0}} \vec{d}_{01} \cdot f(\vec{r})$.

Combing the atom, field, and interaction Hamiltonians produces the JC Hamiltonian:

$$H_{\text{JC}}/\hbar = \omega_c \left(a^\dagger a + \frac{1}{2} \right) + \frac{\omega_q}{2} \sigma_z + g(a + a^\dagger)(\sigma + \sigma^\dagger). \quad (1.23)$$

The rotating wave approximation (RWA) replaces high-frequency terms with their average over the time scale set by the interaction rate. The approximation is not valid when the cavity photon number is high. The RWA approximation results in a new JC Hamiltonian:

$$H_{\text{JC}}^{(\text{RWA})}/\hbar = \omega_c \left(a^\dagger a + \frac{1}{2} \right) + \frac{\omega_q}{2} \sigma_z + g(a\sigma^\dagger + a^\dagger\sigma). \quad (1.24)$$

From comparing Equations [4.22] and [1.24], the neglected high-frequency terms correspond to two-excitation processes, such as $a\sigma$ which annihilate one excitation in each of the cavity and atom.

Because a acts on an infinite-dimensional Hilbert space, finding energy eigenvalues of Equation 1.24 can be challenging. Fortunately, the Hamiltonian is block-diagonal and can be solved analytically. See References [31, 32] for insightful derivations. We elect to diagonalize the Hamiltonian numerically by truncating the Hilbert space, corresponding to only allowing for a fixed number of excitations. This is reasonable because the RWA doesn't apply for higher occupation numbers. The numerical treatment also provides a quick generalization when the multi-level transmon qubit replaces the two-level atom.

We rely on the generative definitions for the matrix representation of a and a^\dagger :

$$a |n\rangle = \sqrt{n} |n-1\rangle \quad (1.25)$$

$$a^\dagger |n\rangle = \sqrt{n+1} |n+1\rangle, \quad (1.26)$$

In Figure 1.1(a), we plot the lowest two eigenstates of the JC Hamiltonian after truncating the Hilbert space to five excitations. We see that when the atom and cavity are nearly resonant, their frequencies shift by $2g$. Near this avoided crossing, the atom and cavity are not well-distinguished: The energy eigenstates are mixtures of atom and cavity modes. Far from the avoided crossing, the cavity retains a small atomic component.

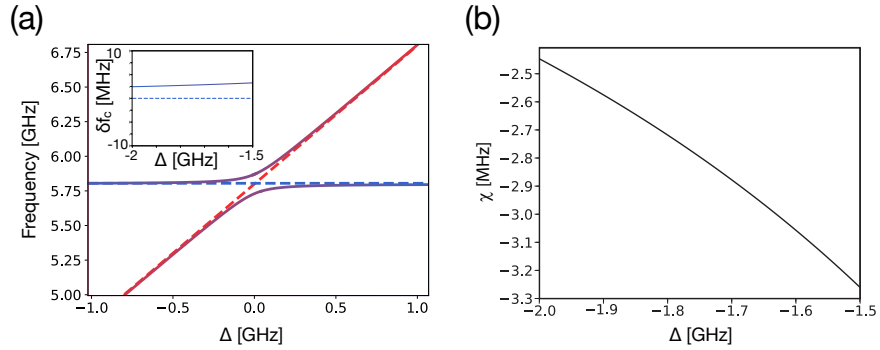


Figure 1.1: (a) The frequencies of the JC Hamiltonian [Eqn. 1.24] as a function of the atom(qubit)-cavity detuning, $\Delta = \omega_q - \omega_c$ with $\omega/2\pi = 5.8$ GHz and $g/2\pi = 70$ MHz. The atom's frequency (red) increases while the cavity frequency (blue) remains fixed. Compared to the uncoupled systems (dashed lines), atom-cavity coupling induces an avoided crossing at $\Delta = 0$ of separation $2g$. Near resonance (purple) the atom-cavity constituents are indistinguishable. The inset shows the cavity behavior in the case of large detuning ($\Delta \gg g$). (b) The dispersive interaction rate, χ , as a function of the atom-cavity detuning.

Dispersive Jaynes Cummings

The Jaynes-Cummings Hamiltonian is further simplified when the atom and cavity are significantly detuned. In the dispersive limit, $|\Delta| \gg g$, a Schrieffer-Wolf transformation [33]

with the unitary operator $U = e^{\frac{g}{\Delta}(a\sigma^\dagger - a^\dagger\sigma)}$ results in the dispersive JC Hamiltonian:

$$H_{\text{JC}}^{(\text{disp})}/\hbar = \omega_c \left(a^\dagger a + \frac{1}{2} \right) + \frac{\omega_q}{2} \sigma_z + \chi a^\dagger a \sigma_z. \quad (1.27)$$

The dispersive rate, $\chi = \frac{g^2}{\Delta}$, describes the small energy shift in the atom's and cavity's energy dispersion, shown in Figure 1.1(b).

The final term describes the atom-cavity interaction in this limit. Because the term is proportional to $a^\dagger a$, it can be incorporated into the cavity frequency: $\omega_c \rightarrow \omega_c + \chi \sigma_z$. The final term is also proportional to σ_z , so it can be incorporated into the atom's frequency: $\omega_q \rightarrow \omega_q + \chi a^\dagger a$. Each frequency shift occurs in tandem, affecting both atom² and cavity frequencies.

The cavity shift is of primary interest because it enables measurement of the atom's state. With the dispersive interaction, the cavity's frequency encodes the atom's state, being shifted by $+\chi$ if the atom's state is $|0\rangle$ and $-\chi$ if the atom's state is $|1\rangle$.

This dispersive measurement technique is desirable for two reasons. First, dispersive measurements are non-destructive. This contrasts with other platforms such as photon- or neutron-based qubits [34, 35, 36], which perform measurements by absorbing the system. Such a measurement obviously prevents any further evolution or measurement. Dispersive measurements are non-destructive because the measurement interaction only shifts the frequencies of the atom and cavity, rather than transferring excitations between systems.

²The factor of $\frac{1}{2}\omega_c$ in the cavity Hamiltonian also shifts the atom's frequency by a small amount called the Lamb shift. But this is neither controllable nor observable, so we ignore it.

However, merely non-destructive measurement can still significantly affect the system's dynamics. The second advantage of dispersive measurements is that they are quantum non-demolition QND. QND measurements do not affect the system's dynamics during measurement. This requires the system's Hamiltonian commutes with the interaction Hamiltonian [37, 38].

For the dispersive JC Hamiltonian, as described in Equation [1.27], verifying QND is easy because the atom's Hamiltonian clearly commutes with the interaction Hamiltonian: $[\sigma_z, a^\dagger a \sigma_z] = 0$. However, the calculation for transmon qubits coupled to microwave cavities is far more involved. Detailed calculations of the dispersive approximation [39, 3] show that cQED measurement is approximately QND when the cavity contains less than the critical number of photons, $\bar{n}_c = \frac{\Delta^2}{4g^2}$.

In this regime, cQED systems can be measured continuously. While the trajectory approach is outside the context of this dissertation, it provides a fascinating perspective on quantum dynamics [3, 4, 5, 6, 9, 10, 40, 11, 12, 41, 7, 8, 13].

1.3.2 Partial Measurements

Projective Measurement

In the simplest textbook approach, quantum measurement completely collapses the wavefunction and returns unambiguous state information. Consider a system in a general superposition state. The wavefunction may be written in the measurement basis as $|\psi\rangle = \sum_i \alpha_i |i\rangle$. The amplitudes, α_i are complex, and the states, $|i\rangle$, are eigenstates of the measurement operator. This bra-ket formulation describes pure states. However, partial measurements can result in incomplete information about the state. Therefore, we move to the density matrix formalism [42, 43], where the state is $\rho = |\psi\rangle \langle\psi|$.

When a measurement occurs, the wavefunction collapses onto one of the eigenstates, chosen randomly with probability equal to the amplitude's square³ magnitude. The collapse is realized mathematically by applying a projector. The projector representation decomposes the measurement operator, A , into a complete set of projectors:

$$A = \sum \lambda_i \Pi_i \equiv \sum_i \lambda_i |i\rangle \langle i|, \quad (1.28)$$

where λ_i is an eigenvalue of the measurement operator with associated projector Π_i . If the random outcome is λ_i , then the state updates by applying the corresponding projector:

$$\rho \rightarrow \rho' = \frac{\Pi_i \rho \Pi_i^\dagger}{\text{Tr}[\Pi_i \rho \Pi_i^\dagger]}. \quad (1.29)$$

The outcome occurs with probability $p_i = \text{Tr}[\rho \Pi_i]$.

Non-Projective Measurement

The projective model of measurement supposes that wavefunction collapse is immediate and irreversible. However, realistic measurements involve an interaction with a measurement apparatus over a finite amount of time. The interaction is unitary, and thus in principle reversible [45].

For partial measurements, we generalize the update operators from projectors to Kraus operators. The Kraus operator formalism describes measurement as an interaction between the system and a measurement apparatus followed by the projection of the apparatus. The Kraus operator itself describes the effect of this process on the qubit state. See References [46, 47, 43] for detailed treatments.

³The square has been called the footnote that won a Nobel Prize. Max Born's 1926 paper [44] did not originally propose the squared magnitude. However, a footnote reads "Addition in proof: More careful consideration shows that the probability is proportional to the square of the [amplitude]."

Upon obtaining an outcome j , the state updates via the Kraus operator K_j :

$$\rho \rightarrow \rho' = \frac{K_j \rho K_j^\dagger}{\text{Tr}[K_j \rho K_j^\dagger]}. \quad (1.30)$$

The probability of obtaining outcome j is

$$P(j) = \text{Tr}[K_j \rho K_j^\dagger]. \quad (1.31)$$

Furthermore, the probability of obtaining an outcome within a range, $[a, b]$, is given by

$$P([a, b]) = \sum_{j=a}^b \text{Tr}[K_j \rho K_j^\dagger]. \quad (1.32)$$

The full set of Kraus operators, $\{K_j\}$, satisfies the relation $\sum_j K_j K_j^\dagger = 1$. This guarantees that $\{K_j\}$ is a valid (completely positive) density matrix transformation (ie that the ρ' satisfies total probability $\text{Tr}[\rho'] = 1$) and that the set of possible outcomes, $\{j\}$, is self-consistent.

Using the relations above, we can construct a new operator $M = \sum_{j=a}^b K_j K_j^\dagger$ which describes the effect of a coarse-grained measurement of all values on the interval⁴ $[a, b]$. If the interval is large enough, M can describe the effect of a projector. Thus, Kraus operators can be thought of as building blocks for other measurement operators. Or conversely, that a single measurement, such as a projector, can be broken down into constituent Kraus operators.

The Kraus operator formalism appears very similar to projective measurements (cf. Eqn. 1.29 with Eqn. 1.30). The similarity arises because any valid measurement can be modeled as an interaction between the system and an auxiliary followed by a projective measurement of the auxiliary [48, 49]. The distinction comes from the number of outcomes. Unlike the set of

⁴Because this holds for any interval, the Kraus operator set forms a measure. Because each K_j is positive, the new M is positive. Hence, the Kraus operator map is a positive measure that is based on operators—a positive operator-valued measure.

projectors, with cardinality equal to the Hilbert space dimension, a set of Kraus operators can have any number of elements. In particular, for the qubit-type systems we study in this dissertation, there are only two projectors for a given measurement operator (e.g. σ_z), corresponding to the two eigenstates. But our weak measurement has many more outcomes, thanks to the cavity's many pointer states. The multitude of outcomes allows for subtle state update (backaction) after a non-projective measurement.

Partial Measurement in cQED

For a detailed treatment of obtaining Kraus operators in cQED platforms, see References [3, 50, 4]. The key result is that because the cavity state is prepared as a coherent state, the probability of a partial measurement outcome is Gaussian-distributed. Therefore, the Kraus operator is given by:

$$K_j = \left(\frac{1}{2\pi\sigma^2} \right)^{1/4} \exp \left(-\frac{[jI - \sigma_z]^2}{2\sigma^2} \right). \quad (1.33)$$

The variance, σ^2 is given by:

$$\sigma^2 = \frac{\tau}{\delta t}, \quad (1.34)$$

where δt is the measurement duration, and the measurement rate $\frac{1}{\tau} = \frac{8\chi^2\bar{n}}{\kappa}$ [51], for a cavity of linewidth κ , populated with \bar{n} photons and dispersively coupled to the qubit at a rate χ .

Chapter 2

Direct-Write Qubits

2.1 Introduction

This section details the development and results of a novel fabrication method for Josephson junctions (JJs) for use in superconducting qubits. The junctions are fabricated with an all-optical direct-write laser lithography system. Because the features written into a resist mask are significantly larger when using photolithography rather than e-beam lithography, photolithography-written JJs often have large overlap areas. Large lithographic areas lead to high numbers of two-level system (TLS) defects, as has been seen in a variety of experiments [52, 53].

JJs primarily function as a nonlinear inductance for LC circuits (see Sect. 1.2.3). However, they also host part of the electric field which can dipole-couple to TLS defects. To improve device quality, defect numbers and densities should decrease. Prior work has shown that decreasing JJ areas is an effective strategy for mitigating TLS loss. However, as this chapter

investigates, careful deposition and design can still lead to low TLS and low loss even with large areas.

TLSs have been a significant source of loss in state-of-the-art quantum devices, including both superconducting [54, 55, 56, 57] and trapped ion [58] platforms. Thus, devices have historically been made as small as possible while maintaining robust fabrication yield. Though most of this shrinking has focused on the area of the junction, some work has also used extremely thin superconducting films (a few nm). Thinner films diminish the expected number of TLS at the cost of diminished superconductivity [59].

For our process, we seek to incorporate two lines of investigation which have proved beneficial in the superconducting circuit community: geometric variation and careful surface treatments. For both coplanar-waveguide resonators and qubits, a device's geometry can be adjusted to minimize electric field storage in lossy materials. While the primary materials (silicon, sapphire, aluminum, and niobium) have low loss [60], other materials which find their way into devices do not have low loss. These primarily reside at metal-substrate, metal-air, and substrate-air interfaces, and they are often introduced during fabrication steps.

In resonators, modifying the form (either $\lambda/2$, $\lambda/4$, or lumped element) modifies how much of an electric field is stored at these interfaces [61, 62], as quantified by the filling factor [63, 57]. Detailed studies of resonator geometry have modified the filling factor by, for example, over-etching the substrate to minimize the substrate-air interface [64, 65, 66, 67, 68]. Other work has focused on the metal-substrate interface. Larger center trace widths diminished TLS loss [69, 70, 71, 72]. If TLS at interfaces can be suppressed, then large feature sizes can dilute electric field densities, decreasing TLS coupling and improving coherence.

In qubits, altering the geometry has also led to improved understanding of the origin of TLS loss. Besides micromachining substrates as in resonators [73], simple geometric modification

can highlight sources of loss. In particular, a variety of alternative designs for transmon shunting capacitor pads led to an understanding of the loss tangents of these materials [74, 75]. As is commonly used in the field, 3D transmons [76] attain high coherence by moving electric fields away from the substrate. Similar to the diluted electric fields in resonators, large-area JJs have recently shown high coherence times in mergemon qubits [77, 78].

The second line of investigation we follow is that of surface treatments. Early experiments with resonators [79] and recent direct measurements imply that around 60% of TLS reside in interfacial surfaces [80, 81]. This understanding has motivated surface-treatment experiments focusing on removing or avoiding oxides and other contaminants through the use of buffered-oxide etching (BOE) [82, 83], other chemical cleanings [68], and inter-metal bandages [84, 85, 86]. This focus on clean surfaces has improved resonator quality factors to well above 10^6 [87, 66, 67, 68, 83].

2.2 Fabrication Theory

2.2.1 Josephson Junction Nonlinearity

Chapter 1 described how the nonlinear inductance provided by JJs creates a platform for studying quantum information of pseudo-spin $1/2$ systems. In this section, we describe the underlying physics that provides the nonlinear inductance.

Two superconductors separated by an electrically insulating tunnel barrier form a JJ. The insulator impedes electron transport, allowing conduction only via tunneling. The superconducting wavefunction can coherently traverse the insulating barrier only when pairs of electrons tunnel (Cooper pair tunneling) [88, 89].

The key feature of a JJ is its nonlinear inductance. The inductive nature of the SIS junction comes from the Josephson relations, which will be derived below, in Section 2.2.2.

The Josephson equations define the current-voltage relationship in terms of the superconductor phases at each end of the junction. The difference between the phases, δ , generates a tunneling current and a potential difference according to the Josephson equations:

$$V = \Phi_0 \dot{\delta} \tag{2.1}$$

$$I = I_0 \sin \delta \tag{2.2}$$

Fabrication fixes the critical current, I_0 (see Section 2.2.3), and Φ_0 is the reduced flux quantum, $\Phi_0 = \hbar/2e \approx 2.0 \cdot 10^{-15}$ Wb ≈ 3.0 GHz h/nA , which depends on (reduced) Planck's constant h (\hbar) and the fundamental charge e . Manipulating the above equations leads to the inductance of the junction:

$$\begin{aligned} L &= \frac{V}{\dot{I}} \\ &= \frac{\Phi_0 \dot{\delta}}{I_0 \cos \delta \dot{\delta}} \\ &= \frac{\Phi_0}{I_0 \cos \delta} \end{aligned} \tag{2.3}$$

Because the Josephson equations result from coherent tunneling, JJs provide dissipationless nonlinear inductance.

2.2.2 Josephson Relations from BCS Theory

To derive the effect of tunneling Cooper pairs—the Josephson effect—we begin with the BCS model stated as a superconductor Hamiltonian [90, 89]:

$$H_{\text{BCS}} = J \sum_k a_k^\dagger a_k + V a_k^\dagger a_{-k}^\dagger a_k a_{-k}. \quad (2.4)$$

The Hamiltonian describes single-electron excitations of momentum k with creation (annihilation) operators a_k^\dagger (a_k). The second term describes a potential that enforces net-zero-momentum interactions.

A Bogoliubov transform translates the second-quantized Hamiltonian into more familiar two-level-system operators. The transform better represents the symmetry enforced by the zero momentum condition. The new creation and annihilation operators, c_k and c_k^\dagger are

$$c_k = u a_k + v a_{-k}^\dagger \quad (2.5)$$

$$c_{-k} = -v a_k + u a_{-k}^\dagger, \quad (2.6)$$

where $u = \cos \theta$ and $v = \sin \theta$ such that $2\theta = \arctan\left(\frac{J}{V}\right)$.

In the new representation, we can truncate the Hilbert space to get two-dimensional operators:

$$H = \sum_k \xi_k \sigma_z^k - \frac{V}{2} \sum_{k,l} \sigma_x^k \sigma_x^l + \sigma_y^k \sigma_y^l, \quad (2.7)$$

where we consider two momentum k and l , ξ_k is the kinetic energy relative to the Fermi energy, and V is the potential difference across the junction leads.

The form of the Hamiltonian $H \sim \sigma_z + \sigma_x$ is a familiar qubit Hamiltonian under Rabi drive [31, 32]. The energy eigenstates for this Hamiltonian can be written in the form

$$\psi = \bigotimes_k [u_k \begin{pmatrix} 1 \\ 0 \end{pmatrix} + e^{i\phi_k} v_k \begin{pmatrix} 0 \\ 1 \end{pmatrix}]. \quad (2.8)$$

The two states correspond to a filled (v_k) or unfilled (u_k) momentum-pair state.

The mean-field solution [89] shows that the phase ϕ_k depends exclusively on the potential term in the Hamiltonian. Thus, with direct control of the external voltage across the junction, one can directly modify the phase. The modification transforms the phase: $\phi_k \rightarrow \phi_k + 2e/h \int V dt$. The derivative of this voltage-altered phase is:

$$\frac{\partial \phi_k}{\partial t} = \frac{2e}{\hbar} V, \quad (2.9)$$

which is the AC Josephson effect, Equation [2.2].

2.2.3 Cabrera-Mott Oxidation Model

A key development in this chapter is a novel oxidation schedule to achieve low critical currents in large-area JJs. Here we present a summary of the Cabrera-Mott model for metal-oxide growth dynamics on thin films [91, 92]. The resulting dependence of oxide thickness on time is logarithmic and self-limited. The model is commonly used to describe the growth of aluminum oxide [93, 94, 95, 82, 96].

Metals oxidize when exposed to molecular oxygen that has adsorbed onto the metal's surface. The growth process can be summarized in three steps. First, electrons tunnel through the barrier and ionize adsorbed oxygen. Second, a Mott potential results from the displaced

charges. Finally, metal ions hop across lattice sites, expanding the size of the oxide. We describe each step below.

Cabrera-Mott theory depends on the free transfer of electrons from the metal to the adsorbed oxygen. In Section 2.2.3, we will describe the physical mechanism for tunneling and show that the tunneling probability decreases (exponentially) with the thickness of the film. This is the origin of the self-limiting nature of Cabrera-Mott growth and limits the discussion to thin films.

Electrons donated by the metal ionize the adsorbed oxygen atoms or molecules on the oxide-gas surface. A positive charge at the metal-oxide interface results from the metal's electron donation. The charge difference creates the Mott potential, $\Delta\Phi$, which drives metal ions across the oxide, increasing the oxide thickness. We can calculate the magnitude of the Mott potential by treating the charge separation as a capacitor:

$$\Delta\Phi = Q/C = (2en_0) \cdot X/\epsilon_r, \tag{2.10}$$

where X is the oxide thickness, n_0 is the number of excess oxygen ions per unit area, ϵ_r is the relative permittivity of the oxide layer, and e is the elementary charge. n_0 is calculated via the equilibrium chemical reaction $\frac{1}{2}O_2 + 2e \rightarrow O^{2-}$. It determines the oxygen ion concentration as a function of the free energy difference of the reaction and the concentrations of each reactant.

Cabrera-Mott theory then estimates the oxidation rate with the rate of the slowest process: vacancy formation due to metal atoms hopping across sites. Vacancies result from either metal atoms entering the oxide (combining with oxygen in the oxide) or from metal atoms leaving the oxide (combining with adsorbed oxygen on the oxide surface). The energy cost of moving across interfaces is the activation energy W , but this cost is lowered due to the

Mott potential. The hopping probability is thus given by $\exp[-(W - ea\Delta\Phi/X)/kT]$. The growth rate depends on the interatomic spacing a and the time scale of hopping, set by the vibrational frequency of the lattice, ν . Thus, the Cabrera-Mott theory of oxidation predicts a growth rate:

$$\dot{X} = \frac{D}{a} e^{-\frac{X_{\max}}{X}}, \quad (2.11)$$

where $X_{\max} = ea\Delta\Phi/kT$ sets the maximum film thickness for which Cabrera-Mott theory applies and $D = a^2\nu e^{-W/kT}$ sets a material-specific diffusion constant.

The qualitative behavior of this type of film growth is exponential suppression of the growth rate as the film thickness increases. Equation [2.11] can be solved in the limit $X \ll X_{\max}$ to recover inverse-logarithmic growth of oxide thickness with time:

$$X(t) \sim \frac{1}{1 - \ln t} \quad (2.12)$$

This prediction has been recently measured directly with *in situ* optical-transmission measurements during aluminum oxidation [96]. Using constants fit to this data, the inverse-logarithmic behavior of Equation [2.12] is shown in Figure 2.1. In an initial fast-growth regime, the oxide thickness grows quickly. But the thickness quickly saturates to a maximal value within a few minutes, proceeding in a slow-growth regime.

For the sake of tuning JJ critical currents, this strong logarithmic dependence is not insurmountable. The exponential sensitivity of critical current on oxide thickness [Eqn. (2.15)] cancels the logarithmic sensitivity of thickness on time, allowing reasonable scaling of critical current with oxidation time, up to a relatively thin limiting thickness.

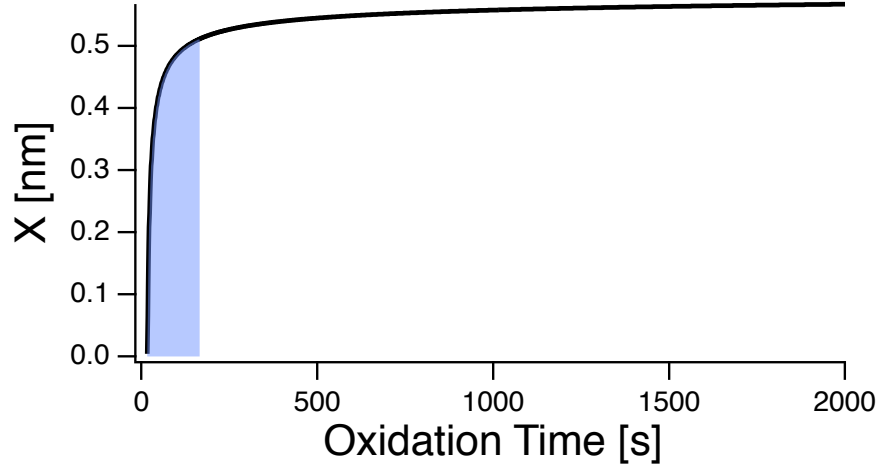


Figure 2.1: Oxide thickness, X , as a function of time under similar conditions to our oxidation environment. Two regimes are visible. A fast regime (blue) accounts for the first 90% of the film growth, and the slow regime represents nearly saturated growth. Non-zero y-offset is due to numerical error.

Barrier Tunneling Resistance Theory

We have discussed how the BCS Hamiltonian leads to eigenstates and dynamics of the current-voltage relationship for JJs. This section focuses on how junction geometry, especially the oxide barrier thickness, affects the critical current. The theory was originally developed by Stratton [97] and expanded by Simmons [98].

Consider a JJ as a 1D tunneling barrier. With an applied potential difference, V , across the junction, electrons on one lead have a higher Fermi level than pairs on the other. However, the tunneling barrier of height Φ inhibits conduction. Provided the barrier is thin enough, electrons can tunnel through. Using the WKB approximation [42], the tunneling probability for an electron with energy E is

$$p(E) = e^{-\frac{4\pi}{h}\sqrt{\Phi+\epsilon_F-E}}, \quad (2.13)$$

where ϵ_F is the Fermi energy of the metal.

To calculate the tunneling current, we need the number of electrons with energy E . Modeling the electrons as a free Fermi gas model allows us to calculate the number of tunneling electrons. The tunneling current density is given by

$$\begin{aligned} J &= e(N_1 - N_2) \\ &= e \frac{4\pi m^3}{h^3} \int [f(E) - f(E - eV)] p(E) dE. \end{aligned} \tag{2.14}$$

The integral can be solved for the specific case of a tunneling barrier and expressed as a resistance [98]:

$$R(X) = \frac{8 \cdot 2\pi R_0 \cdot X^2}{(1 + 2KX) \exp(2KX)}, \tag{2.15}$$

where $K = \frac{1}{\hbar} \sqrt{2m\Phi}$ depends on the electron mass m , elementary charge e and the tunneling barrier height, Φ . $R_0 = h/2e^2$ is the inverse of the conductance quantum. For aluminum oxide, the estimates of the barrier range from $\Phi \sim 0.15 - 2$ eV [82, 99, 100].

The resistance derived above translates to a critical current via the Ambegaokar-Baratoff relation [101]. The relation comes from a detailed treatment of the superconducting wavefunction. However, the result has the familiar form of Ohm's law:

$$I_c = \frac{\frac{\pi}{2} \frac{\Delta}{e}}{R_N}. \tag{2.16}$$

The superconducting gap in volts is Δ/e , and the normal resistance, R_N , can be probed at room temperature. The full quantum mechanical treatment produces the factor of $\pi/2$ [101].

The joint requirements of frequency and transmon-regime set the scale for the required charging and Josephson energies, as discussed in Section 1.2.3. These specifications require $I_c \approx 10$ nA

2.3 Recipe Development

2.3.1 Design-of-Experiment Philosophy

When developing recipes and best practices, a common approach is to use “A/B testing”. A treatment (such as a cleaning step) can be applied (A) or not applied (B), and the final figure of merit (such as quality factor) can be directly evaluated based on the average outcome, while also considering standard deviations. This strategy can provide clear evidence for the efficacy of a single variable. However, when an outcome depends on multiple variables, the results can be misleading. For example, the A/B test results may differ when other variables changes. We will show an example in Section 2.3.2, where this was the case.

An alternative methodology is called “Design of Experiment”. The most complete Design of Experiment test is a factorial test. A factorial test sweeps each variable independently through its full range. Ideally, each sweep is repeated multiple times to quantify variability.

This test can be time- and labor-expensive, because for even just two treatments, the number of experiments grows like 2^n for n number of variables. However, this methodology offers a complete statistical picture through analysis of variance (ANOVA). In particular, interactions between variables can be directly monitored in factorial design statistics. More advanced methods, such as nested factorial designs, offer more efficient approaches [102]. We will make use of a Design of Experiment test in Section 2.3.2.

2.3.2 Resist Exposure Tuning

Imaging Resist Only

In this section, we describe the lithography development process for our all-optical direct-write photolithography system. First, we focus only on one of the two resists in our dual-resist stack. Then, we describe the full resist stack.

We expose resist with a Heidelberg DWL 66+ system. To adjust the dose, the user may set the laser power, laser intensity, and filter. Laser power and intensity combine to set the net dose. (Laser power is largely fixed for each write head.) Filter percentage selects a neutral density filter to further attenuate the laser power, and thus further modifies the dose. The user may also adjust the focus of the optical write head. The focus is a percentage value and sets the lens's relative Z-offset from its default position. This allows the laser to target different parts of the resist stack. Each of these four parameters must be tuned to some precision to achieve target feature sizes.

In addition to exposure calibration, the resist stack must be calibrated as well. For example, we can also tune the resist behavior with softbake time and temperature along with development time, temperature, and mechanical agitation (such as by hand or with an ultrasonic bath).

Thus, the full calibration procedure can be quite involved. Degeneracy in the above nine variables confounds interpretation. For example, one can tune the exposure dose by using both the intensity and the filter percentage. While we have experimented with each of the nine parameters listed above, this section will only focus on changes in a few and leave the rest fixed to optimized values.

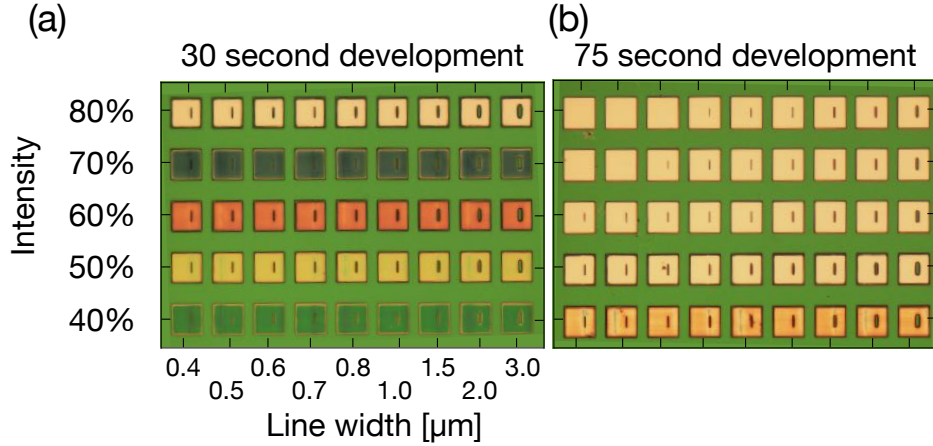


Figure 2.2: An optical micrograph of S1805 resist after an exposure dose test. The images display a three-dimensional slice of a five-dimensional sweep between the exposure intensity, the development time, minimal line width, filter percentage (fixed), and focus percentage (fixed). Colors (unaltered) indicate residual resist of varying thickness. Dark green corresponds to the full stack without exposure, and tan corresponds to the silicon substrate, where the resist is fully developed.

First, consider a resist stack composed only of imaging resist—MicroChem Shipley S1805. The data presented here is from an early test that highlights the role of intensity and focus. The pattern creates an array of tall resist stripes of varying widths between 0.3 and 3 μm . This pattern is the inverse of what is necessary for a JJ, but it provides a basic test for the resist-exposure combination. The pattern is written many times with a matrix sweep of laser intensity and focus percentage. The matrix repeats across the wafer, and matrix copies develop for various times.

Figure 2.2 displays test results for three variables: intensity, development time, and minimum line width. Degeneracy appears even in this relatively simple sweep. A high-intensity exposure developed for a short time (Fig. 2.2a, 80% intensity) produces similar results to a low-intensity exposure developed for longer (Fig. 2.2b, 50% intensity). This particular test showed no significant difference between adjusting the focus percentage from -50% to -30%, despite being

quite different from the optimal (-17% focus at the time). Design principles such as working far from extreme values can help break the degeneracy and determine working parameters.

This test does not probe consistency, despite the importance to process reliability. Though many of the parameter vectors work here, this test does not identify if they will work consistently across a wafer or consistently throughout time. Such one-off tests should be repeated many times to provide yield information.

Full Resist Stack

The resist tests performed in the above section optimized the exposure and development procedures for a single layer of resist. They set useful baselines for moving to the full double-resist stack.

Our full resist stack includes two resist layers. The top imaging layer is S1805, and the bottom liftoff resist is MicroChem LOR 10B. Liftoff resists are more sensitive to exposure and thus overdevelop beyond the exposure region. This creates an undercut that can be used as a mask for angle-selective deposition of metals. We designed the resist stack to support Dolan bridge shadow mask evaporation [103]. Other mask techniques include the overlap and the Manhattan methods [104, 105, 106], but the Dolan bridge technique allows us to utilize a multi-step oxidation scheme, as detailed in Section 2.3.4.

Our spin and softbake recipes target 1 μm height in the liftoff resist and 0.6 μm in the imaging resist (see Section 2.3.4). Our recipes are tailored for 1.5 μm undercuts, but the liftoff photoresist supports undercuts up to 10 μm .

In Figure 2.3, we show optical and scanning electron microscope (SEM) images of the resist stack after development. The feature sizes are large due to the wavelength limitation of

photolithography. The SEM image in Figure 2.3(b) provides a perspective on the resist shadow-masking deposited gold.

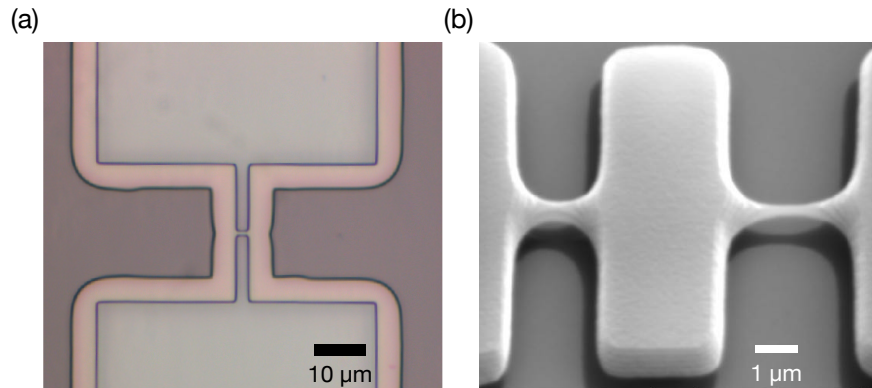


Figure 2.3: The developed resist stack after exposure and development. (a) An optical image of the resist after exposing a single JJ. The color indicates the number of resist layers. White corresponds to bare substrate, indicating both resist layers have cleared. Dark pink indicates both resist layers persist in unexposed regions. Light pink indicates undercut regions where the bottom resist (LOR10B) has dissociated, but the top imaging resist (S1805) persists. Of central importance is the undercut region in the middle which creates the Dolan bridge. (b) A tilt-view SEM image of the resist stack (after depositing gold to prevent charge buildup and improve contrast). Shadows indicate a lack of gold due to resist masking.

Factorial Design of Process Variables

With all the variables at work in the fabrication pipeline, understanding how each component behaves in isolation can tell a very different story when all variations can occur together. Such interacting processes require Design of Experiment principles, as introduced in Section 2.3.1, we create a test that varies five critical variables in a factorial design: number of JJs, exposure intensity, radial position, evaporation angle, and number oxidation layers.

The design includes a pattern that is repeated across the wafer and subjected to different treatments. A single pattern contains chains of up to 8 SQuIDs connected in series. This

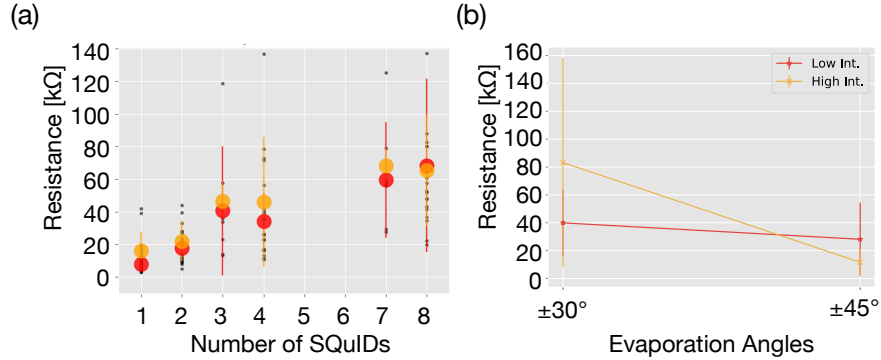


Figure 2.4: A selection of results for a factorial design of JJ fabrication parameters. (a) The resistance scales with the number of JJ (SQuIDs) in series, as expected. For each number of SQuIDs, the oxidation and evaporation treatments are fixed. Black points indicate different positions. The average and standard deviation over the set of positions yields the colored circles and error bars. Colors indicate the development treatment: red corresponds to low-intensity exposure with long development time and orange corresponds to high-intensity exposure with short development time. Junction-number scaling is independent of development treatment. (b) The resistance for sets of single-SQuID devices averaged over the position and number of oxide layers. The line is a guide to the eye showing the decrease with the area. The decrease is significantly stronger in the high-intensity development. Also, the high intensity development shows significantly larger variation.

pattern repeats across the wafer. Quarters of the wafer receive different exposure treatments: either high-power exposure (54 mW effective power) with short development time (35 seconds) or low-power exposure (33 mW effective power) with long development time (60 seconds), similar to the treatment in Section 2.3.2 (especially Fig. 2.2). Horizontal dices across each quarter separate stripes of repeated patterns for different evaporation and oxidation treatments. The radial position varies along each stripe. The evaporation treatment entails evaporation at 30° or 45° relative to the wafer’s normal vector. The oxidation treatment is either one or two layers of oxidation, detailed in Section 2.3.4. This test runs the gamut of tunable parameters within our standard process, although we have severely limited the range in order to retain tractability.

The figure of merit for these devices is the room temperature resistance. Multiple repetitions of single-JJ chains provide statistics on resistance deviation. In the following results, we take

a variety of slices through the parameter space and examine the impact on resistance and resistance deviation.

First, consider how the resistance increases with the number of JJs in Figure 2.4(a). We focus discussion on the case of a single oxidation step with one evaporation angle while averaging over the radial position. The resistance trends nearly linearly with the number of SQuIDs. Deviation from the linear trend is largely due to the finite resistivity of the silicon substrate (15 k Ω cm). The trend is independent of the exposure treatment.

This independence does not hold for the evaporation angle treatment, shown in Figure 2.4(b). For either exposure, increasing the evaporation angle increases the area of the junction, lowering the resistance. However, there is significant interaction between the evaporation angle and the treatment. With low-intensity exposure and long development [red points in Fig. 2.4(b)], the decrease in resistance with angle is significantly less than in the case of high-intensity exposure. Longer development time allows the exposed resist to fully and uniformly dissolve. In contrast, short development time requires aggressive removal of resist and can lead to significant deviation within a single treatment.

Throughout this design, we observed significant intra-treatment variation. Thus, several of the variables motivate specific studies as a single variable. For example, we found that a significant amount of variation resulted from position treatments. We corroborated the resistance measurements with SEM imaging [see Fig. 2.8(a) for an example] for one wafer chip with fixed oxidation, evaporation angle, and development. Figure 2.5 shows that this single treatment contained wide variation in the junction area, leading to predictable variation in the normal resistance. The variation in the area is discussed in detail in Section 2.3.3. In addition, Section 2.4.1 describes resistance scaling with the number of oxide layers.

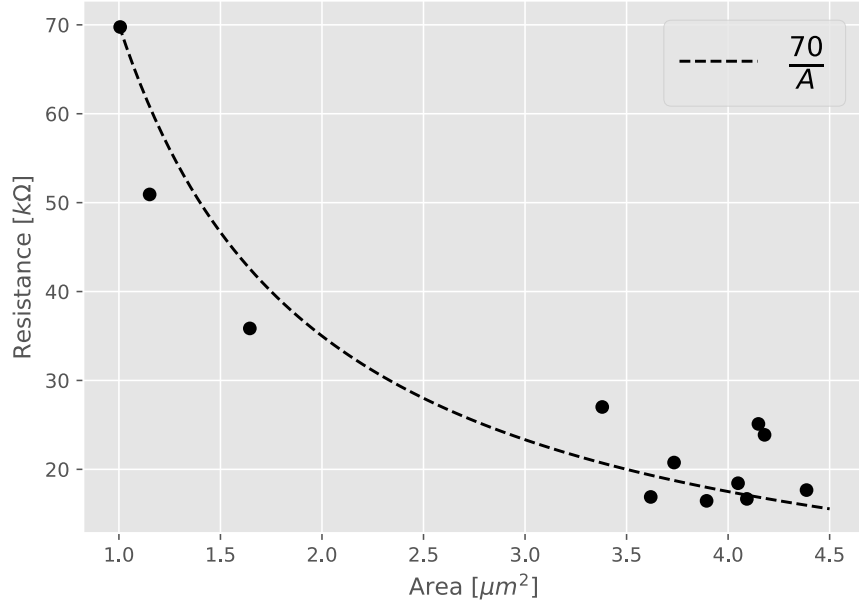


Figure 2.5: Normal resistance measurements for a batch of junctions made under nominally identical conditions. The area, A , is based on SEM imaging [such as in Fig. 2.8(a)]. The dashed line is a guide to the eye indicating the $1/A$ dependence of resistance.

2.3.3 Junction Consistency Tests

During recipe development, we identified significant variation among devices fabricated under identical processes. The following tests illustrate a path towards treating the source of that variation.

Manhattan Uniformity Tests

To quantify our process uniformity, we repeat a series of JJs across a wafer. The test includes variation on two distance scales. First, 16 junctions are located in a $50 \mu\text{m}$ strip. Second, groups of junctions are separated throughout the wafer, each placed 6 mm apart. The two scales provide different information about the process variability. Group-scale variation captures intrinsic variation, while wafer-scale variation captures extrinsic variation. These

two types of variation suggest different treatment paths, as we describe in Sections 2.3.3 and 2.3.3.

In this test we utilized Manhattan-style junctions [104, 105, 106] rather than Dolan-bridge-style junctions. The Manhattan approach replaces the Dolan bridge with two orthogonal trenches in the resist. Deposition at more extreme angles (increased from 45° to 70°) places metal on the electrode of the parallel trench but onto the sidewall of the orthogonal trench. Manhattan-style junctions allow for better consistency because the junction area is not sensitive to the resist height [105]. However, the Manhattan process prohibits our two-junction oxidation method for large area JJs (see Section 2.3.4).

The resistance results are shown in Figure 2.6. This test exhibits clear spatial dependence. Moving across the wafer either horizontally [Fig. 2.6(a)] or vertically [Fig. 2.6(a)], increases the mean resistance by nearly a factor of two. While the within-group variation is only 8%, the between-groups variation is 20%, after removing outliers such as open circuits.

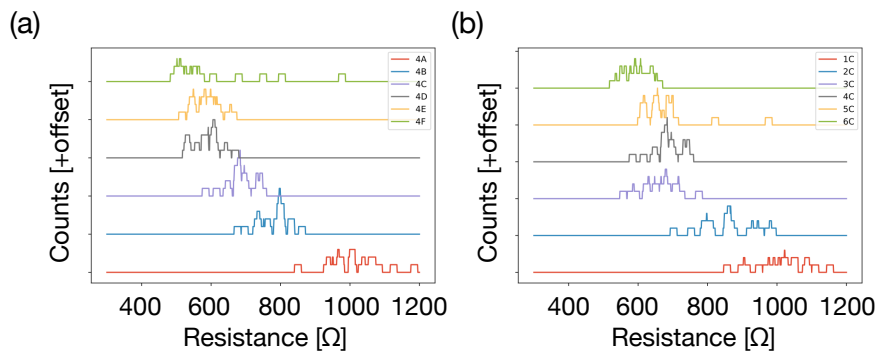


Figure 2.6: Histograms of resistance of identically fabricated JJs using the Manhattan process. Each trace corresponds to a group of JJs within a $50\ \mu\text{m}$ strip. The traces are offset according to position either (a) vertically or (b) horizontally across a wafer. The variation across the wafer is larger than the variation within a single group.

Wafer Heating for Uniformity

Early in the recipe development, resist spinning showed clear deficiencies. Color changes of the resist on the wafer, due to interference of optical wavelengths, indicated variation in the resist thickness on the order of hundreds of nanometers. Despite clean spins in the previous test, we continued to see large-scale variation. Our testing led to suspicion of hotplate temperature uniformity. An IR thermometer indicated regions $\pm 10^\circ$ C outside of the nominal temperature. Although IR thermometer measurements are inaccurate due to the low emissivity of the ceramic platform, we take the measured range as an estimate of the variation's order of magnitude. According to LOR10B's manufacturer specifications, this magnitude of temperature variation changes the dissolution rate by 45%. Thus, the local temperature variation can create significant differences in the resist patterns.

To test this variable's role, we added a copper sheet onto the hotplate while softbaking the resist. While the high thermal conductivity changes the heat capacity of the heating element, it improves the temperature uniformity.

The test results are shown in Figure 2.7. We used the same pattern and process as in Section 2.3.3. However, compared to the previous Manhattan-process test, the copper-plate softbake does not show a statistically significant shift across the wafer. The average within-group relative standard deviation (the standard deviation divided by the mean) was 7.5%, similar to the bare-plate bake. However, the between-groups variation decreased from 20% to 14%. Spatial variation is significantly mitigated using this softbaking approach.

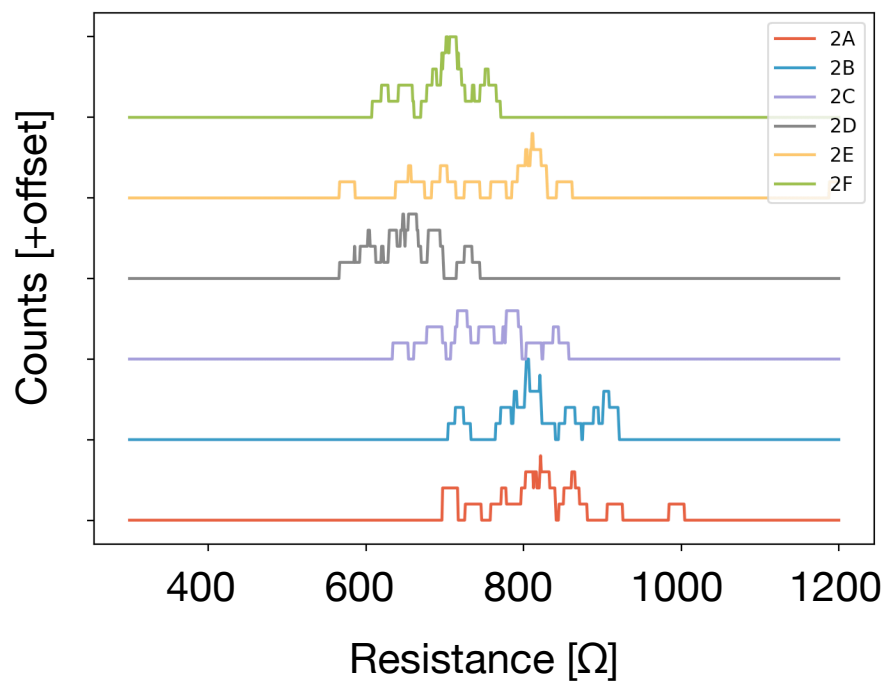


Figure 2.7: Similar to Figure 2.6, each trace is a histogram of resistance within local groups of JJs. Here, the wafer was baked on a copper sheet rather than directly on the hotplate’s ceramic surface. The variability between groups is significantly improved.

Further Directions for Uniformity

Monumental work towards the development of device consistency has identified several additional avenues [107]. Ultrasonic development, rather than by-hand mechanical agitation, can sufficiently displace dissolved resist while removing human error. Other groups using a similar oxygen plasma asher device have found non-radially-symmetric behavior during ashing [107]. Dynamic oxidation, in which oxygen is pumped in and out of the chamber also shows improved uniformity. Cold development—as is common in e-beam lithography [31]—lowers the resist dissolution rate, allowing uniform pattern sizes. Finally, our evaporation rate, 0.3 nm/s, is slow enough to allow large grain formation, improving uniformity and eliminating a site for lossy dielectrics [108].

2.3.4 Full Recipe

The recipe development described above culminates in the following detailed list of the full qubit fabrication process.

1. Silicon substrate

For all devices, we use single-side-polished 2-inch silicon substrates with 100 crystal orientation and high resistivity ($> 15\text{k}\Omega \cdot \text{cm}$).

2. Substrate Cleaning

Clean the blank silicon substrate in a buffered oxide etch (BOE) consisting of ammonium fluoride, ammonium bifluoride, and hydrofluoric acid for 5 minutes at room temperature. A two-step DI water rinse removes and neutralizes residual HF.

3. Spin resist

Attach the wafer to the vacuum chuck of the Brewer Science CEE 200X spin coater. Dispense 3 mL of LOR10B, carefully maintaining a continuous stream to prevent bubbles. Resist dispensation can be a major source of device inhomogeneity. Spin at 3000 RPM for 50 seconds to achieve a target thickness of $1.0 \mu\text{m}$. Soft bake the wafer at 195°C for 10 minutes. Lower temperatures can produce larger undercuts. Dispense 1 mL of Shipley S1805. Spin at 2000 RPM for 30 seconds to achieve a target thickness of $0.6 \mu\text{m}$. Soft bake the wafer at 115°C for 1 minute.

4. Expose transmon pattern

Load the wafer into the Heidelberg DWL 66+. Center the device, and focus the head with pneumatic mode⁵. Exposure parameters should be calibrated monthly for the particular write lens head. For the 10 mm head⁶, recent calibration required 67 mW

⁵Pneumatic mode provides a height accuracy of $\pm 100 \mu\text{m}$.

⁶10 mm refers to the focal length. This lens provides a $1.10 \mu\text{m}$ depth of field.

power, 90% intensity, 25% filter and 0% focus. The dose time is set with the beam's raster rate, 30 kHz.

5. Development

Mechanically agitate the wafer in Microposit Metal-ion Free (MF)-319 developer for 45 seconds at room temperature. Mechanically agitate the wafer in DI water for 30 seconds at room temperature. Blow dry with N₂. The sample may be visually inspected under an optical microscope to check nominal junction dimensions. Dolan bridges should be 1.5 μm long and 1 μm wide. Resist color (indicating thickness) should reflect cleared LOR-10B and intact S1805, as in Figure 2.3(a).

6. Ashing

Use the Plasma Etch PE-50 to ash organics (residual resist) in 100 W oxygen plasma for 20 seconds.

7. Substrate Clean

Clean the wafer again in BOE for 30 seconds at room temperature. HF does not etch our photoresists [109].

8. Pump Down

Quickly mount the wafer and begin pumping down after the BOE clean. Apply two Ti getter steps, with about 5 minutes delay. The base pressure should be $< 10^{-9}$ Torr. Allow at least 18 hours in this ultra-high vacuum (UHV) environment. We believe this removes any residual surface contaminants. Our e-beam evaporator is an AJA ATC-Orion-8E with an 8.5 kV electron source.

9. Evaporation of Bottom Electrode

Align the wafer's in-plane angle to align the wafer's flat vertically, orthogonal to the normal-angle rotation axis. Position the normal angle to +45°. With the shutter

blocking the sample, turn on the automated ramp to increase the e-beam source filament from 0 mA to 180 mA over two minutes. When the targeted current is reached, open the shutter to begin deposition. A crystal oscillator monitor tracks the deposited film thickness, and a PID controller tunes the filament current to match the targeted rate, 3 \AA/s . When the target thickness for the bottom electrode, 30 nm, is reached, the shutter blocks the sample, and the current ramps down in a few seconds.

10. Oxidation

Remove the sample from the UHV chamber into the load lock. Flood the load lock with 99.99% pure O_2 at 4.3 Torr. Use a dose time calibrated to the targeted critical current. Large-area JJs in our transmons require 1800 seconds (30 minutes). Josephson parametric amplifiers ($I_c \sim 1 \mu\text{A}$) require ~ 600 seconds. Our transmon junctions also utilize a multi-step oxidation process. See Section 2.3.4.

11. Evaporation of Top Electrode

Repeat Step 9, but with the normal angle set to -45° . The target thickness is 60 nm.

12. Protective Oxide

After removing the sample to the load lock, another 4.3 Torr oxidation for 60 seconds creates a clean protective oxide. We believe oxidation in a vacuum environment improves aging compared to atmospheric oxidation.

13. Liftoff

Place samples in N-Methyl-2-pyrrolidone (NMP), heated to 60°C for at least one hour. Use a pipette filled with NMP to squirt sacrificial aluminum away. Other groups sonicate during liftoff. Spray-clean the sample with isopropyl alcohol. Blow dry with N_2 .

14. Dice

Use a diamond scribe to score the wafer parallel with the crystallographic axis. Cleave the wafer at the score.

15. Mount Device

For transmons, adhere the silicon to the cavity shelf with GE varnish. For other planar devices, adhere the sample to the enclosure and wire bond the connections.

Multi-step Oxidation for Large-area JJs

To attain the required critical current for transmon qubits (~ 10 nA), a new oxidation scheme is required. Cabrera-Mott Theory (Section 2.2.3) predicts a saturation thickness which results in ~ 1.5 nm thick oxides for our temperature and pressure conditions [95, 82]. With a $1.5 \mu\text{m}^2$ area, this creates a JJ with $\sim 1 \mu\text{A}$ of critical current [98]. While suitable for parametric amplifiers [110, 111, 112], the inductance of such large junctions is unsuited for transmon qubits. Instead, the alternative oxidation scheme laid out below creates two junctions. One of which has the requisite 10 nA critical current.

Our JJs consist of a 30-nm-thick aluminum bottom electrode, an aluminum oxide insulating barrier, and a 60-nm-thick aluminum top electrode. After depositing the bottom electrode, we create the oxide tunnel layer by exposing the electrode to oxygen at 4.3 Torr for 300 seconds. Standard evaporation procedures would proceed with the top electrode [31, 32]. Instead, we add a 0.5 nm filler layer of aluminum. We then oxidized the filler under the same conditions. 300 seconds ensures the full layer is oxidized [95, 82, 96]. We add as many fully oxidized filler layers to achieve the desired critical current, typically three.

Two junctions form through this process. When the bottom electrode oxidizes, both its top face and side face develop oxide layers with the same thickness. The filler aluminum layer

only covers the top electrode due the sharp resist [see Figure 2.3(b)]. Thus, the top-face oxide layer grows by an additional 0.5 nm, owing to the fast initial growth phase of Equation [2.12]. However, the side-face oxide grows only a small amount, owing to the slow growth phase (see Figure 2.1).

The top electrode encapsulates both top- and side-face junctions. The top-face junction's thickness implies that its resistance and inductance are exponentially larger than the side-face junction, according to Equation [2.15].

2.4 Devices

In this section, we describe results for large-area transmons [113]. The results provide insights into the loss mechanisms for state-of-the-art quantum computing devices. In particular, we show JJ areas need not be small to have good coherence. Instead, surface cleaning is essential.

The results are broken down into four categories. First, in Section 2.4.1, we describe the physical structure of the junctions, including a cross-sectional view of junctions and tests of the oxidation method. Then, Section 2.4.2 presents spectroscopy results, which verify the transmon nature of the circuit. In the process, we observed several of strongly-coupled TLS defects resulting from uncleaned surfaces. Next, Section 2.4.3 presents coherence times, including for uncleaned devices. Finally, Section 2.4.4 provides a few checks against additional loss mechanisms and summarizes the results.

2.4.1 Structure of Large-Area Junctions

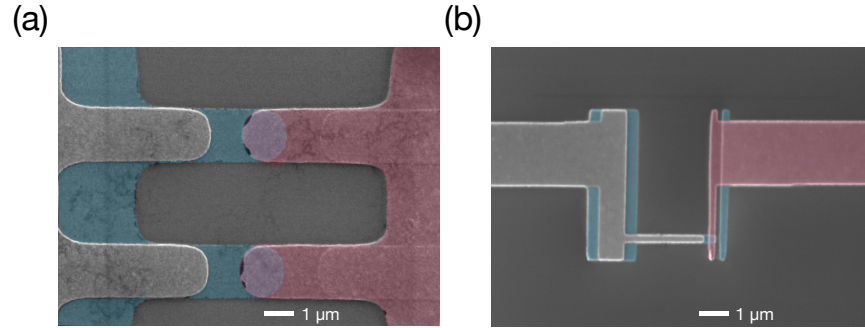


Figure 2.8: SEM images of junctions made with (a) photolithography and (b) eBL lithography. Images are at the same magnification. In each image, the bottom electrode is false-colored blue, and the top electrode is false-colored red. The overlap between electrodes defines the junction. The area of each junction in (a) is $2.88 \mu\text{m}^2$ whereas the junction's area in (b) is $0.08 \mu\text{m}^2$. Our oxidation process achieves similar critical currents despite the significant disparity in area.

In this section, we discuss the physical structure of large-area JJs. Because their patterns are defined with photolithography, the feature sizes are large compared to electron-beam lithography (eBL), see Figure 2.8. The large junction area significantly shifts the oxide barrier requirements, namely thickness and cleanliness.

TEM sample

To confirm the structure of the large-area JJ, we image a JJ cross-section with a transmission electron microscope (TEM). A focused ion beam (FIB) creates the cross-section using gallium ions to selectively mill regions of the JJ, as seen in Figure 2.9. The FIB first cuts away material surrounding the JJ. The FIB then thins the cut-away to $\sim 100 \text{ nm}$ to make the sample electron-transparent.

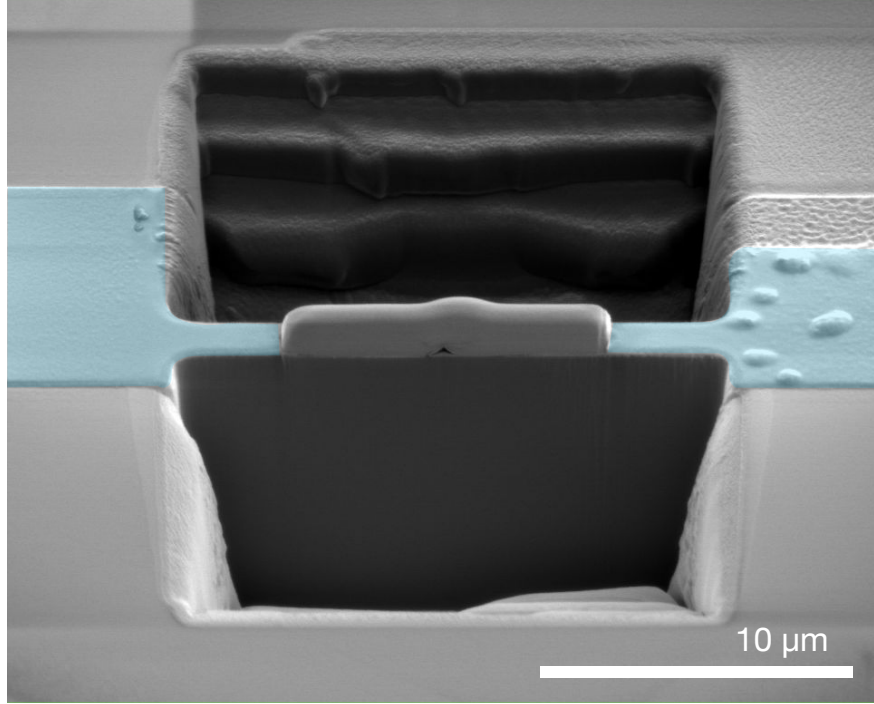


Figure 2.9: An SEM image of preparing a JJ for cross-sectional viewing. At this intermediate state, the FIB has cut away the majority of material and is preparing to separate the sample before thinning. The aluminum electrodes are highlighted in cyan. The junction (covered in a protective platinum layer) is visible as the black chevron in the image center . (This junction appears to have formed as a cusp on top of resist, see Figure 2.3b.)

With the sample prepared, we image the atomic configuration with a TEM. Electrons' small de Broglie wavelength allows TEM imaging to image with exquisite spatial resolution. Imaging capabilities can be combined with energy-dispersive x-ray spectroscopy (EDXS) to attain atomic-precision chemical abundance.

In Figure 2.10, we show EDXS data for a JJ made with two layers of oxidation, as described in Section 2.3.4. The magnification of this image is sub-optimal, but we nonetheless examine the JJ structure. We estimate the thickness of the aluminum oxide barrier with a Gaussian fit to the averaged oxygen abundance [see Figure 2.10(b)]. The fit returns an estimate of 4.5 nm, which is much larger than expected. However, we note that TEM imaging significantly

overestimates the size of the effective barrier [100]. TEM images reflect the structural properties (atom locations) of the barrier, but they do not capture the electronic properties. Quantitative X-ray photoelectron spectroscopy (XPS) would provide a better estimate of the true barrier thickness. This TEM imaging thus serves as an upper bound for the junction thickness.

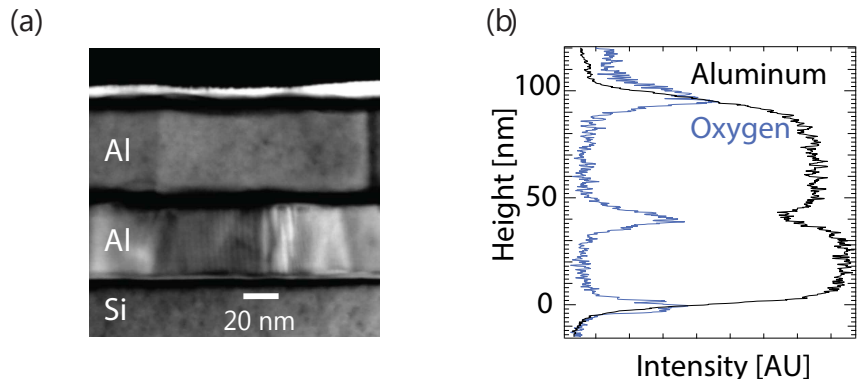


Figure 2.10: (a) Bright-field image from the EDXS measurement highlights the structural properties of the junction. Each aluminum layer and the silicon substrate are labeled, with respective oxides appearing as dark. Note the grain boundaries in the bottom aluminum layer. (b) EDXS chemical abundance averaged over the columns of panel (a). Blue indicates oxygen abundance, and black indicates aluminum abundance. The oxygen abundance in between the aluminum layer fits a Gaussian with a standard deviation of 4.5 nm.

Resistance Scaling: Evidence of Multiple Junctions

Section 2.2.3 described the dependence of normal resistance on the thickness of the junction barrier. This section describes a series of measurements investigating the resistance scaling with the number of layers applied with our multi-step oxidation scheme (see Section 2.3.4).

Figure 2.11(a) shows the resistance of JJs with a variable number (N_{layer}) of total oxide layers. Each layer after the first ($N_{\text{layer}} \geq 2$) is created with a 0.5 nm filler layer aluminum, so we expect the film thickness to be $(1.5 + 0.5N_{\text{layer}})$ [nm], based on an initial oxide layer's

thickness [95, 82, 96]. Despite the predicted exponential scaling, we see significantly sub-exponential scaling. Resistance in parallel with the junction can lower the measured resistance. We attribute the parallel resistance to the presence of two junctions.

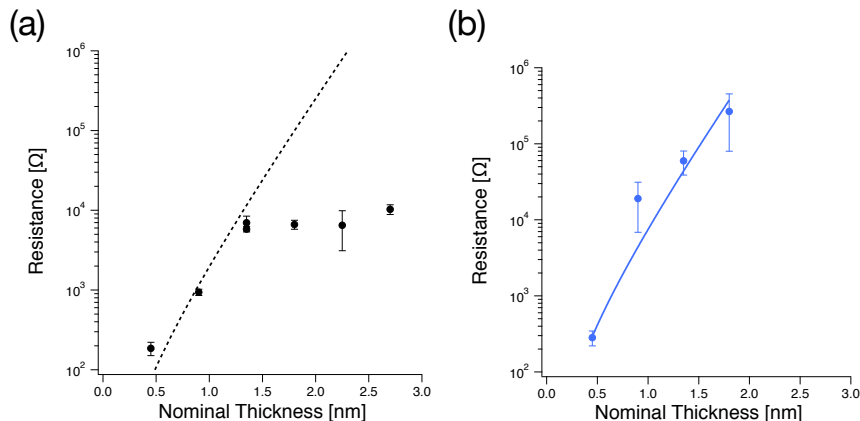


Figure 2.11: The room-temperature normal resistance for junctions with two evaporation schemes. (a) Electrodes are evaporated at $\pm 45^\circ$ with a number of oxide filler layers. As a function of the nominal oxide thickness (number of filler layers), the resistance does not scale exponentially, indicating the parallel resistance of a second junction. The dashed line is a guide to the eye based on the Simmons equation (Eqn. [2.15]). (b) Electrodes are evaporated at 10° and 60° , respectively, with a variable number of intermediate filler layers. The results can be fit to the Simmons equation, indicated by the solid blue line. Error bars in both figures correspond to multiple devices evaporated together.

Consider the geometry of the evaporation. After the first deposition at the standard angle of 45° relative to normal, a 30 nm electrode lies underneath the junction. The oxygen exposure oxidizes every face of the electrode. The next layer of filler aluminum only covers the top face of the electrode. The electrode's side face does not receive additional aluminum. The next oxidation contributes significantly to the top-face oxide's thickness because the filler aluminum oxidizes in the fast regime of Cabrera-Mott oxidation theory (see inset of Figure 2.1). However, the side-face oxide does not grow significantly because the oxide has entered the slow regime (see Figure 2.1). The process repeats for additional filler layers. When

the second electrode evaporates at -45° , two junctions are created. The oxide layer on the top face is thick, leading to high resistance. The resistance of this top-face junction' scales exponentially in N_{layer} . The oxide layer on the side face is thin, leading to lower resistance which is nearly independent of N_{layer} . The parallel is resistance is dominated by the lesser resistance of the side junction.

To confirm this model, we modify the oxidation procedure. Rather than evaporating layers at $\pm 45^\circ$, we evaporate layers at $+10^\circ$ and the final layer at $+60^\circ$. Because the evaporations approach from the same side of the bridge (ie the angles have the same sign), the filler layers build the full junction. The scaling of resistance with N_{layer} is shown in Figure 2.11(b). The exponential scaling indicates a single, thick junction has been created. We note that the finite resistivity of the silicon substrate slightly decreases the measured resistance.

2.4.2 Circuit Spectroscopy

These devices are intended for use in cQED experiments. Thus, we embed large-area JJs in a standard 3D cQED circuit. The circuit contains a SQUID (two JJs in a loop) and a shunt capacitor. The shunt capacitor should be large compared to the junction's capacitance so that the charging energy, E_C , is low enough to suppress charge noise (via low charge dispersion) [30]. The criteria for E_C and E_J is the transmon approximation: $E_J/E_C \gg 1$ [30].

E_J depends on the JJ critical current. Were we to follow the conventional transmon fabrication recipe for large-area JJs, the critical current would be too high, according to Equation [2.16]. But JJs fabricated with the procedure outlined in Section 2.3.4 have a transmon-suitable critical current (~ 10 nA).

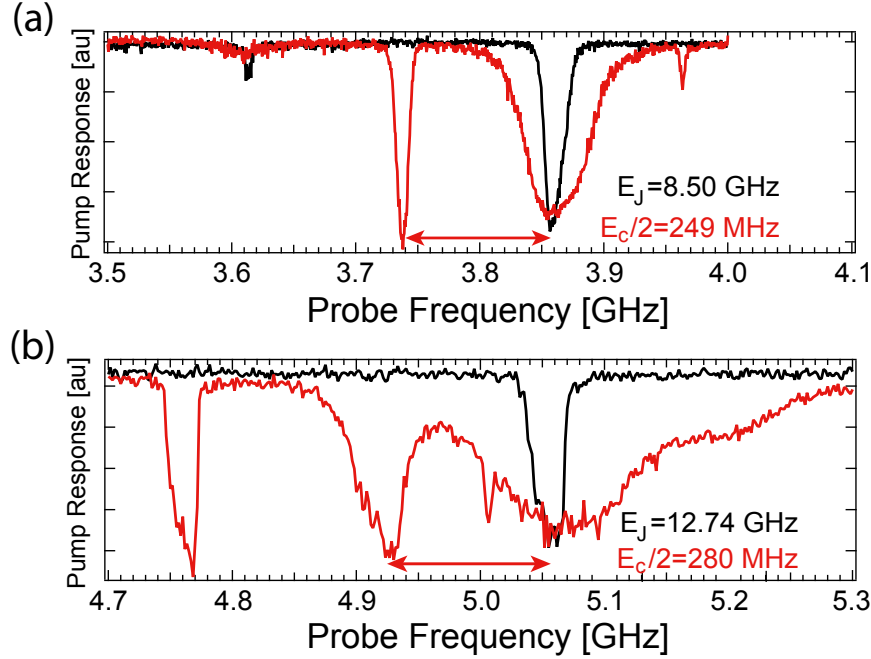


Figure 2.12: In both panels, two-tone spectroscopy probes the energy structure of the circuit. Lower probe power (black) only excites the first transition, $f_{01} = \sqrt{8E_J E_C} - E_C$. Higher probe powers (red) excite higher transitions separated by the circuit anharmonicity, $\alpha = -E_C$. (High power also induces significant power broadening). Arrows indicate $\alpha/2$, the frequency spacing of the two highest-frequency peaks. The extracted circuit energies, E_J and E_C are indicated for each device. Panel (a) corresponds to a device made with multiple oxide steps, and panel (b) corresponds to a device with a single oxidation step. Note the similar charging energies.

To verify the transmon approximation, we measure E_J and E_C . E_C can be found by measuring the circuit's anharmonicity. Moderate-power two-tone spectroscopy excites multi-photon transitions in the circuit. The highest frequency corresponds to the $|0\rangle \leftrightarrow |1\rangle$ transition. High probe power excites the next two transitions: $|1\rangle \leftrightarrow |2\rangle$ and $|0\rangle \leftrightarrow |2\rangle$, which are partially populated due to thermal excitation. Spectra like the one shown in Figure 2.12 exhibit dips at frequencies corresponding to each energy-level difference⁷: f_{01} , f_{12} , and $f_{02}/2$. The difference

⁷The factor of 2 is the number of photons required for the transition.

$\alpha \equiv f_{12} - f_{01}$ is the anharmonicity, and $E_C \approx -\alpha$ [30]. The transmon energy levels can be solved for E_J as a function of E_C and f_{01} .

Surprisingly, large-area JJs do not exhibit charging energies significantly different from their small-area counterparts, despite a 100 times enlargement of the area. The reason for similar charging energies is the presence of the two junctions, detailed in Section 2.3.4.

TLS Evidence

Early experiments in superconducting qubits with large areas showed evidence of many TLS defects [52, 53]. We show that insufficient surface cleaning may have significantly contributed to these results. We do so by excluding the BOE surface treatments and searching for spectroscopy signatures of TLSs.

At minimal probe power, two-tone spectroscopy does not saturate TLS, allowing excitations to swap between the qubit and the TLS. Strong TLS-qubit coupling significantly shifts the qubit frequency [114, 55], resulting in avoided crossings in spectroscopy. Spectroscopy of four devices with sufficiently low power exhibited four total resolved (strongly coupled) avoided crossings. Two devices exhibited no avoided crossing, and two devices exhibited two avoided crossings each. This finding is consistent with the colloquial wisdom that TLS occurrences are stochastic so that some devices are “unlucky”.

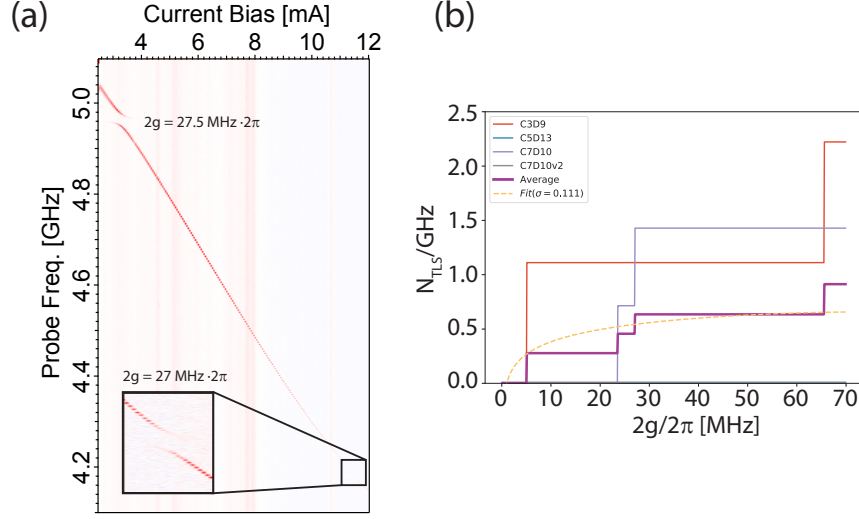


Figure 2.13: (a) An example of avoided crossings as a qubit transition frequency comes into resonance with a strongly coupled TLS. The coupling strength is given by the maximal separation, $2g$, as indicated. (b) The cumulative density of splitting for multiple qubits (see legend). The average density (purple) and a fit to the standard TLS model (yellow dashed) estimates the total defect density, $\sigma = 0.11 N_{\text{TLS}}/\text{GHz}/\mu\text{m}^2$.

An estimate for the total TLS density results from combining the TLS count over the swept qubit-frequency range with the known area of the junctions [52]. Figure 2.13 contains the cumulative distribution function of TLS coupling strengths, along with a fit to the standard TLS model [115, 52, 116]:

$$N_{\text{TLS}} = A \sigma \sqrt{\frac{1}{g^2} - \frac{1}{g_{\text{max}}^2}} \quad (2.17)$$

The TLS density in these non-BOE cleaned devices is $\sigma = 1.1/\text{GHz } \mu\text{m}^2$, consistent with other measurements [52, 53]. Because the JJs in these devices have 100-times larger insulating barriers, we expect these devices should host significantly more defects.

For devices that received surface treatments, we do not observe strongly-coupled TLS with sufficient statistics to fit. However, the absence of spectroscopically-resolved (strongly coupled)

defects does not imply the absence of defects. Recent experiments using DC electric fields to directly tune TLSs have shown that only 3% of TLS are strongly coupled to the qubit[80].

2.4.3 Time Domain Measurements

Having examined the energy properties of the circuits with large-area JJs, we have confirmed their transmon nature. Now, we turn to the time domain to measure their coherence properties, especially T_1 .

T_1 Without Surface Cleaning

When a qubit is near resonance with a TLS, the decay rate is highly sensitive to the TLS state, due to an increase in the environmental density of states. With fluctuations of the TLS state, T_1 fluctuates in the presence of TLS [54, 55, 56]. Having identified regions where TLS strongly couple to the qubit through spectroscopy, we can compare the T_1 behavior to these regions. For the same device pictured in Figure 2.13(a), we measure T_1 across a range of qubit frequencies multiple times over the course of 40 hours. Figure 2.14 shows the effects of TLS state-switching. Our sweeping rate for flux is relatively slow, so the sampling rate for T_1 at a particular qubit bias is only once per five minutes. Therefore, the measurement is not sensitive to diffusive or telegraphic statistics of the TLS [55]. We note that the T_1 values for this qubit are also significantly influenced by Purcell decay.

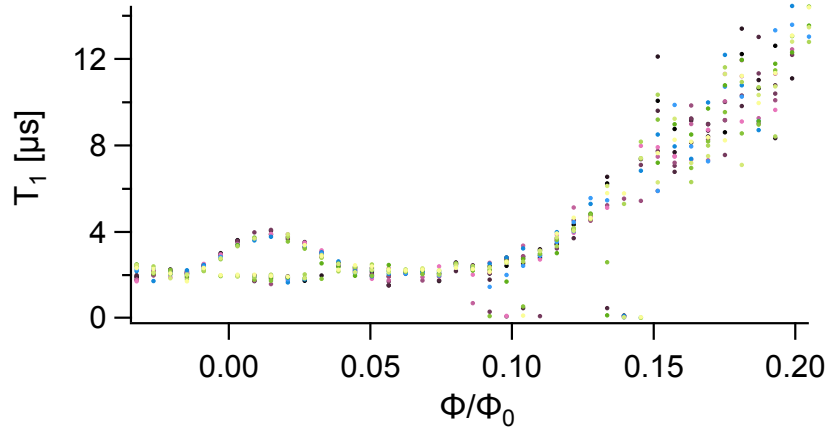


Figure 2.14: The T_1 time of a device that did not receive surface cleaning. We repeatedly sweep through flux biases for several hours and measure T_1 . Near 0 bias, T_1 oscillates between two steady states—a clear signature of TLS state-switching. T_1 is further suppressed by the Purcell effect, given the small detuning, $\Delta_{\min} = 0.235$ MHz.

T_1 With Surface Cleaning

TLSs reside at interfaces [81]. Thus, surface cleaning processes [117, 118, 68, 83] are essential. The next generation of large-area transmons was cleaned with BOE both before spinning resist and before evaporation pump down. BOE-cleaned devices exhibit significantly fewer strongly-coupled defects in spectroscopy. The absence of strongly-coupled defects does not imply the absence of a weakly-coupled bath of defects [116, 57]. However, the difficulty of probing these kinds of TLS forces us to turn to less direct probes of TLS activity.

We perform similar repeated measurements of T_1 over hour-long timescales. The statistics of these measurements hint at the abundance of TLS. Because the qubits have significantly different frequencies, f_{01} , T_1 should not be directly compared between the devices. Instead,

we utilize the quality factor:

$$\frac{1}{Q} = \frac{1}{T_1^{\text{tot.}} \cdot 2\pi f_{01}} = \sum_i p_i \tan \delta_i + \frac{1}{T_1^{\text{other}} \cdot 2\pi f_{01}}. \quad (2.18)$$

Q provides a time-scale invariant metric for qubit loss by directly connecting to dielectric losses, $\tan \delta_i$, weighted by participation ratios, p_i [74, 116, 68, 57, 29]. T_1^{other} indicates the coherence time as limited by other factors such as Purcell decay and quasi-particles.

In Figure 2.15, we plot histograms of Q measurements for each of three devices receiving different cleaning treatments. The substrate of the first device received no surface cleaning upon receipt from the manufacturer. The next substrate was cleaned with a 5-minute BOE dip before spin coating. After pattern development and ashing, the wafer received another BOE dip for 30 seconds. The third substrate was cleaned with a Piranha solution (3:1 mixture of H_2SO_4 and H_2O_2 at 120°) for 10 minutes along with a 5-minute BOE dip before spin coating. This device also received a 30-second BOE dip after development and ashing.

Additional cleaning steps lead to a marked improvement in Q . The uncleaned device which exhibited strongly coupled TLS (Fig. 2.14) exhibits a long, non-Gaussian tail in its Q distribution. We associate this with the TLS state switching away from the qubit, allowing higher-than-average Q (T_1). However, we note that the device which received multiple cleaning treatments also exhibits extended tails. With an overall improvement in the loss rate, the qubit appears more sensitive to fluctuations of weakly coupled defects. Using Fermi's golden rule, the density of (TLS) states has decreased, but the transition matrix element is unaffected. The low decay rate can thus significantly shift with TLS fluctuations. We also note that T_1 for the doubly-cleaned was not monitored for as long as for the other devices, so the statistical uncertainty is higher.

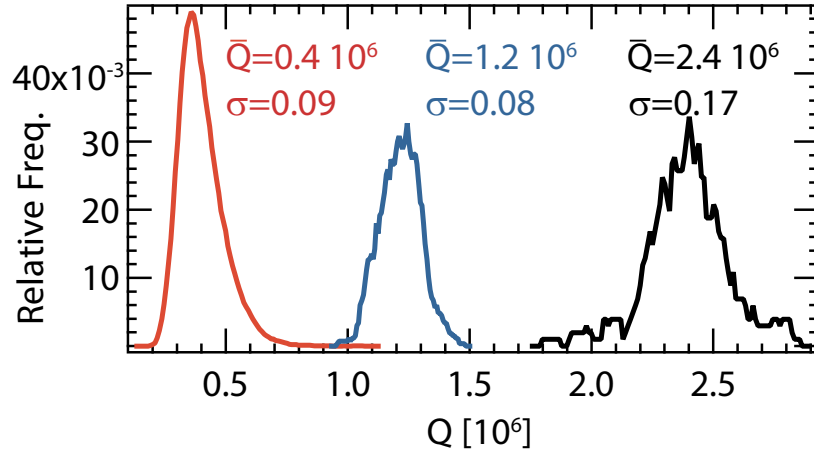


Figure 2.15: Distributions of quality factors measured for multiple hours for three devices under different cleaning conditions. Red curve: (same as in Fig. 2.14) no surface cleaning; blue curve: BOE dip for 5 minutes before spin coating, a 30-second dip before evaporation; black curve: Piranha cleaned for 10 minutes, BOE clean before spin coating. The average Q and standard deviation of Q are indicated for each device.

Aging T_1

While T_1 can vary significantly over a batch of devices, T_1 of a single device can also vary significantly from run to run. In Figure 2.16, we show Q data as a function of a qubit's age: the time between fabrication and cooldown. Most qubits are cooled within a few days of fabrication, but we have occasionally returned to old batches. While not cold, qubits are stored in ambient conditions. We find that in these few tests, T_1 can significantly degrade. We suspect that large area JJs are more susceptible to aging due to the increased surface area on which oxygen and other contaminants can adsorb [119, 120]. Similar effects have been observed in resonators [121] and qubits [122] after multiple cooldowns.

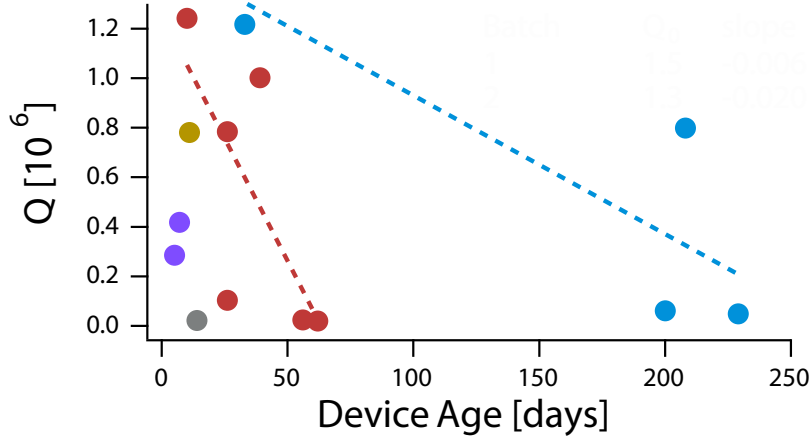


Figure 2.16: Quality factor measurements for qubits from the same batches (color) as a function of age (time between fabrication and cooldown). Dashed lines are guides to the eye, signifying mostly negative trends.

2.4.4 Additional Noise Sources

We have primarily focused on T_1 effects due to TLS defects. While other mechanisms also affect T_1 such as Purcell decay, other material losses, packaging modes, their contributions are expected to be small (see Refs. [123, 90, 122] and references therein for detailed reviews). However, at the current level of T_1 , quasiparticle (QP) tunneling can significantly contribute to T_1 loss.

QP tunneling occurs when a single electron is excited out of the superconducting ground state and tunnels across the JJ barrier. The tunneling event drives transitions between the qubit's energy states (favoring excited state to ground transitions), leading to T_1 decay [124, 125]. At thermal equilibrium with a 10 mK environment, the number of QP tunneling events is effectively 0, due to exponential scaling in the temperature. However, incident photons with frequencies above the superconducting gap of aluminum ($\Delta = 50$ GHz) can induce nonequilibrium QP transitions [124, 125, 126, 127].

To mitigate QP, we extensive shielding and cable filtering. At the dilution refrigerator’s base plate, we surround qubit-cavity enclosures with a black-coated copper shield to absorb tray infrared radiation. The coating is a mixture of carbon-lack powder, stycast epoxy, and SiC granules [128, 129, 130].

Shielding limits radiation from nearly the full 4π steradians, but RF lines remain as an entry path. We include absorptive low-pass filters to further attenuate infrared radiation in the lines. Our homemade filters are either stripline or coax transmission lines with a lossy dielectric. The dielectric contains magnetic particles which absorb high-frequency radiation [131]. Typical attenuation is 3 dB at 6 GHz and 70 dB at 50 GHz. Evidence suggests that filters are most effective against QP when placed inside the can [90].

2.4.5 Limits on Loss Tangents

Devices with high coherence times can be used as upper bounds for the intrinsic loss tangents of materials [132, 133, 134]. High coherence devices have focused on loss tangents for substrate materials such as silicon [135, 136] and sapphire [137, 138, 139]. But our devices emphasis the loss tangent of the aluminum oxide barrier.

Our highest $Q = 2.8 \cdot 10^6$ device allows us to contribute to the body of estimates for the loss tangent of aluminum oxide [132, 140]. Assuming published $(p, \tan \delta)$ values for metal-substrate interface $(10^{-4}, 10^{-4})$, metal-air interface $(10^{-5}, 10^{-2})$, surface-air interface $(10^{-4}, 10^{-4})$, and silicon $(10^{-1}, 10^{-7})$ [52, 141, 74, 67, 122] (contributing a net $1/Q = 1.1 \cdot 10^{-7}$), we estimate an upper bound on the loss tangent of AlO_x of $2.3 \cdot 10^{-6}$. While this is lower than the current limit, $4 \cdot 10^{-8}$ [132], further coherence improvements may set a lower bound.

Chapter 3

Entropic Uncertainty Relations

3.1 Introduction

Uncertainty relations provide limits to precision metrology [142, 143], amplification [144, 145], and measurement-based feedback [15]. The minimal amount of noise achievable is lower-bounded in uncertainty relations. They highlight how quantum noise arises from disagreement between, or incompatibility of, quantum operations. They predict lower limits on the measurement uncertainty of incompatible measurement operators, such as the position and momentum of an electron, as in Heisenberg's original thought experiment [146]. The uncertainty extends to measurement operators which are not conjugate pairs. For any Hermitian quantum operators, A and B , Robertson proved [147] the textbook uncertainty relation:

$$\Delta A \Delta B \geq \frac{1}{2} | \langle \psi | [A, B] | \psi \rangle | \quad (3.1)$$

where ΔA (ΔB) denotes the standard deviation of repeated A (B) measurements for identically prepared systems with state $|\psi\rangle$ [147].

3.1.1 Problems with Variance-based Uncertainty Relations

Variance is often used to quantify uncertainty. The variance of a probability distribution for a random discrete variable x is

$$\text{var}(\{p_x\}) = \sum_i p_i \cdot (x_i - \bar{x})^2. \quad (3.2)$$

Variance measures a probability distribution's expected deviation from its mean and thus quantifies the spread of a distribution. However, this deviation is an inappropriate metric for uncertainty when applied to finite-dimensional operators [148, 149].

Consider a spin-1 particle in a maximally mixed state between its three possible values: $s_j \in \{-1, 0, +1\}$. The variance is $\frac{1}{3}(-1)^2 + \frac{1}{3}(0)^2 + \frac{1}{3}(1)^2 = \frac{2}{3}$. Suppose we perform a measurement that excludes the possibility that $s_j = 0$. We have gained information by decreasing the number of possibilities. Yet the variance has *increased* to $\frac{1}{2}(-1)^2 + \frac{1}{2}(1)^2 = 1$.

Variance inherits the units of its underlying random variable. This makes variance undesirable for uncertainty relations because eigenvalue labels can confound the underlying goal of uncertainty relations. For example, in the above spin-1 example, the story changes if the measurement excludes $s_j = +1$ instead of $s_j = 0$. The same number of outcomes have been excluded, yet the change in variance is different.

As a unitful quantity, variance is also incompatible with nonnumerical quantities. Neutrino mass-eigenstates oscillate between flavors: “electron”, “muon”, and “tau” [150]. Treated as a three-outcome observable, a flavor measurement's uncertainty cannot be quantified with variance [151]. Entropy, on the other hand, only applies to the probability of an outcome, not to the value of the outcome.

The bound of Inequality [3.1] has a few shortcomings as well [148]. From the relation, we would like to gather that quantum measurements are noisy by virtue of measurement operators themselves, namely their failure to commute. However, the bound depends also on the prepared state. Thus, the Robertson-Heisenberg uncertainty relation, unfortunately, doesn't relate quantum measurement uncertainty with quantum measurements alone. Besides lacking aesthetic purity, state-dependence makes the bound inapplicable to cryptography applications, where the state is often unknown and/or prepared by an adversary [152].

Of particular interest is the uncertainty relation for σ_x and σ_z . Inequality [3.1] implies that the bound is $\frac{1}{2} |\langle \psi | \sigma_y | \psi \rangle|$. For any state in the X - Z plane of the Bloch sphere, the bound is zero—equivalent to the trivial bound. For an eigenstate of σ_x or σ_z , the trivial bound is tight (the LHS of the inequality matches the RHS). However, in this case, nothing is conveyed about the second measurement's uncertainty, which is multiplied by zero—the first measurement's variance. The bound is tight only because the product of a minimal uncertainty state with a maximal uncertainty state is zero. So the tightest bound conveys no information about the outcomes.

In our measure of uncertainty, we desire a quantity which appropriately represents the information content (or uncertainty due to lack thereof) of measurements. We then want to make meaningful statements of the bounds for such a measure.

3.1.2 Entropic Uncertainty Relations

Modern uncertainty relations replace the product of variances with the sum of entropies [153]. Entropy, unlike variance, directly pertains to the information content of a probability

distribution. The Shannon entropy of a probability distribution is

$$H(\{p_x\}) = \sum_i p_i \cdot \log_2 \left(\frac{1}{p_i} \right). \quad (3.3)$$

As the expected value of “surprisal” ($\log \frac{1}{p}$), entropy ideally quantifies the *information content* of a probability distribution.

Besides improving the deficiency for variance-based uncertainty relations, entropic uncertainty relations make connections between fields like thermodynamics and quantum cryptography [152]. In addition to answering the above concerns, entropic relations also provide bounds for connected sectors of quantum information science. For example, quantum cryptography findings often base the capacity of quantum channels on entropic uncertainty relations [153].

A seminal result from Maassen and Uffink [154] displays the advantages of entropic uncertainty relations. For an A measurement of a system described by density matrix ρ , suppose outcome a occurs with probability p_a . The operator A has a Shannon entropy via the a probability distribution:

$$H(A)_\rho = - \sum_a p_a \log_2 p_a. \quad (3.4)$$

With an analogous $H(B)_\rho$, Maassen and Uffink proved

$$H(A)_\rho + H(B)_\rho > - \log c. \quad (3.5)$$

c denotes the *maximum overlap* between any eigenstates, $|a\rangle$ and $|b\rangle$, of the observables’ eigenstates: $c = \max_{a,b} \{ |\langle b|a\rangle|^2 \}$.

Inequality [3.5] improves the weakness of Inequality [3.1]. First, the new bound is independent of the state ρ . Second, entropy depends only on probabilities, in contrast with variance which

depends on both probabilities and outcome. Finally, the smallest minimum in the bound of Inequality [3.5] is zero: minimum uncertainty in all cases occurs when observable eigenvectors coincide, leading to a maximum overlap of $c = 1$ and thus a bound of zero.

The work of this chapter centers on including a weak measurement in an entropic uncertainty relation. Weak measurements illuminate quantum dynamics, as in the tracking of the progress of spontaneous emission [12, 11], the catching and reversing of quantum jumps [13], and observations of noncommuting observables' dynamics [7]. Here, we ask what role weak measurements play in operator incompatibility. We find that weak measurements can decrease the uncertainty between otherwise incompatible observables.

In the process of including a weak measurement in the uncertainty relation, we find that a weak value naturally appears. Weak values' significance and utility have been debated across theory and experiment [21, 22, 23, 24, 25]. Our work demonstrates how weak values have physical meaning in uncertainty relations. As we will see, weak values decrease the incompatibility between incompatible observables.

Other experimental work has explored entropic uncertainty relations with various platforms, including neutrons, optics, and nitrogen-vacancy centers [155, 156, 157, 36]. The measurements in [36], though nonprojective, are probabilistic projections. In contrast, our measurements are weak and experimentally demonstrate the weak value's role in reconciling incompatible operations.

Uncertainty relations occupy two categories [153], one centered on measurement outcomes' unpredictability [157, 36] and one centered on measurements' disturbance of quantum states [155, 156]. Our uncertainty relation occupies both categories, similar to some optical photon experiments [158]: on the one hand, we prepare an eigenstate of one measurement operator and perform a measurement of an incompatible measurement operator. On the other

hand, we take advantage of the weak measurement’s disturbance of the initial eigenstate. This work identifies weak measurements as a means to unify the classes of uncertainty relations.

Let us now turn to the underpinnings of our entropic uncertainty relations for weak measurements.

3.2 Theory

The progress of uncertainty relations is the gradual tightening of bounds for ever-more-complicated operators. In this section, we describe the derivation of our central entropic uncertainty relation governing weak measurements. The path will begin with several bounds for familiar projective operators (called projector-valued measures, PVMs). Then, we will generalize the operator to positive operator-valued measures, POVMs.

In every example, the uncertainty relation centers on the disagreement between two operators. The LHS of the inequality is constructed as the sum of two entropies—one for each of the operators. The calculation of the entropy depends on the details of the operator, but the process boils down to calculating the Shannon entropy for probabilities of outcomes.

The RHS of each inequality is an attempt to leverage various facts about entropies to derive as tight of a bound as possible. The relevant facts are often geometric. The arguments rely on the correspondence between entropies and distances: Consider a probability distribution over N outcomes has an N -dimensional vector. The (Rényi) entropy of the probability distribution is proportional to the logarithm of the vector’s norm (of degree α):

$$H_\alpha(\{p\}) = \frac{\alpha}{1-\alpha} \log \|\vec{p}\|_\alpha \tag{3.6}$$

For reference, the 3-norm of vector \vec{x} is $\|\vec{x}\|_3 = \left(\sum_j x_j^3\right)^{\frac{1}{3}}$, and the 2-norm of a vector is the well-known Euclidean distance. The Shannon entropy is equal to the Rényi entropy of degree 1. The above equation implies that the uncertainty of a probability distribution is related to how extended the distribution is over its support: If the probability amasses on one outcome, the extent is small and the uncertainty is low.

The profound mathematical fact of uncertainty relations is that not all vector spaces (quantum operators) that host the probability vector (quantum state) are equally efficient. In terms of entropy, some operators require more bits of information to represent the same intrinsic probability distribution (quantum state).

Let us work up to this fact through simpler examples.

3.2.1 Trivial Bound

The simplest bound for entropic uncertainty relations uses elementary properties of probabilities [159]. Probabilities⁸ are quantities between 0 and 1. The logarithm of a quantity between 0 and 1 is always negative, and the probability is always positive. The entropy, $-p \log p$, is a negated product of the logarithm with the probability—a positive quantity. This relation gives the trivial bound for the sum of two entropies:

$$H_\rho(A) + H_\rho(B) \geq 0. \tag{3.7}$$

Equality depends on the limit $-p \log_2 p \rightarrow 0$ as $p \rightarrow 0$.

⁸Certain representations of quantum states such as the Wigner function use quasi-probabilities which can be negative.

3.2.2 Deutsch Bound

David Deutsch used simple algebraic features of quantum states to improve the bound [148].

Consider the expanded expression for the sum of entropies:

$$H_\rho(A) + H_\rho(B) = \sum_a -|\langle a|\psi\rangle|^2 \log_2 (|\langle a|\psi\rangle|^2) + \sum_b -|\langle b|\psi\rangle|^2 \log_2 (|\langle b|\psi\rangle|^2) \quad (3.8)$$

where the presumed pure state $\rho = |\psi\rangle\langle\psi|$ has been replaced with its ket representation. With the identity, $\sum_x |\langle x|\psi\rangle|^2 = 1$, Equality [3.8] rearranges into an expression that conjoins probabilities of the two operators.

$$\begin{aligned} H_\rho(A) + H_\rho(B) &= \sum_{a,b} -|\langle a|\psi\rangle|^2 |\langle b|\psi\rangle|^2 [\log_2 (|\langle a|\psi\rangle|^2) + \log_2 (|\langle b|\psi\rangle|^2)] \\ &= \sum_{a,b} -|\langle a|\psi\rangle|^2 |\langle b|\psi\rangle|^2 \left[\log_2 \left(\langle\psi|a\rangle \langle a|\psi\rangle \langle\psi|b\rangle \langle b|\psi\rangle \right) \right]. \end{aligned} \quad (3.9)$$

Now we may leverage some properties of quantum states. The maximum value for the square-bracketed factor corresponds to the state which bisects the eigenstates. The state corresponds to $\psi_{\text{bisector}} = \frac{1}{\sqrt{2(1+|\langle a|b\rangle|)}} (|a\rangle + e^{-i\theta} |b\rangle)$, where we've used $\theta = \arg(\langle a|b\rangle)$. This state bounds the logarithm factor in Equality [3.9]:

$$\log_2 \left(\langle\psi|a\rangle \langle a|\psi\rangle \langle\psi|b\rangle \langle b|\psi\rangle \right) \leq 2 \log_2 \left[\frac{1}{2} (1 + |\langle a|b\rangle|) \right]. \quad (3.10)$$

Replacing each term in the sum with its maximal⁹ value leads to the Deutsch entropic uncertainty relation:

$$H_\rho(A) + H_\rho(B) \geq \min_{a,b} \left\{ -2 \log_2 \left[\frac{1}{2} (1 + |\langle a|b\rangle|) \right] \right\} \quad (3.11)$$

⁹The maximum becomes a minimum with the leading negative sign.

Note how state removal transformed the equality into an inequality.

3.2.3 Maassen-Uffink Bound

Hans Maassen and Jos Uffink slightly improved this bound while extending the relation to include an entire class of (Rényi) entropies [154]. The class of entropies corresponds to the different norms of the probability distribution (treated as a vector). Our targeted (Shannon) entropy is a special case of the generalization (using the 1-norm).

Maassen and Uffink apply a result from complex analysis known as the Riesz-Thorin interpolation theorem. The theorem applies to transformations of complex-valued vectors which preserve length. Here, the complex-valued vectors are inner products $x = \langle a|\psi\rangle$, and the transformation is a basis transform: $T : \langle a|\psi\rangle \rightarrow \langle b|\psi\rangle$. Thus formulated, the Riesz theorem states:

$$c^{\frac{1}{n}} \left(\sum_j |Tx_j|^n \right)^{\frac{1}{n}} \leq c^{\frac{1}{m}} \left(\sum_j |x|^m \right)^{\frac{1}{m}}, \quad (3.12)$$

where c is the maximum transformation matrix element: $c = \max_{a,b} |\langle b|a\rangle|$. For choices of m and n which select the Shannon entropies, the Maassen-Uffink relation states:

$$H_\rho(A) + H_\rho(B) \geq \min_{a,b} \{-2 \log_2 |\langle b|a\rangle|\}. \quad (3.13)$$

This uncertainty relation provides a direct comparison to our uncertainty relation in the absence of the weak measurement. We will refer to it elsewhere.

3.2.4 Tomamichel Bound

The primary bound for this thesis is an application of a bound derived by Marco Tomamichel [152] and adapted by Nicole Yunger Halpern, Anthony Bartolotta, and Jason Pollack [160]. The bound generalizes the previous results from projector-valued measures (PVM) such as projectors of Pauli operators to positive operator-valued measures (POVM). The generalization is essential in describing weak measurements which do not project the system of interest.

The general uncertainty relation follows a similar path to the Maassen-Uffink relation. The bound depends on the “distance” (inner product) between the quantities of interest. The Maassen-Uffink bound depends on the distance between eigenvectors of the operators. The Tomamichel bound depends on the distance between POVMs. The operator-norm quantifies the distance between two POVMs, \mathcal{A}_a and \mathcal{B}_b :

$$\|\mathcal{A}_a\mathcal{B}_b\| = \lim_{\alpha \rightarrow \infty} \text{Tr} \left\{ \left[\sqrt{(\mathcal{A}_a\mathcal{B}_b)^*(\mathcal{A}_a\mathcal{B}_b)} \right]^\alpha \right\}^{\frac{1}{\alpha}}. \quad (3.14)$$

The derivation of the bound follows again from the Riesz-Thorin interpolation theorem [161], now applied to this operator norm. The bound states

$$H_\rho(\mathcal{A}) + H_\rho(\mathcal{B}) \geq \min_{a,b} \left\{ -\log_2 \|\mathcal{A}_a\mathcal{B}_b\|^2 \right\}. \quad (3.15)$$

The next section describes the application of this bound to the particular POVMs of interest.

3.2.5 Weak Measurement Bound

The first operator in our weak measurement uncertainty relation is a projective Pauli operator. We choose to fix this operator as σ_z , amounting to a choice of the coordinate

system. Measurements of this initial operator result in an outcome $i \in \{-1, 1\}$. The second operator is a composition POVM. It combines a weak-measurement Kraus operator with a final projective Pauli operator: AF . As such, measurements of this POVM result in a tuple of outcomes, (j, f) , for the weakly-measured component and the strongly-measured component.

Let us consider the entropies of each operator in detail. The entropy of the initial σ_z measurement follows from Equation [3.4]. The entropy of the joint-measurement POVM is calculated for the joint probability of (j, f) outcomes. j is a continuous variable, and so the Shannon entropy¹⁰ would not be well-defined. However, weak measurements are experimentally discrete quantities due to finite detector resolution. Thus, the Shannon entropy is calculated over a finite sum:

$$H(AF)_\rho = \sum_{j,f} p_{j,f} \log_2 p_{j,f} \quad (3.16)$$

The range of j depends on the detector settings (see Sect. 3.3). The sum of the two entropies yields the LHS of the EUR.

Now consider the bound. The Yunger Halpern-Bartolotta-Pollack bound [160] is an application of the Tomamichel bound to the POVM describing weak measurements. We aim to describe the uncertainty between two POVMs. The POVM for the first strong (projective) measurement of \mathcal{I} is $\{\Pi_i\}$. The set contains elements corresponding to each outcome $i = \pm 1$. The second POVM for the joint weak-strong measurement of AF is $\{\Pi_f K_j\}$, where the Kraus operator

$$K_j = \left(\frac{\delta t}{2\pi\tau} \right)^{1/4} \exp \left(-\frac{\delta t}{4\tau} [jI - A]^2 \right) \quad (3.17)$$

describes the weak measurement of operator A with outcome j [49].

¹⁰The differential entropy quantifies information in the case of continuous-variable probability distributions.

In the Tomamichel form, the calculation of the operator norm results in an expression that depends on a maximal eigenvalue and is not directly accessible to experiments [162]. Instead, experiments access expectation values of eigenvalues. We use the monotonicity¹¹ of vector norms to translate the expression into an experimentally accessible form. In particular, the operator norm (which uses infinite degree) is less than the 1-norm:

$$\|\mathcal{O}\| = \lim_{\alpha \rightarrow \infty} \sqrt{\text{Tr} [\mathcal{O}^{\frac{\alpha}{2}}]^{\frac{2}{\alpha}}} < \sqrt{\text{Tr} [\mathcal{O}]}. \quad (3.18)$$

By measuring expectation values (the RHS above), we get a quantity which upper-bounds the infinite norm. This inequality admits experimental tests at the cost of a loosened bound.

With this expression, we can formulate the bound of our uncertainty relation. We use the norm between the POVMs $\|\mathcal{I} \cdot \mathcal{WF}\|$. The entropy of the two POVMs is bounded as:

$$H_{\rho}(\mathcal{I}) + H_{\rho}(\mathcal{WF}) \geq \min_{i,j,f} \left\{ -\log_2 \left(\text{Tr} \left[\Pi_i K_j^{\dagger} \Pi_f K_j \right] \right) \right\}. \quad (3.19)$$

Some simplification is in order. Because the measurement is weak, we can Taylor expand the Kraus operator using the strength of the measurement as a smallness parameter:

$$K_j = \sqrt{p_j} (I + g_j A) + O(g_j^2). \quad (3.20)$$

$\sqrt{p_j} = \left(\frac{\delta t}{2\pi\tau}\right)^{1/4} \exp\left(-\frac{\delta t}{4\tau} [j^2 + 1]\right)$ is the prefactor to I and describes the probability of obtaining outcome j if the detector is not coupled to the system. $g_j = \frac{\delta t}{2\tau} j$ is the prefactor to A (combined with $\sqrt{p_j}$) and is thus related to the amount of backaction from the weak measurement. Section 3.3.2 discusses the measurement of these quantities.

¹¹Monotonicity states that norms decrease with increasing order: $\|x\|_i > \|x\|_j$ when $i < j$.

The detailed simplification below shows how the weak value directly appears in the bound of our uncertainty relation. We plug the Taylor-approximated form of the Kraus operator into the bound of Inequality [3.19]. The result is:

$$\begin{aligned}
& -\log_2 \left\{ \text{Tr} \left[\Pi_i K_j^\dagger \Pi_f K_j \right] \right\} \\
&= -\log_2 \left\{ \text{Tr} \left[\Pi_i \sqrt{p_j} (I + g_j^* A^\dagger) \Pi_f \sqrt{p_j} (I + g_j A) \right] \right\} \\
&= -\log_2 \left\{ p_j \text{Tr} [\Pi_i \Pi_f] + p_j \text{Tr} [\Pi_i g_j^* A^\dagger \Pi_f + \Pi_i \Pi_f g_j A] \right\} \\
&= -\log_2 \left\{ p_j \text{Tr} [\Pi_i \Pi_f] + p_j \text{Tr} [\Pi_i \Pi_f] \left(\frac{\text{Tr} [(\Pi_f g_j A \Pi_i)^*]}{\text{Tr} [\Pi_f \Pi_i]} + \frac{\text{Tr} [\Pi_f g_j A \Pi_i]}{\text{Tr} [\Pi_f \Pi_i]} \right) \right\} \tag{3.21} \\
&= -\log_2 \{ p_j p_{f|i} \} - \log_2 \{ 1 + 2\Re(g_j A_{\text{wv}}) \} \\
&\approx -\log_2 \{ p_j p_{f|i} \} - \frac{2}{\ln 2} \Re(g_j A_{\text{wv}})
\end{aligned}$$

With this, we have the final form of our entropic uncertainty relation:

$$\boxed{H_\rho(\mathcal{I}) + H_\rho(\mathcal{WF}) \geq \min_{i,j,f} \left\{ -\log_2 \{ p_j p_{f|i} \} - \frac{2}{\ln 2} \Re(g_j A_{\text{wv}}) \right\}} \tag{3.22}$$

3.3 Experiment

Here we describe the experimental results for measuring each side of the uncertainty relation derived in the last section [163]. We first focus on entropies before moving onto bounds. The entropy results highlight two distinct components of uncertainty relations. First, *preparation uncertainty* results from incompatibility between a measurement and the underlying state. For example, a position eigenstate is incompatible with momentum measurements. Second, *disturbance uncertainty* relates to the measurement-induced backaction imparted on the state. For example, a linear combination of position states collapses into a single position upon measurement.

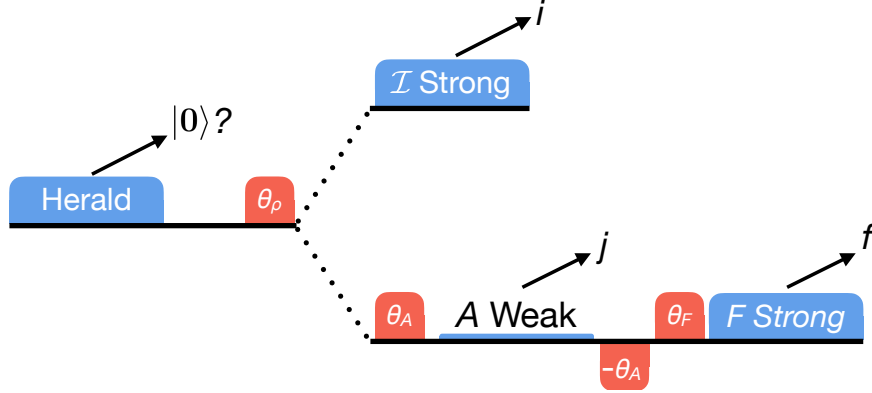


Figure 3.1: Pulse sequences measuring both $H(\mathcal{I})_\rho$ (top branch) and $H(AF)_\rho$ (bottom branch). Blue pulses gate the cavity frequency, and red pulses gate the qubit frequency (single-sideband modulation not shown). The outcomes of each measurement i , j , and f are shown with their respective cavity pulses.

We measure the entropic uncertainty relation with a transmon superconducting qubit. The qubit couples to one mode of the electromagnetic field in a three-dimensional microwave cavity. The qubit frequency, $\omega_q/(2\pi) = 3.889$ GHz, is far detuned from the cavity frequency, $\omega_c/(2\pi) = 5.635$ GHz, enabling a dispersive interaction. Dispersive interactions do not exchange energy, allowing for quantum-nondemolition measurements (see Sect. 1.3.1).

3.3.1 Entropies of the Entropic Uncertainty Relation

Entropy measurements of the two observables are performed with the following sequence (see Figure 3.1). We herald the ground state by strongly measure σ_z at the beginning of each repetition. Having projected the qubit into either $|0\rangle$ or $|1\rangle$, we discard experimental runs in which the qubit was not in the ground state. A resonant qubit drive rotates the qubit state by θ_ρ to prepare the initial state, ρ . We then perform one of two measurements, \mathcal{I} or AF . The first measurement, $\mathcal{I} = \sigma_z$, results in outcomes $i = \pm 1$. The relative frequencies sample the probability distribution of \mathcal{I} , p_i .

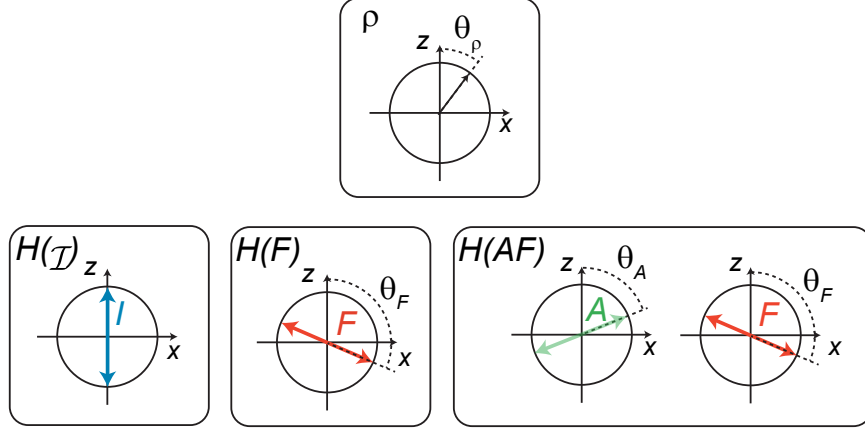


Figure 3.2: Each preparation and measurement is characterized by an angle in the X – Z plane of the Bloch sphere. Measurements at a specified orientation are proceeded with to align the measurement axis with the Z -axis. With this scheme, we effectively measure the desired operator by measuring σ_z . Another state-rotation with negated amplitude (see Fig. 3.1) after the measurement undoes the first rotation.

The measurement AF is a joint weak strong measurement. The weak measurement axis is θ_A radians away from the $+Z$ -axis, and the strong measurement axis is θ_F radians away from the $+Z$ -axis (see Fig. 3.2). Our experiment only measures the σ_z component of the qubit (see Sect. 1.3.1). We can measure a different operator by first rotating the state so that the operator’s measurement axis aligns with the Z -axis. Our σ_z measurement then effectively measures the desired operator. For the weak measurement, after which other operations will be performed, we rotate the state by the negative angle, to reset the orientation (see Fig. 3.1). The joint AF measurement procedure results in a tuple of outcomes, (j, f) . The relative frequency of each tuple samples the two-dimensional joint probability distribution of AF , $p_{j,f}$.

The outcome f , being the measurement result of a Pauli operator, can equal ± 1 . The outcome j , on the other hand, is the result of a cavity state measurement. Because the cavity’s quadrature values are continuous variables (see Sect. 1.2.1), j is a continuous variable. However, in practice, we discretize the continuous outcome into 52 bins. Of these,

approximately half typically receive counts. This choice contributes a baseline amount of $\log_2(26) \simeq 4$ bits of entropy and also raises the bound.

Entropies of Strong Measurements

Consider the entropy of the first measurement, $H(\mathcal{I})_\rho$, shown as the black trace in Figure 3.3. Different initial states result in different amounts of uncertainty for the σ_z measurement. When $\theta_\rho = 0$, the initial state is $|0\rangle$ —an eigenstate of the measurement operator. Measurement outcomes thus result in one outcome with near-unity probability. (In practice, measurement infidelity reduces the probability from 100%.) The entropy of this probability distribution is nearly zero. The same argument applies when $\theta_\rho = \pi$. At the other extreme, when $\theta_\rho = \pi/2$, the initial state $\rho = (|0\rangle\langle 0| + |1\rangle\langle 1|) / \sqrt{2}$ is an eigenstate of σ_x . Here, i outcomes of the $\mathcal{I} = \sigma_z$ are nominally equiprobable. The uncertainty of this probability distribution, quantified as entropy, is maximal, with a value of 1 bit due to the number of possible outcomes (2).

The red traces of Figure 3.3 examine the sum of entropies as a function of θ_F for a fixed initial state. Because there are now two binary outcomes—each of which can misalign with the state—the maximal entropy is now two bits. The state can introduce additional uncertainty with respect to both of these measurements.

The changes in entropy for different state preparations exemplify preparation uncertainty. A given state can be represented in any (complete) basis. However, there is one particular basis in which the state’s description is most efficiently represented—the state’s eigenbasis. Efficiently represented information has minimal entropy. An operator which shares the state’s eigenbasis will have measurements with minimal representation uncertainty.

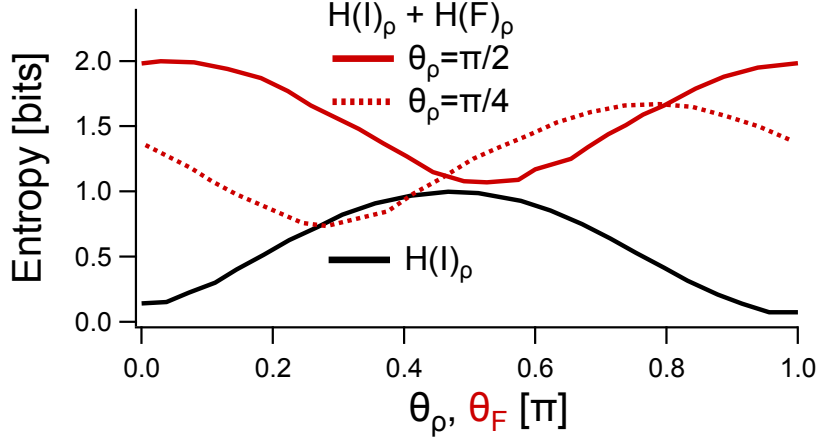


Figure 3.3: In black, the entropy of projective \mathcal{I} measurements as a function of θ_ρ displays preparation uncertainty. This entropy (for fixed ρ) adds to the entropy of the other projective measurement F , in red, for two different initial states. The near-equality between the solid curves at $\pi/2$ demonstrates the uncertainty trade-off between the two measurement operators. Finite readout fidelity (98%) is reflected in 0.14 lower bounds in each entropy.

Because the uncertainty relations we consider have two measurement operators, there are two sources of preparation uncertainty—one for each measurement. Consider an initial state prepared with $\theta_\rho = \pi/2$ and measured with $\mathcal{I} = \sigma_z$ or with $F = \sigma_z$ (solid red line in Fig. 3.3 at $\theta_F = 0$). This choice of measurements leads to two bits of uncertainty because the state’s eigenbasis is mutually unbiased with respect to both measurements. The uncertainty improves when θ_F becomes $\pi/2$, because now the F measurement shares the state’s eigenbasis.

Compare to the case of a $\theta_\rho = \pi/4$ preparation (dashed red line in Fig. 3.3). As a function of θ_F , the sum of entropies has a minimum at $\theta_F = \pi/4$, unsurprisingly because F and ρ share an eigenbasis. However, for this preparation, the new maximum is only 1.67 bits, compared to 2.0 bits. The maximum decreases because the state’s eigenbasis better aligns with both of the operator eigenbases.

The total entropy decreases when the state’s eigenbasis aligns with either measurement operator. Because we chose to fix the configuration for \mathcal{I} , we can minimize the entropy

overall by always initializing the state in an eigenstate of \mathcal{I} , e.g. with $\theta_\rho = 0$. Initializing the state to an eigenstate of one of the operators is the most interesting case because it allows the uncertainty relation to quantify uncertainty between the operators, rather than the uncertainty between each operator and the state. With the state initialized to an eigenstate of an operator, we focus only on preparation uncertainty resulting from operator-operator disagreement (rather than state-operator disagreement).

Let us turn to this operator incompatibility, quantified by the Maassen-Uffink relation (Ineq. [3.5]). For our chosen initial state, this uncertainty relation quantifies the degree of operator-operator disagreement. The relation includes two entropies and provides a lower bound for their sum. Consider the entropies. For the Maassen-Uffink case, the operators are Pauli operators, $\mathcal{I} = \sigma_z$ and $F = \sigma_\theta$. F is a linear combination of σ_z and σ_x , as in Figure 3.2.

Each of the entropies is shown in Figure 3.4. Because of the initial state, the first entropy term is nominally zero. However, state preparation and measurement errors (especially finite-temperature qubit populations) cause \mathcal{I} measurements to result in both outcomes, with 98% and 2% probability. This probability distribution has 0.14 bits of entropy, as the blue line in Figure 3.4 shows.

The second entropy, shown in red in Figure 3.4 shows how entropy depends on the measurement axis, θ_F . When θ_F increases from 0 to $\pi/2$, the two operators become less compatible, and entropy increases.

The dependence illustrates the second type of uncertainty relations owing to operator-operator disagreement called preparation uncertainty. That is, quantum mechanics disallows preparation of a state which minimizes uncertainty of both σ_x and σ_z . Preparing a definite eigenstate of one operator results in a completely mixed state of the other.

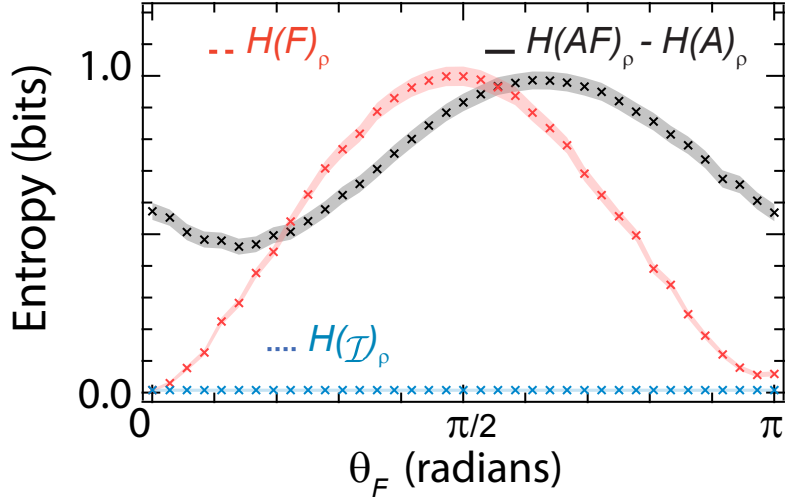


Figure 3.4: Three entropies as a function of the F measurement orientation. The blue and red curves display the entropy of \mathcal{I} or F measurements, respectively, without any weak measurement. The black curve represents the entropy of the joint AF measurement with the baseline entropy due to the many-outcome A subtracted off. Here, the weak measurement axis is set to $\theta_A = \pi/4$. Error bands indicate the propagated uncertainty due to finite sampling.

Entropies of Weak Measurements

To consider the entropy of the weak measurement, we first describe the weak measurement outcome. The outcome results from probing the state of the cavity. We correlate the cavity signal by scaling it so that when the qubit initialized to the ground or excited states, the average outcome is $+1$ or -1 , respectively. We scale the weak measurement outcomes such that an initial ground or excited state results in an average outcome of $+1$ or -1 , respectively. With the measurement strength chosen to be weak enough to satisfy the Taylor approximation in the bound (see Eqn. [3.20]), the distribution of weak measurements has a standard deviation of 5.5. We discretize the distribution of j outcomes into 52 bins.

First, let us examine the case of a weak measurement fixed to an axis $\theta_A = \pi/4$, while varying θ_F as above. To facilitate comparison to the Maassen-Uffink relation, we subtract off the entropy at $\theta_F = 0$. This point amounts to a normalization. This measurement entails

preparing the ground state, then immediately measuring σ_z weakly before strongly measuring σ_z again. The outcomes are as certain as possible with a weak measurement. However, there is uncertainty because weak measurements only provide partial state information. The entropy of the joint WF measurement thus has a minimal but nonzero value of 4.53 bits at $\theta_F = \theta_W = 0$. We subtract this normalization value off of the relation in Figure 3.4.

Thus normalized, the value $H_\rho(AF) - H_\rho(A_{\sigma_z}\sigma_z)$ compares directly to $H_\rho(F)$ and $H_\rho(\mathcal{I})$. With $\theta_W = \pi/4$, Figure 3.4 characterizes $H_\rho(AF)$ as a function of θ_F . Here, the minimal value is nonzero because the state is misaligned with the weak measurement axis. The maximum value is one bit, corresponding to the entropy added by the strong measurement—just as was the case without the weak measurement. Despite a σ_z -eigenstate preparation, the maximum does not occur at $\theta_F = \pi/2$, when $F = \sigma_x$. The weak measurement has shifted the eigenbasis which is mutually unbiased to σ_z .

From another perspective, with a preceding weak measurement, σ_x no longer maximally disagrees with σ_z , despite the two operators' failure to commute. We now explore the amelioration of σ_z and σ_x by considering $H_\rho(AF)$ as a function of θ_A with fixed $\theta_F = \pi/2$ in Figure 3.5.

As before, the entropy at $\theta_A = 0$ serves as a base case. The value results from preparing $+z$, weakly measuring σ_z then measuring $F = \sigma_x$. Weakly measuring an eigenstate does not change the state, so the F outcomes are unaffected. The entropy is thus the combination of uncertainty from unbiased F outcomes and the multiplicity of A outcomes.

Remarkably, the entropy resulting from a weak measurement halfway between the two strong measurements ($\theta_A = \pi/4$) is lower than the unbiased value. The decrease is due to the measurement-disturbance component of uncertainty relations. Weak measurements cause slight backaction on the state. The state partially collapses towards one of the eigenstates

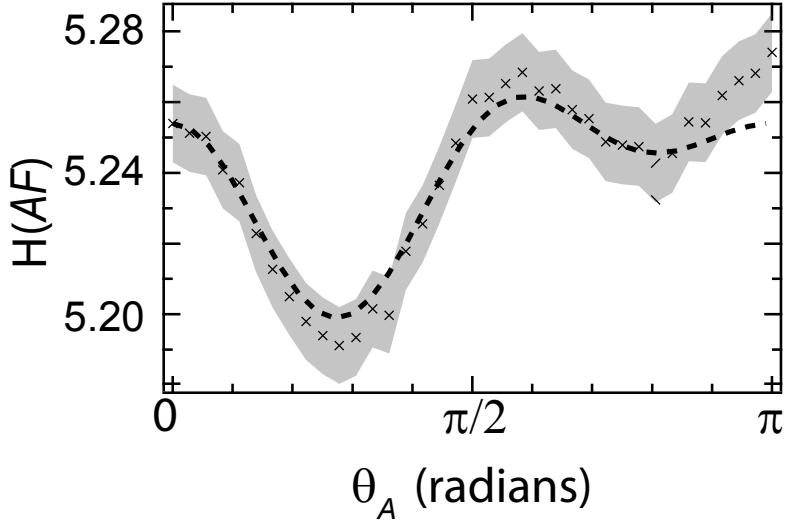


Figure 3.5: Entropy of the joint AF measurement as a function of θ_A with the strong-measurement component fixed at σ_x . The prepared state is the $|0\rangle$ eigenstate of σ_z . The dashed line indicates the prediction of a modified theory which accounts for measurement induced dephasing as well as T_1 decay. Dephasing enhances the dip at $\pi/4$ and T_1 decay raises the entropy with higher θ_A .

of the measurement operator. The state dephases, and off-diagonal components (in the measurement basis) decay.

When $\theta_A = \pi/2$, the dephasing is maximal because the state is fully orthogonal to the measurement axis. However, as Figure 3.5 shows, the resulting entropy is not minimal. This is because the dephasing does not significantly change the σ_x component of the state. There is no entropic advantage to “pre-measuring” the state.

However, when $\theta_A = \pi/4$, the entropy is minimal. Although this orientation does not maximize dephasing, the orientation does optimally shift the state towards σ_x eigenstates. This appears to contradict the results of a direct calculation of $H_\rho(AF)$ which predicts that $\theta_A = \pi/4$ should be a *maximum* in the entropy. The direct calculation results in a subtle shift in the state. However, when we estimate the probability by collecting an ensemble of measurements, inefficient detection plagues the distribution. The ensemble-level dephasing

overwhelms the subtle changes at the single trajectory level. Thus, the dephased ensemble-level dynamics dominate the measurement bias. Note also how Figure 3.5 exhibits skew with increasing θ_A . This asymmetry about $\theta_A = \pi/2$ is due to small but pronounced T_1 decay effects.

The above results for $H(AF)_\rho$ as a function of the two joint-measurement configuration angles are a part of a larger parameter space. Figure 3.6 displays measured entropies for each angle θ_A and $\theta_F \in [0, \pi]$. See Table 3.1 for specific values. Broad features match expectations; Minima in the entropy occur when both θ_A and θ_F are either 0 or π . This configuration involves σ_z measurements (weak and strong) of a σ_z eigenstate. The outcomes are minimally uncertain because each form of entropy is minimized: (i) the representation is efficient (ii) the preparation is not incompatible and (iii) no backaction occurs in either measurement. Measurements with either component near $\theta = \pi$ tend to have slightly higher entropy due to the T_1 -induced skew explained above.

Measurement configurations with maximum entropy occur near $\theta_F = \pi/2$ when the strong-measurement component disagrees maximally with the incompatible prepared state. Many measurement orientations result in statistically similar values of entropy. Surprisingly, this region of maximum entropy does not follow the line $\theta_F = \pi/2$ for all θ_A . Instead, for each value of θ_A , the maximum entropy occurs for a slightly different θ_F . At $\theta_A = 0$, the maximum entropy occurs at $\theta_F = 0$, but at $\theta_A = \pi/4$, the maximum entropy occurs at $\theta_F = 0.66\pi$. The entropy-maximizing θ_F sweeps back and forth like a sinusoid as a function of θ_A with an amplitude of 0.11π . This result is an alternative way to describe Figure 3.5: Varying θ_A along $\theta_F = \pi/2$, the entropy decreases because the maximally disagreeing F operator is no longer σ_x . Although the absolute maximum occurs at $(\theta_A, \theta_F) = (0.69\pi, 0.42\pi)$, this appears to be a statistical fluctuation on top of T_1 -induced skew.

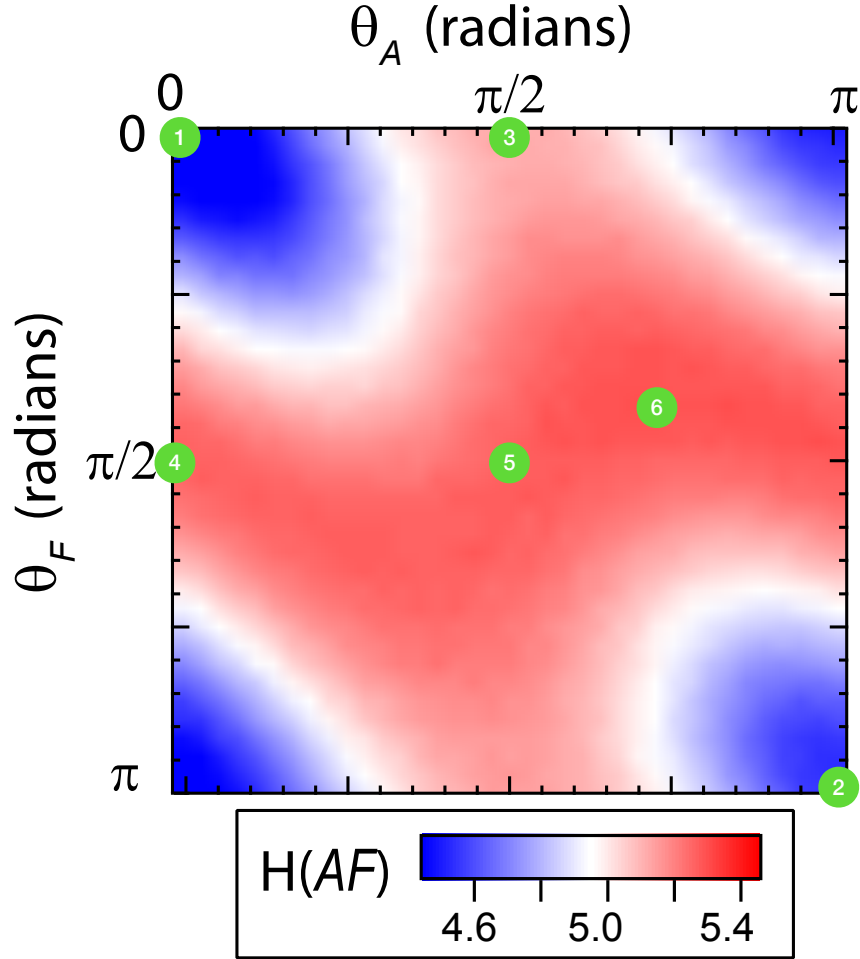


Figure 3.6: The entropy of the AF measurement outcomes as a function of the configuration angles for each measurement component. See Figure 3.2 for definitions of the measurement angles. The minima in entropy, colored blue, appear when both measurement axes align with the state, initialized to a σ_z eigenstate ($\theta_\rho=0$). See Table 3.1 for explicit values at marked points. Maxima in the entropy, colored red, occur when either the weak measurement A or the strong measurement F are oriented $\pi/2$ radians away from the initial state, due to these measurements being unbiased bases for the initial state. Across the parameter range, $H(\mathcal{I})_\rho$ contributes 0.01 bits.

Index	θ_A	θ_F	$H(AF)_\rho$ [bits]	Notes
1	0	0	4.30	Absolute minimum
2	π	π	4.56	Theoretical minimum, biased by T1 noise
3	$\pi/2$	0	5.11	Disagreement with A alone
4	0	$\pi/2$	5.25	Disagreement with F alone
5	$\pi/2$	$\pi/2$	5.26	Disagreement with both AF
6	0.69π	0.42π	5.29	Absolute maximum

Table 3.1: Explicit values for the entropy $H(AF)_\rho$ (Fig. 3.6) for various points of interest in (θ_A, θ_F) parameter space. Each value has a typical uncertainty of 0.03 bits due to finite sampling statistics.

3.3.2 Bound of the Entropic Uncertainty Relation

We have so far focused on the uncertainty component of our primary entropic uncertainty relation. Let us now turn to the bound. cQED allows nearly independent measurements of each component of the bound:

$$\min_{i,j,f} \left\{ -\log_2 \{p_j p_{f|i}\} - \frac{2}{\ln 2} \Re(g_j A_{wv}) \right\} \quad (3.23)$$

Let us discuss each of the four non-constant components in turn.

Measuring Conditional Probabilities

We will start with the conditional probability $p_{f|i}$ of obtaining outcome f given a preparation $|i\rangle$. The measurement procedure consists of preparing either $|0\rangle$ or $|1\rangle$ (eigenstates of \mathcal{I}) and measuring F (with the pre-rotation discussion in Section 3.3). Thus, the conditional probability depends only on the final measurement angle, θ_F . The sequence is similar to Rabi oscillations [31], modified by the initial π pulse. The results are shown in Figure 3.7(a).

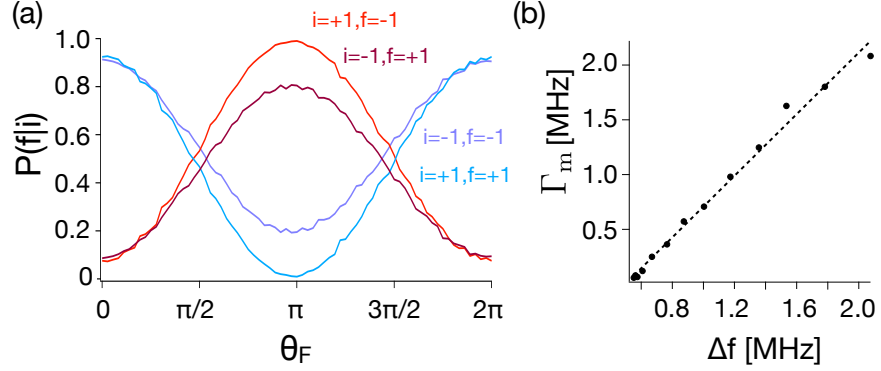


Figure 3.7: Components of RHS (a) The conditional probability of measuring outcome f from strongly measuring θ_F after preparing an i eigenstate. Each choice of i and f is indicated. Red hues correspond to $i \neq f$ and blue hues correspond to $i = f$. Darker shades correspond to the case when i is prepared as an excited state, leading to added T_1 decay. (b) Calibrating the measurement strength. By populating the cavity with \bar{n} photons, we shift the qubit frequency by a fixed amount Δf , causing dephasing Γ . The slope is $\frac{4\chi}{\kappa}$, providing the measurement strength.

Measuring p_j and g_j

Now consider the components associated with the Taylor expansion of the weak measurement Kraus operator, K_j . The Taylor expansion produced Equation [3.20] and provided expressions for p_j and g_j which depend only on the measurement strength.

To calibrate the measurement strength, we populate the cavity with photons and measure the qubit's T_2^* decay time with a Ramsey sequence [31]. The measurement provides the ensemble dephasing rate, $\Gamma_m = 8\chi^2\bar{n}/\kappa$ and the ac Stark shift, $\Delta\omega_q = 2\chi\bar{n}$. $\kappa/(2\pi) = 4.5$ MHz is the cavity linewidth measured with low power transmission via a vector network analyzer. From these values, we infer the dispersive coupling rate, $\chi/(2\pi) = -1.5$ MHz, and the mean intracavity photon number during the weak measurement, $\bar{n} = 0.5$. We integrate the weak signal for $\delta t = 250$ ns, setting $\delta t/\tau = 0.375$. From this we calculate $\sqrt{p_j} = \left(\frac{\delta t}{2\pi\tau}\right)^{1/4} \exp\left(-\frac{\delta t}{4\tau}[j^2 + 1]\right)$ and $g_j = \frac{\delta t}{2\tau}j$ for each value of j in the span sampled during the LHS measurement. See Figure 3.7(b).

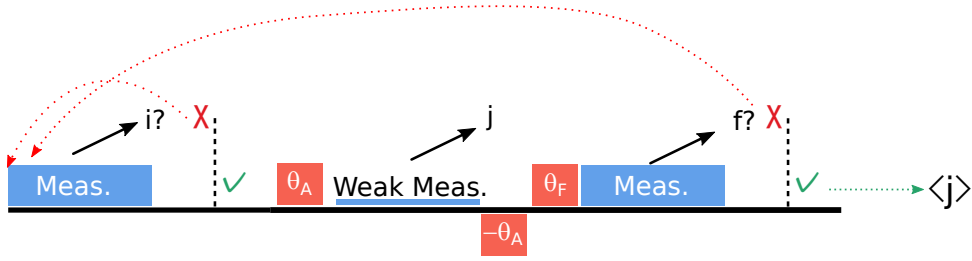


Figure 3.8: To measure weak value $A_{\text{wv}}^{i,f}$, the state $|i\rangle$ is prepared and measured. If the undesired outcome results, the run is discarded and begins again. A weak A measurement results in outcome j . Then F is strongly measured to obtain outcome f . If f is not the desired outcome the run is discarded and begins again. If the desired outcome results, the outcome j is included in a final average which estimates the weak value.

Measuring weak values

The weak value is a pre- and post-selected (conditional) expectation value [20, 164]:

$$A_{\text{wv}}^{i,f} = \frac{\langle f|A|i\rangle}{\langle f|i\rangle}, \quad (3.24)$$

where we have explicitly denoted the \mathcal{I} and F outcomes, i and f . We experimentally probe the weak value through the protocol shown in Figure 3.8. The protocol is similar to measuring the LHS of the entropic uncertainty relation but differs because of post-selection.

Each choice of i and f , corresponds to a different weak value. As an example, consider the process for measuring the weak value for $i = -1$ and $f = +1$. First, two counters for the numbers of total and successful trials initialize to zero. After heralding the ground state, a π -pulse prepares the pre-selected \mathcal{I} eigenstate, $|1\rangle$. Fast rotations prepare the state for an A measurement which results in outcome j . A final set of rotations prepare the state for the strong F measurement. The number of total trials increments. For the case of measuring $A_{\text{wv}}^{-1,+1}$, if the F measurement results in $f = -1$, the outcome is discarded and the sequence repeats. If the F measurement results in $f = +1$, then the success counter increments and

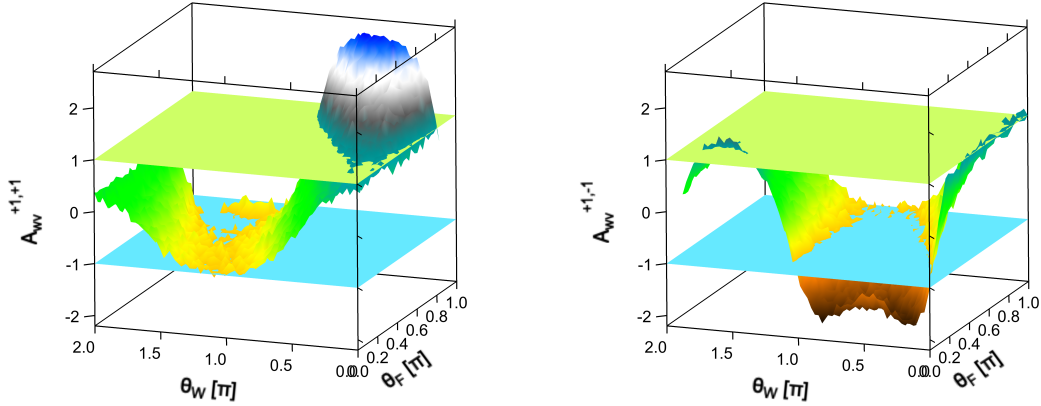


Figure 3.9: The weak value, $A_{\text{wv}}^{i,f}$, for two choices of i and f across a span of AF compositions. Outside of $\theta_F \in \{\pi/6, 5\pi/6\}$, the sampling success probability for one of these weak values becomes prohibitively low. The weak value is expected to show similar behavior for $\theta_F > \pi$. Pastel blue and green planes indicate the maximum expectation value for Pauli operators. Weak values beyond these are anomalous.

the value of j is appended to a list of successful outcomes. After a sufficient number of trials, the average value of successful j outcomes is divided by the fraction of successful trials, producing the weak value.

Weak value averaging depends on successful measurement outcomes. The success probability depends on the overlap between $|f\rangle$ and $|i\rangle$ and is equal to $\frac{1}{2}(1 + \cos\theta_F)$. Dephasing due to the A measurement can slightly improve this probability, but the θ_F dependence dominates. When θ_F takes on values outside the range $[\pi/6, 5\pi/6]$, the post-selection success probability becomes too small to measure accurately in a reasonable amount of time. Fortunately, this range contains the point $\theta_F = \pi/2$, which is a primary point of interest for the uncertainty relation. In order to expedite measurements, we only measure $A_{\text{wv}}^{+1,+1}$ and $A_{\text{wv}}^{+1,-1}$, using the fact that $A_{\text{wv}}^{+1,+1} = -A_{\text{wv}}^{-1,-1}$. Figure 3.9 displays the results of these two measurements.

Many of our weak values are anomalous. The maximally anomalous weak value is 2.7, well beyond 1—the maximal value for an expectation value of a Pauli operator. More anomalous weak values do not play a significant role in the uncertainty relation’s bound because they violate the Taylor approximation assumed in the bound (see Equations [3.21]).

Some of our measured weak values display apparent suppression of anomalous weak values (see especially $A_{\text{wv}}^{+1,-1}$ in Figure 3.9). We attribute this to T_1 effects. T_1 jumps are rare because the measurement time (250 ns) is much shorter than the T_1 time (50 μs). However, anomalous weak values require sampling rare events, namely preparation of one eigenstate and measurement of a nearly orthogonal eigenstate. While the probability of such a nearly-orthogonal projection is low, T_1 decay increases the probability.

3.3.3 Combing Elements of the RHS

We now have each element to construct the argument for the minimization over i, j , and f in the RHS of Inequality [3.22]. Figure 3.10 shows the result of the minimization for each configuration of AF . This bound is always lower than the measured entropy, as expected.

Consider how well the bound does in predicting the entropy. The bound’s tightness, the LHS – RHS, is maximal throughout a set of orientations near $\theta_F = \pi/2$. Here, the tightness is 2.45 ± 0.05 bits. Theoretically, the tightness is 0.7 bits, but inefficient detection ($\eta = 10\%$) raises the entropy sum’s by 1.66 bits.

The bound follows a similar qualitative shape as the LHS. The maximum of the bound is near $\theta_F = \pi/2$, indicating nearly maximal disagreement between \mathcal{I} and σ_x . However, the maximum shifts sinusoidally with θ_A . For example, when $\theta_A = \pi/4$, the maximally disagreeing AF measurement has $\theta_F = 0.53\pi$, when the measurement strength is $\delta t/\tau = 0.17$.

When $\theta_F = \pi/2$, setting θ_A to $\pi/4$ reconciles disagreeing operators, σ_z and σ_x . Phrased alternatively, for fixed $\theta_F = \pi/2$, the bound decreases as θ_A increases from 0 to $\pi/4$.

The weak value decreases the bound. The second term of the bound enters with a negative sign. The signs of A_{wv} and g_j correlate so that the sign of their product is positive. Hence, the weak value term decreases the bound, reconciling incompatible observables.

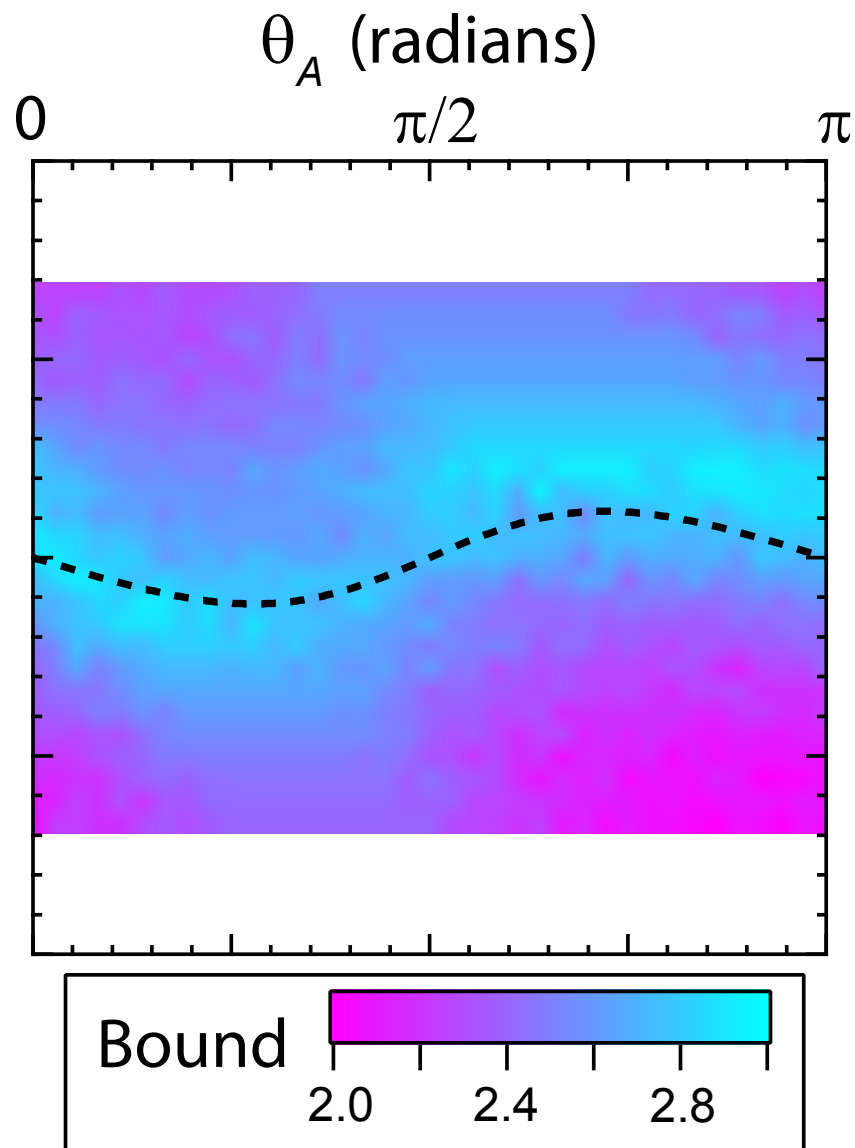


Figure 3.10: The bound for the sum of entropies for our two POVMs. The theoretical maximum of the bound is indicated with the black dashed curve.

Chapter 4

Time-Reversed Feedback

4.1 Introduction

In this chapter, we investigate the origin of irreversible dynamics from reversible processes. This is Loschmidt's paradox. We study single quantum trajectories and compare forward and backward path probabilities to infer a statistical arrow of time quantified by an entropic measure. Moreover, we implement post-selected feedback protocols wherein the extraction and subsequent use of information appear to set a definite direction for the arrow of time. Though causal-order feedback does not affect entropy production, a reversed causal order feedback protocol reverses the flow of entropy, annihilating rather than creating entropy, revealing the essential role of causality in the direction of the arrow of time.

Standard dynamics of quantum systems, as governed by Schrödinger's equation, are time-reversal invariant. Taking $t \rightarrow -t$ and taking the complex conjugate leaves the Schrödinger

equation unaffected:

$$\begin{aligned}
i\hbar \frac{\partial}{\partial t} \psi(t) &= H\psi(t), \\
\rightarrow (-)i\hbar \frac{\partial}{\partial(-t)} \psi(t) &= H\psi(t), \\
\rightarrow i\hbar \frac{\partial}{\partial t} \psi(t) &= H\psi(t).
\end{aligned} \tag{4.1}$$

While under such dynamics the von Neumann entropy is constant, many quantum mechanical systems allow for the gain or loss of information corresponding to changes in the von Neumann entropy. For example, measurement is a process that can change a system's entropy. When a system starts in a mixed state (maximal entropy), measurement projects the system onto a pure eigenstate, resulting in zero entropy.

On the other hand, consider measuring σ_x of the state $\rho = |0\rangle\langle 0|$. The state is initially pure, with no entropy. But upon projection onto a σ_x eigenvector, the state's information (Shannon) entropy in the original basis has increased.

Each of these phenomena displays entropy production or annihilation. However, systems described by unitary (i.e. norm-preserving) dynamics can have no such entropy change. This is the quantum analog of Loschmidt's paradox wherein phase-space volume conservation (as guaranteed by Liouville's theorem) seemingly cannot produce phase space enlarging processes, as demanded by the laws of thermodynamics.

Changes in entropy arise when subsystems are traced over, yet due to their presence in an inaccessible environment, or as a measurement apparatus [165]. Such an *open* quantum system allows for entropy-producing evolution [166]. Thus, open quantum systems can have stochastic evolution which obeys more nuanced laws of entropy production [167, 168, 169, 170]. Rather than satisfying Clausius' maxim that thermodynamic entropy always increases, statistical entropy of open quantum systems can fluctuate between positive and negative values.

A stochastic version of the second law of thermodynamics for classical systems resolved Loschmidt's paradox [171, 172, 173]. The law is expressed as a fluctuation theorem that describes the statistics of time-ordered and time-reversed dynamics [174, 175, 176]. Such fluctuation theorems have been successfully measured in a variety of classical systems [177, 178, 179, 180], as well as quantum systems [181, 182, 183].

4.2 Stochastic Thermodynamics

The expectation of time-irreversible dynamics, especially entropy production, is firmly grounded in thermodynamics. However, for small systems, such as particles undergoing Brownian motion, standard thermodynamics begin to break down. As thermodynamic variables describe more strongly stochastic processes, common notions like positive entropy production are challenged. These quantities fluctuate, and can occasionally take on negative values.

4.2.1 Classical Fluctuation Theorems

We begin with a classical treatment of stochastic thermodynamics, following the development of Ref. [184]. Consider a system and a reservoir at temperature T . We wish to describe the dynamics of the system while interacting with the reservoir. The state is indexed by m , and the probability of occupying state m follows one of the standard ensembles. We suppose that the master equation is Markovian and has the following form:

$$\dot{p}_m = \sum_{m'} H_{m',m} p'_m \tag{4.2}$$

where $H_{m,m'}$ is the transition matrix element from state m' to m . In the case of equilibrium with the bath, the transition matrix obeys detailed balance:

$$H_{m,m'} p_{m'}^{\text{eq}} = H_{m',m} p_m^{\text{eq}}, \quad (4.3)$$

where p_m^{eq} is the equilibrium distribution for the particular ensemble.

We focus on the stochastic dynamics of a single trajectory, emphasizing its thermodynamics. The interaction with the reservoir induces jumps in the trajectory (which we will interpret as heat). The resulting discontinuities break up the trajectory into sub-intervals of smooth, unitary evolution (during which work is performed). We specify the interval after jump j with a single index $m_j(t)$, which depends on time, $t \in [t_j, t_{j+1})$.

Because energy is a state function, the total change in the energy across the trajectory is unaffected by the discontinuities. The total change in energy only depends on the final and initial states. We use this fact to define the first law of thermodynamics for the stochastic trajectory. The energy is composed of two path-dependent quantities, which we call heat, \mathcal{Q} and work, \mathcal{W} :

$$\Delta E = \mathcal{Q} + \mathcal{W}. \quad (4.4)$$

Following common approaches in quantum thermodynamics [citeNaghiloo2020](#), we associate work with the smooth evolution (due to energy level shifts) and heat with the jump evolution (due to state changes). Within the smooth interval, the work becomes a state variable of the trajectory (a microstate) and can be calculated as the energy difference at the interval's endpoints.

$$\mathcal{W} = [E_{m_0(t_1)} - E_{m_0(t_0)}] + \dots + [E_{m_N(t_f)} - E_{m_N(t_N)}]. \quad (4.5)$$

The heat describes the energy related to jumps:

$$\mathcal{Q} = \sum_j [E_{m_j(t_j)} - E_{m_{j-1}(t_j)}]. \quad (4.6)$$

Entropy is often thought of as an ensemble property. However, with the ability to calculate the probability of a single trajectory, we can define a microstate entropy via the surprisal, similarly to Section 3.1.2. This definition of entropy retains its state-variable characteristic [185, 186], and so it only depends on the initial and final states:

$$\Delta\mathcal{S} = -k (\ln P[m_f] - \ln P[m_i]), \quad (4.7)$$

where k is Boltzmann's constant.

We decompose this entropy into two components:

$$\Delta\mathcal{S} = \Delta\mathcal{S}_r + \Delta\mathcal{S}_i. \quad (4.8)$$

The first component, $\Delta\mathcal{S}_r$, describes reversible entropy flow via heat exchange with the reservoir. It comes from the Clausius definition:

$$\Delta\mathcal{S}_r = \frac{\mathcal{Q}}{T} \quad (4.9)$$

The second component, $\Delta\mathcal{S}_i$ describes irreversible entropy production and will relate to forward and backward path probabilities.

To see this, consider the probability of the forward path, P_F . The total probability is given by the product of each independent step. The probability of the path to (i) start at the initial

state, (ii) evolve for the interval, (iii) jump, (iv) evolve, (v) jump, etc. is:

$$P_F = P[m_0] \times P[m_0(t_0) \rightarrow m_0(t_1)] \times P[m_0(t_1) \rightarrow m_1(t_1)] \times \dots \times P[m_f]. \quad (4.10)$$

The actual calculation would be incredibly tedious, but we can greatly simplify it by considering groups of terms in turn. First, the jump probabilities are simply given by the specified H_{m_{j+1}, m_j} of the master equation. Second, consider the no-jump probabilities for a single interval. The probability of each smooth interval $[t_j, t_{j+1}]$ can be calculated as the probability of having no jumps, for every infinitesimal interval $dt \in [t_{j-1}, t_j]$, $1 - H_{m_{j+dt}, m_j}$. Integrating the interval results in a path integral [184]. Fortunately, we do not need to perform this calculation because this group of no-jump factors cancels in the forward and reverse path probabilities [187]. The final group contains the boundary terms, which are given by the ensemble distribution.

Turning to the backward path probability, P_B , we follow the same prescription. The jumps now occur with probability $H_{m_j, m_{j+1}}$ (indices inverted). The smooth intervals have the same probability as in the reversed case. This treatment produces an expression analogous to Equation [4.10] for P_B .

We can then calculate the log-ratio of the forward-to-backward path probabilities:

$$\ln \frac{P_F}{P_B} = \ln P[m_1] + \sum_j \ln \frac{H_{m_j, m_{j+1}}}{H_{m_{j+1}, m_j}} - \ln P[m_N]. \quad (4.11)$$

We now applied detailed balance to finish the proof. From Equation [4.3], we have:

$$\sum_j \ln \frac{H_{m_j, m_{j+1}}}{H_{m_{j+1}, m_j}} = \sum_j \ln \frac{P_{m_j}^{\text{eq}}}{P_{m_{j+1}}^{\text{eq}}} = -\beta Q = -\frac{\Delta \mathcal{S}_r}{k}. \quad (4.12)$$

Substituting expressions for the total and irreversible entropies (Eqns. [4.7] and [4.12]) into Equation [4.11], we can see:

$$k \ln \frac{P_F}{P_B} = \Delta\mathcal{S} - \Delta\mathcal{S}_r. \quad (4.13)$$

Thus, we identify the irreversible entropy production in terms for forward and backward path probabilities:

$$\boxed{\ln \frac{P_F}{P_B} = \frac{\Delta\mathcal{S}_i}{k}} \quad (4.14)$$

From this derivation, especially at Equation [4.11], we can see why $\Delta\mathcal{S}_r$ and $\Delta\mathcal{S}_i$ have been called boundary and bulk terms, respectively [185, 188, 186]. The reversible entropy flow relates to the final and initial state of the trajectory, while the irreversible entropy production relates to the intermediate evolution.

More explicit statistical mechanical calculations based on reversing phase-space trajectories provide the same result [189]. Moreover, it can be proved based solely on results of measure theory [190]. From this expression for the entropy production in terms of forward and reversed path probabilities, we can derive several additional stochastic thermodynamic relations.

Detailed Fluctuation Theorem

The detailed fluctuation theorem describes the probability that the entropy production takes on some specific value, $P(\Delta\mathcal{S}_i = \mathcal{P})$. The theorem takes the form of a ratio between the probabilities of $\pm\mathcal{P}$. We use the Dirac delta functional¹² to select trajectories that create

¹²This object is called a functional because unlike a function which maps a number to a number, this object maps a function to a number (namely the function's value at zero).

entropy \mathcal{P} :

$$\begin{aligned}
P(\Delta\mathcal{S}_i = \mathcal{P}) &= \sum_{\text{traj.}} P_F \delta \left[\mathcal{P} - k \ln \frac{P_F}{P_B} \right] \\
&= e^{\mathcal{P}} \sum_{\text{traj.}} P_B \delta \left[\mathcal{P} - k \ln \frac{P_F}{P_B} \right] \\
&= e^{\mathcal{P}} \sum_{\text{traj.}} P_B \delta \left[-\mathcal{P} - k \ln \frac{P_B}{P_F} \right] \\
&= e^{\mathcal{P}} P(\Delta\mathcal{S}_i = -\mathcal{P})
\end{aligned} \tag{4.15}$$

Thus, the ratio of probabilities for trajectories producing an irreversible entropy of $\pm\mathcal{P}$ is equal to $e^{\mathcal{P}}$.

This expression represents one of a variety of generalized second laws of thermodynamics [191], applied to stochastic systems. It is an exact equality that characterizes much more than the narrow (and sometimes false) statement about the monotonic increase of entropy. It not only allows for negative entropy fluctuations but requires at least small negative entropy fluctuations to balance the ratio. These negative fluctuations can be thought of as a state update procedure becoming less certain about the actual state [192]. The apparent absence of observed entropy annihilation arises from the exponential suppression of backward trajectories. Because of its role in the time-reversibility of dynamics, such adherence to fluctuation theorems is often an important characteristic of arrow-of-time statistics [172, 173].

Integral Fluctuation Theorem

We also obtain the integral fluctuation theorem. This theorem returns us to the ensemble level of traditional thermodynamics. We calculate an average over an ensemble of trajectories.

$$\langle e^{-\Delta\mathcal{S}_i/k} \rangle = \left\langle e^{\ln \frac{P_B}{P_F}} \right\rangle = \left\langle \frac{P_B}{P_F} \right\rangle = \sum_{\text{traj.}} P_F \frac{P_B}{P_F} = 1. \tag{4.16}$$

Jarzynski's Equality and the Second Law

In the special case that the trajectory begins and ends in equilibrium states, we can also derive Jarzynski's equality. In this case, the entropy production obeys $T\Delta\mathcal{S}_i = \mathcal{W} - \Delta F^{\text{eq}}$. So the integral fluctuation theorem becomes:

$$\begin{aligned}\langle e^{-\Delta\mathcal{S}_i/k} \rangle &= 1 \\ \langle e^{-\beta\mathcal{W} + \beta\Delta F} \rangle &= 1 \\ \langle e^{-\beta\mathcal{W}} \rangle &= e^{-\beta\Delta F}.\end{aligned}\tag{4.17}$$

This seminal equality has also been extended to include measurement and feedback [193, 194, 195].

The more familiar second law about entropy increase also follows from the integral fluctuation theorem:

$$\langle \Delta\mathcal{S}_i \rangle = \langle \ln e^{\Delta\mathcal{S}_i} \rangle \geq \ln \langle e^{\Delta\mathcal{S}_i} \rangle = \ln 1 = 0.\tag{4.18}$$

The inequality comes from an application of Jensen's inequality which applies to any convex function f : $f(\bar{x}) \leq \bar{f}(x)$, where, for the sake of clarity, averages are indicated with bars.

4.2.2 Thermodynamics of Quantum Trajectories

We have shown in Section 1.3.2 how to update a state based on the stochastic outcome of a partial measurement. Based on these trajectories, we can calculate forward and backward path probabilities, allowing for a characterization of the entropy production (and annihilation) in open quantum systems.

Reversibility is a key tenet for the calculation in Section 4.2.1. The reversibility of quantum measurement dynamics is enabled by the positivity of the POVM mapping [50]. For a measurement of non-zero strength, some backaction will be imparted on the system. Measuring outcome j changes the initial state ρ_0 to $\rho_1 \propto K_j \rho_0 K_j^\dagger$ via the Kraus operator, K_j (see Sect. 1.3.2). This update protocol is reversible since we may apply a time-reversed measurement that undoes the backaction. The operator Θ produces the reversing measurement: $\tilde{K}_j = \Theta K_j \Theta^\dagger$. The reversed measurement operator reverses a single step in the trajectory:

$$\begin{aligned}
\tilde{\rho}_0 &\propto \tilde{K}_j \tilde{\rho}_1 \tilde{K}_j^\dagger \\
&\propto K_{-j} \Theta K_j \rho_0 K_j^\dagger \Theta^\dagger K_{-j}^\dagger \\
&\propto \Theta \rho_0 \Theta^\dagger,
\end{aligned} \tag{4.19}$$

where we have used the fact that $\Theta \Theta^\dagger = 1$. We applied the so-called “passive” transformation by negating the measurement record measurements [196]. This reduces to $\tilde{\rho}_0 = \Theta \rho_0 \Theta^\dagger$, the time-reversed initial state. Thus, because we track the individual record steps, j , we can apply time-reversed measurement operators to reverse the dynamics of measurement.

With individual, reversible quantum trajectories we may proceed with calculating an irreversible entropy production. We define:

$$\mathcal{Q} \equiv \ln \frac{P_F}{P_B} \tag{4.20}$$

where P_F and P_B are the probabilities of a forward or reversed trajectory, respectively. This definition of entropy has offered insights into a statistical arrow of time [196, 183]. Similar to Equation [4.14], \mathcal{Q} obeys a detailed fluctuation theorem:

$$\frac{P(+\mathcal{Q})}{P(-\mathcal{Q})} = e^{\mathcal{Q}}. \tag{4.21}$$

The derivation of this equation is more difficult to the lack of clear definitions of state variables and measurements [197, 198].

After introducing the experiment in Section 4.3, we will describe the calculating of probabilities for these forward and reversed trajectories in Section 4.3.2 and verify the detailed fluctuation theorem in Section 4.3.3

4.3 Experiment

4.3.1 Setup

The experiment consists of a qubit coupled to a single mode of the electromagnetic field. The lowest two levels of a superconducting transmon circuit form the qubit, and a 3D aluminum cavity stores the single EM mode. A dispersive qubit-cavity interaction allows weak measurements of the qubit. The qubit's state is inferred from coherent states transmitted through the cavity. Transmitted signals receive a qubit-state-dependent frequency shift according to the dispersive Jaynes-Cummings Hamiltonian:

$$H_{\text{JC}}/\hbar = \frac{\omega_q}{2}\sigma_z + a^\dagger a(\omega_c + \chi\sigma_z). \quad (4.22)$$

The dispersive interaction, $H_{\text{int}}/\hbar = \chi a^\dagger a \sigma_z$ has been interpreted as a qubit-state-dependent frequency shift on the cavity.

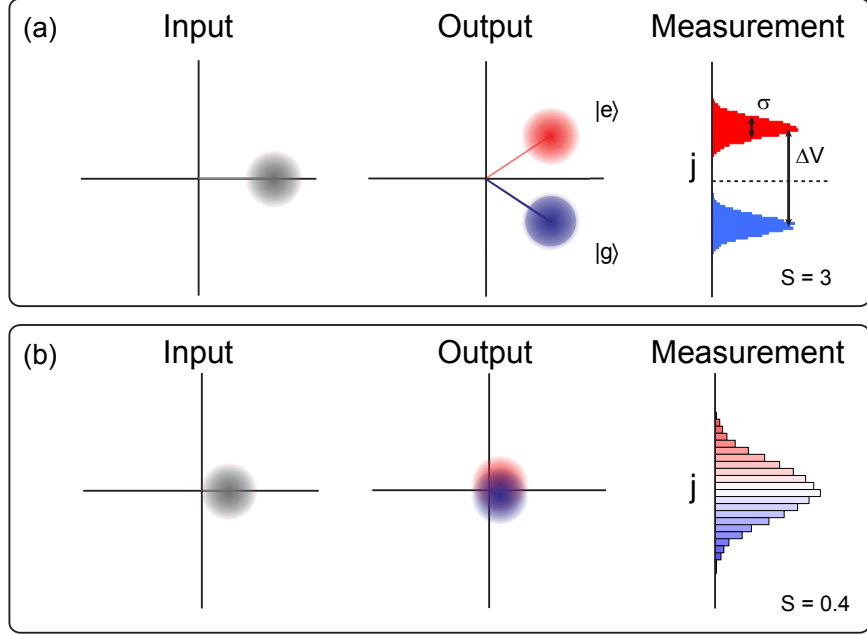


Figure 4.1: Our readout scheme allows both strong and weak measurements. **(a)** For strong measurements, a coherent tone sent into the cavity receives a qubit-state-dependent phase shift resulting in two well-separated Gaussian distributions ($S=3$). **(b)** Conversely, we implement weak measurements by decreasing the intra-cavity photon number so that the qubit states do not resolve ($S=0.4$).

Readout consists of homodyne monitoring of the field's quadrature component. The outcomes are Gaussian-distributed with a variance of σ^2 and a mean which shifts by ΔV depending on the qubit's state, as shown in Figure 4.1. The separation parameter, $S \equiv \frac{\Delta V^2}{\sigma^2}$ can be expressed in experimental parameters [5]:

$$S = \frac{8 \delta t \eta}{\tau}. \quad (4.23)$$

The measurement duration is $\delta t = 145$ ns, the characteristic measurement strength is $\frac{1}{\tau} = \frac{8\chi^2\bar{n}\eta}{\kappa} = 2\pi \times 2.54$ MHz, and the quantum efficiency is $\eta=0.31$. The measurement strength depends on the dispersive shift, $\chi/2\pi = -0.25$ MHz, the variable intra-cavity photon number, \bar{n} , and the cavity linewidth $\kappa/2\pi = 3.37$ MHz. When $S = 3$, ground- and

excited-state preparations result in significantly different homodyne voltages [Fig. 4.1(a)]. Decreasing the intra-cavity photon number, so that $S = 0.4$, implements a weak measurement. The weak measurement does not completely distinguish ground from excited qubit states [Fig. 4.1(b)], thus inducing small backaction on the state.

The Kraus operator for measurement update (see Sec. 1.3.2) is given by

$$K_j = \sqrt{\frac{\delta t}{2\pi\tau}} \exp[-(j - \sigma_z)^2 \delta t / 2\tau]. \quad (4.24)$$

From the updated state, we can directly calculate expectation values of Pauli operators, $\langle \sigma_i \rangle = \text{Tr}[\rho' \sigma_i]$. Using Bayesian update rules [199], we attain measurement-update equations for the Bloch coordinates:

$$Z_j = \tanh\left[\frac{j\delta t}{2\tau} + C\right] \quad (4.25a)$$

$$X_j = \sqrt{1 - \langle \sigma_z \rangle^2} e^{-\gamma \delta t} \quad (4.25b)$$

where γ is the dephasing rate and $C = \frac{\ln[1+Z_0]}{\ln[1-Z_0]}$ depends on the initial coordinate Z_0 .

In Figure 4.2, we show that the measurement-update equations (Eqns. [4.25]), accurately predict the measured state. For 1.3×10^6 experimental runs we collect a weak measurement record, j , followed by a tomographic projective measurement. We then bin trajectories based on j and compare the bin's average tomography value for $\langle \sigma_z \rangle$ (or $\langle \sigma_x \rangle$ or $\langle \sigma_y \rangle$) with the predicted value. Good agreement between this correlated tomography and the predictions of measurement-update equations implies that we accurately track quantum trajectories.

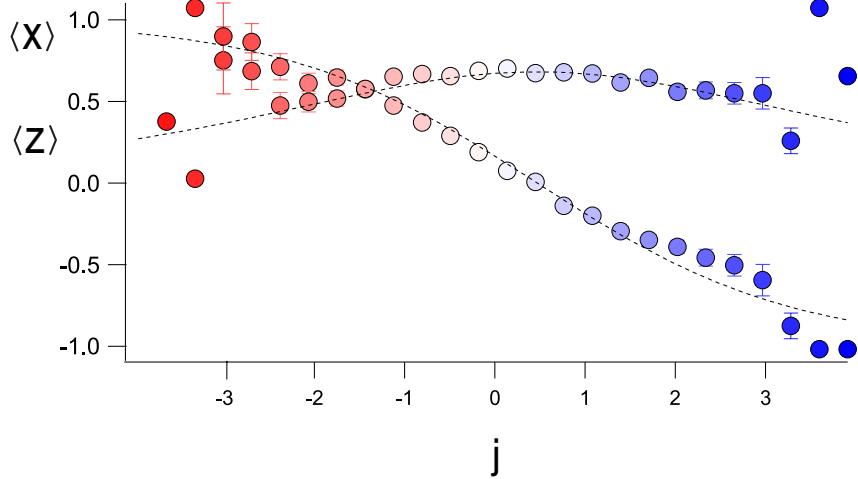


Figure 4.2: In the weak measurement regime, Bayesian state update (Eqns. 4) enables faithful state reconstruction via tomographic outcomes conditioned on average homodyne voltages. $\langle \sigma_y \rangle$ is not shown but is consistent with zero, as expected for rotations about σ_y .

4.3.2 Trajectory probabilities

We now turn to calculating the probability of individual trajectories in order to infer the likelihood of the arrow of time. Within the POVM formalism, the probability of measurement outcome j is $P(j) = \text{Tr}[K_j \rho K_j^\dagger]$. In order to directly compare forward and backward probabilities we condition on the appropriate initial condition. We reverse trajectories with an “active transformation” [196], where coordinates are inverted and the order of measurement outcomes are reversed, while the sign of the measurement outcome is fixed. We calculate the forward and backward path probabilities via conditioned Bayesian inference:

$$P_F(j|Z_0) = \frac{1 + Z_0}{2} e^{-\frac{(j - V_{\text{gnd}})^2 \delta t}{2\tau}} + \frac{1 - Z_0}{2} e^{-\frac{(j - V_{\text{ex}})^2 \delta t}{2\tau}}$$

$$P_B(j|\tilde{Z}_t) = \frac{1 + \tilde{Z}_t}{2} e^{-\frac{(j - V_{\text{gnd}})^2 \delta t}{2\tau}} + \frac{1 - \tilde{Z}_t}{2} e^{-\frac{(j - V_{\text{ex}})^2 \delta t}{2\tau}}$$

where V_{gnd} (V_{ex}) is the mean voltage measured when the qubit is prepared in the ground (excited) state and \tilde{Z}_t is the Bloch coordinate propagated to time t and then negated.

With forward and backward probabilities for individual quantum trajectories, we estimate the statistical arrow of time from the log ratio of forward and backward probabilities:

$$Q \equiv \ln \left[\frac{P_F}{P_B} \right] \quad (4.27)$$

which in general is non-zero. The preference for forward-moving trajectories ($Q > 0$) comes from the effect of measurement to project towards eigenstates. As the measurement dynamics unfold, previous measurements induce backaction towards an eigenstate, causing the relative weights of Equations 4.26 to favor continued progression towards that eigenstate. Moreover, initial conditions may bias these weights to further heighten the movement towards an eigenstate. Thus, despite the reversibility of individual measurements, we nonetheless statistically infer $\bar{Q} > 0$, i.e. trajectories tend to move forward in time.

Feedback Protocols

We now turn to our feedback protocol for state stabilization, visualized in Figure 4.3. The goal of feedback to maintain an initial state in the face of decoherence and stochastic evolution from environmental interactions. However, in order to consider the role of both causal and anti-causal feedback in the arrow of time, we implement a post-selected feedback scheme. After preparing the target state, we allow the qubit to stochastically evolve under the influence of measurement. We then apply a corrective rotation pulse, θ_{app} , about the Y -axis with a randomly chosen angle between $-\frac{\pi}{4}$ and $\frac{\pi}{4}$. In post-analysis, we select realizations wherein we chose the ideal feedback angle, $\theta_{\text{ideal}} = \tan^{-1} \left[\frac{Z_j}{X_j} \right]$, within $\frac{\pi}{20}$.

Under this feedback protocol, we then evaluate forward and backward probabilities of individual trajectories for causally-ordered feedback (COF). Critically, the backward probability, $P_B(j|\tilde{Z}_t)$, is based on the time-reversed coordinate *after* the time-reversed feedback (Fig. 4.3). At this stage, the state has undergone both feedback and its time-reversal, effectively canceling the effect of feedback [12]. Thus in the case of causal order feedback, the arrow of time ratio, seen in Figure 4.4, is the same as if we had not applied feedback. Our results for forward feedback are consistent with previous studies [196, 183].

Now consider feedback with anticausally-ordered feedback (ACOF). We utilize the same post-selected feedback protocol, but after state preparation, we proceed with a random rotation succeeded by weak measurement. Interpreted as a feedback protocol, we correct the state and then measure to see what feedback should be applied. With this protocol we observe a backward arrow of time, seen in Figure 4.4, reflecting the anticausal order of the “feedback”. In one sense, the measurements which correctly “unmeasure” the rotation are so exceedingly rare that an ensemble consisting of these trajectories must annihilate entropy. In another sense, because the arrow of time is a fundamentally causal relationship, an ACOF protocol produces a reversed arrow of time.

4.3.3 Fluctuation Theorems

We could, in principle, use this data to verify the detailed fluctuation theorem (Eqn. 4.21). However, as Figure 4.4 shows, entropy-annihilating trajectories do not occur for states prepared in $|+x\rangle\langle+x|$.

In this case, the initial state is “too unlikely” to produce entropy annihilating trajectories. Over an ensemble of many initial states, the measurement process produces entropy in accordance with the detailed fluctuation theorem. However, when the ensemble is pre-selected

to an initial state which strongly favors entropy production, the resulting distribution of \mathcal{Q} is severely skewed. Such a biased initial state deviates from an integral fluctuation theorem by a quantity called the absolute irreversibility [183].

With preliminary data of a different initial condition, $(X_0, Z_0) = (\frac{1}{\sqrt{2}}, \frac{1}{\sqrt{2}})$, we find that the entropy production and annihilation do balance according to the detailed fluctuation theorem (Figure 4.4, inset).

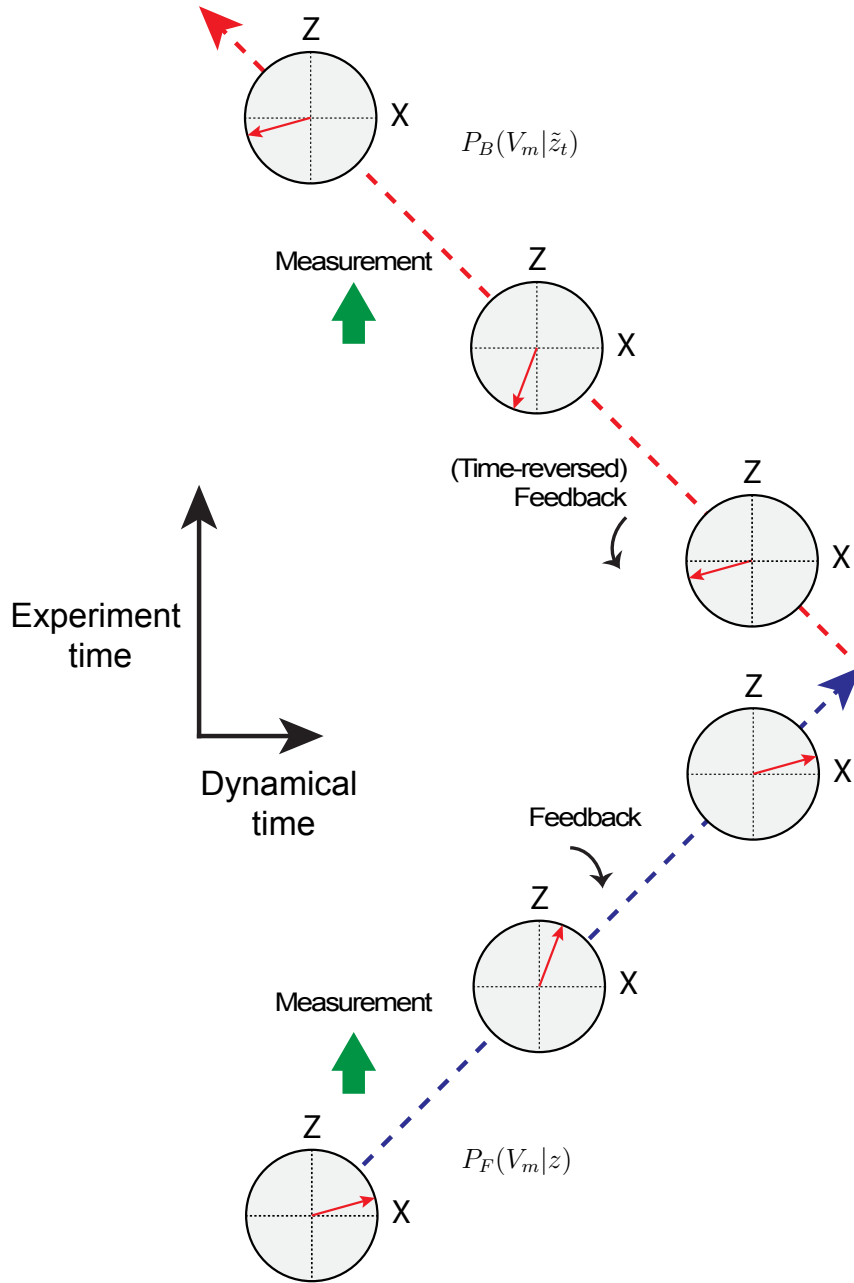


Figure 4.3: Our feedback experiments entail stabilizing an initial state and comparing forward and backward path probabilities under measurement dynamics. Experimental realizations involve (a) first preparing a state which is then perturbed by measurement-induced backaction. (b) By applying a corrective unitary feedback rotation we (c) return the qubit to its initial state. We make an equitable comparison of forward and backward probabilities by (d) flipping the dynamics (in analysis) before (e) applying the time-reversed unitary feedback (negative angle) and (f) calculating the measurement probability according to Equation 5. The backaction of the forward measurement outcome restores the system to the time-reverse of the initial state.

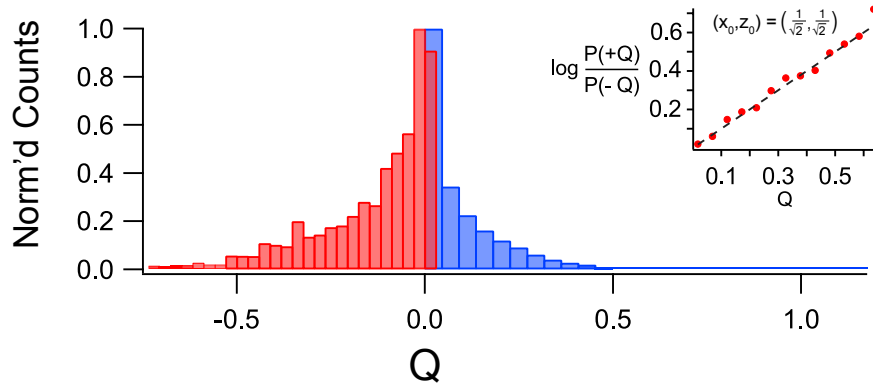


Figure 4.4: Histogram of the log ratio of forward and backward probabilities, Q (Eqn. 4.27), calculated from individual quantum trajectories. In standard COF (blue) the trajectories are essentially all entropy-producing due to the initial state, $\rho = |+x\rangle\langle +x|$. Conversely, for ACOF (red), time apparently flows backward due to the imposed anticausality. The figure inset shows validation of a fluctuation theorem for a different initial condition, as indicated.

4.4 Conclusion

In this experiment, we have investigated the nuance of entropy production (and annihilation) in quantum systems. The details of such processes require a microscopic view of individual trajectories, and an ability to evaluate probabilities of time-reversed trajectories.

The foundation of generalized second laws includes an essential connection to causality [200, 201]. We investigated the influence of COF and ACOF protocols on the fluctuation theorem. We found that feedback enforces a causal direction by allowing information gained to then be imparted into the system. We found that this preference had no effect in an already causal world. However, reversing the causality via ACOF flipped the sign of entropy production, annihilating entropy and reversing the arrow of time.

The influence of feedback on the flow of entropy, suggests that these techniques could be used to create information-based engines [202], even when causality can be reversed [203]. These would be quantum versions of Szilard's classical engine [204].

Bibliography

- [1] W. H. Zurek. Pointer basis of quantum apparatus: Into what mixture does the wave packet collapse? *Physical Review D*, 24(6):1516–1525, 1981. (Cited on page 2.)
- [2] Christine Guerlin, Julien Bernu, Samuel Deléglise, Clément Sayrin, Sébastien Gleyzes, Stefan Kuhr, Michel Brune, Jean-Michel Raimond, and Serge Haroche. Progressive field-state collapse and quantum non-demolition photon counting. *Nature*, 448(7156):889–893, aug 2007. (Cited on page 2.)
- [3] Maxime Boissonneault, J. M. Gambetta, and Alexandre Blais. Dispersive regime of circuit QED: Photon-dependent qubit dephasing and relaxation rates. *Physical Review A - Atomic, Molecular, and Optical Physics*, 79(1), 2009. (Cited on pages 2, 14, and 17.)
- [4] M. Hatridge, S. Shankar, M. Mirrahimi, F. Schackert, K. Geerlings, T. Brecht, K. M. Sliwa, B. Abdo, L. Frunzio, S. M. Girvin, R. J. Schoelkopf, and M. H. Devoret. Quantum back-action of an individual variable-strength measurement. *Science*, 339(6116):178–181, jan 2013. (Cited on pages 2, 14, and 17.)
- [5] K W Murch, S J Weber, C Macklin, and I Siddiqi. Observing single quantum trajectories of a superconducting quantum bit. *Nature*, 502(7470):211–214, 2013. (Cited on pages 2, 14, and 99.)
- [6] S. J. Weber, A. Chantasri, J. Dressel, A. N. Jordan, K. W. Murch, and I. Siddiqi. Mapping the optimal route between two quantum states. *Nature*, 511(7511):570, 2014. (Cited on pages 2 and 14.)
- [7] Shay Hacoen-Gourgy, Leigh S. Martin, Emmanuel Flurin, Vinay V. Ramasesh, K. Birgitta Whaley, and Irfan Siddiqi. Quantum dynamics of simultaneously measured non-commuting observables. *Nature*, 538(7626):491–494, oct 2016. (Cited on pages 2, 14, and 62.)
- [8] Q. Ficheux, S. Jezouin, Z. Leghtas, and B. Huard. Dynamics of a qubit while simultaneously monitoring its relaxation and dephasing. *Nature Communications*, 9(1):1926, dec 2018. (Cited on pages 2 and 14.)

- [9] R. Vijay, D. H. Slichter, and I. Siddiqi. Observation of quantum jumps in a superconducting artificial atom. *Physical Review Letters*, 106(11):1–4, 2011. (Cited on pages 3 and 14.)
- [10] U Vool, S Shankar, S O Mundhada, N Ofek, A Narla, K Sliwa, E. Zalus-Geller, Y. Liu, L. Frunzio, R. J. Schoelkopf, S. M. Girvin, and M. H. Devoret. Continuous Quantum Nondemolition Measurement of the Transverse Component of a Qubit. *Physical Review Letters*, 117(13):1–6, 2016. (Cited on pages 3 and 14.)
- [11] P. Campagne-Ibarcq, P. Six, L. Bretheau, A. Sarlette, M. Mirrahimi, P. Rouchon, and B. Huard. Observing Quantum State Diffusion by Heterodyne Detection of Fluorescence. *Physical Review X*, 6(1):011002, jan 2016. (Cited on pages 3, 14, and 62.)
- [12] M. Naghiloo, N. Foroozani, D. Tan, A. Jadbabaie, and K. W. Murch. Mapping quantum state dynamics in spontaneous emission. *Nature Communications*, 7(1):11527, sep 2016. (Cited on pages 3, 14, and 62.)
- [13] Z. K. Mineev, S. O. Mundhada, S. Shankar, P. Reinhold, R. Gutiérrez-Jáuregui, R. J. Schoelkopf, M. Mirrahimi, H. J. Carmichael, and M. H. Devoret. To catch and reverse a quantum jump mid-flight. *Nature*, 570(7760):200–204, jun 2019. (Cited on pages 3, 14, and 62.)
- [14] Ashkan Balouchi and Kurt Jacobs. Coherent versus measurement-based feedback for controlling a single qubit. *Quantum Science and Technology*, 2(2):025001, jun 2017. (Cited on page 3.)
- [15] Shay Hacoheh-Gourgy and Leigh S. Martin. Continuous measurements for control of superconducting quantum circuits. 2020. (Cited on pages 3 and 58.)
- [16] P. Campagne-Ibarcq, E. Flurin, N. Roch, D. Darson, P. Morfin, M. Mirrahimi, M. H. Devoret, F. Mallet, and B. Huard. Persistent control of a superconducting qubit by stroboscopic measurement feedback. *Physical Review X*, 3(2):1–7, 2013. (Cited on page 3.)
- [17] L. Bretheau, P. Campagne-Ibarcq, E. Flurin, F. Mallet, and B. Huard. Quantum dynamics of an electromagnetic mode that cannot contain N photons. *Science*, 348(6236):776–779, 2015. (Cited on page 3.)
- [18] Christian Arenz, Daniel Burgarth, Paolo Facchi, Vittorio Giovannetti, Hiromichi Nakazato, Saverio Pascazio, and Kazuya Yuasa. Universal Control Induced by Noise. 062308:1–11, 2016. (Cited on page 3.)
- [19] Daniel Szombati, Alejandro Gomez Friero, Clemens Müller, Tyler Jones, Markus Jerger, and Arkady Fedorov. Quantum Rifling: Protecting a Qubit from Measurement Back Action. *Physical Review Letters*, 124(7):070401, feb 2020. (Cited on page 3.)

- [20] Yakir Aharonov, David Z. Albert, and Lev Vaidman. How the result of a measurement of a component of the spin of a spin- $1/2$ particle can turn out to be 100. *Physical Review Letters*, 60(14):1351–1354, apr 1988. (Cited on pages 3 and 83.)
- [21] A. J. Leggett. Comment on “How the result of a measurement of a component of the spin of a spin- $(1/2)$ particle can turn out to be 100”. *Physical Review Letters*, 62(19):2325–2325, may 1989. (Cited on pages 3 and 62.)
- [22] Yakir Aharonov, Jeeva Anandan, Sandu Popescu, and Lev Vaidman. Superpositions of time evolutions of a quantum system and a quantum time-translation machine. *Physical Review Letters*, 64(25):2965–2968, jun 1990. (Cited on pages 3 and 62.)
- [23] O. Hosten and P. Kwiat. Observation of the Spin Hall Effect of Light via Weak Measurements. *Science*, 319(5864):787–790, feb 2008. (Cited on pages 3 and 62.)
- [24] Justin Dressel, Mehul Malik, Filippo M. Miatto, Andrew N. Jordan, and Robert W. Boyd. Colloquium: Understanding quantum weak values: Basics and applications. *Reviews of Modern Physics*, 86(1):307–316, 2014. (Cited on pages 3 and 62.)
- [25] Andrew N. Jordan, Julián Martínez-Rincón, and John C. Howell. Technical advantages for weak-value amplification: When less is more. *Physical Review X*, 4(1):1–11, 2014. (Cited on pages 3 and 62.)
- [26] S. Kocsis, B. Braverman, S. Ravets, M. J. Stevens, R. P. Mirin, L Krister Shalm, and Aephraim M Steinberg. Observing the Average Trajectories of Single Photons in a Two-Slit Interferometer. *Science*, 332(6034):1170–1173, jun 2011. (Cited on page 3.)
- [27] Daniel A. Steck. *Quantum and Atom Optics*, 2007. (Cited on pages 5 and 10.)
- [28] J J Sakurai. *Modern Quantum Mechanics (Revised Edition)*. Addison Wesley, 1993. (Cited on page 6.)
- [29] Zlatko K. Mineev, Zaki Leghtas, Shantanu O. Mundhada, Lysander Christakis, Ioan M. Pop, and Michel H. Devoret. Energy-participation quantization of Josephson circuits. pages 1–39, oct 2020. (Cited on pages 6 and 54.)
- [30] Jens Koch, Terri M Yu, Jay Gambetta, A A Houck, D I Schuster, J Majer, Alexandre Blais, M H Devoret, S M Girvin, and R J Schoelkopf. Charge-insensitive qubit design derived from the Cooper pair box. *Physical Review A*, 76(4):042319, oct 2007. (Cited on pages 9, 48, and 50.)
- [31] Mahdi Naghiloo. Introduction to Experimental Quantum Measurement with Superconducting Qubits. *Thesis*, (April), 2019. (Cited on pages 11, 23, 38, 42, 81, and 82.)
- [32] Patrick Michael Harrington. *Measurement, Dissipation, and Quantum Control with Superconducting Circuits*. PhD thesis, 2020. (Cited on pages 11, 23, and 42.)

- [33] J. R. Schrieffer and P. A. Wolff. Relation between the Anderson and Kondo Hamiltonians. *Physical Review*, 149(2):491–492, 1966. (Cited on page 12.)
- [34] Robert H. Hadfield. Single-photon detectors for optical quantum information applications. *Nature Photonics*, 3(12):696–705, 2009. (Cited on page 13.)
- [35] Y. F. Chen, D. Hover, S. Sendelbach, L. Maurer, S. T. Merkel, E. J. Pritchett, F. K. Wilhelm, and R. McDermott. Microwave photon counter based on josephson junctions. *Physical Review Letters*, 107(21):1–5, 2011. (Cited on page 13.)
- [36] Bülent Demirel, Stephan Sponar, Alastair A. Abbott, Cyril Branciard, and Yuji Hasegawa. Experimental test of an entropic measurement uncertainty relation for arbitrary qubit observables. *New Journal of Physics*, 21(1):013038, jan 2019. (Cited on pages 13 and 62.)
- [37] Kip S. Thorne, Ronald W. P. Drever, Carlton M. Caves, Mark Zimmermann, and Vernon D. Sandberg. Quantum Nondemolition Measurements of Harmonic Oscillators. *Physical Review Letters*, 40(11):667–671, mar 1978. (Cited on page 14.)
- [38] Jean-Philippe Poizat, Jean-François Roch, and Philippe Grangier. Quantum non-demolition measurements in optics and quantum optical repeaters. *Fundamentals of Quantum Optics III*, pages 289–305, 2007. (Cited on page 14.)
- [39] Jay Gambetta, Alexandre Blais, D. I. Schuster, A. Wallraff, L. Frunzio, J. Majer, M. H. Devoret, S. M. Girvin, and R. J. Schoelkopf. Qubit-photon interactions in a cavity: Measurement-induced dephasing and number splitting. *Physical Review A - Atomic, Molecular, and Optical Physics*, 74(4):1–14, 2006. (Cited on page 14.)
- [40] N. Foroozani, M. Naghiloo, D. Tan, K. Mølmer, and K. W. Murch. Correlations of the Time Dependent Signal and the State of a Continuously Monitored Quantum System. *Physical Review Letters*, 116(11):110401, mar 2016. (Cited on page 14.)
- [41] P. Campagne-Ibarcq, S. Jezouin, N. Cottet, P. Six, L. Bretheau, F. Mallet, A. Sarlette, P. Rouchon, and B. Huard. Using Spontaneous Emission of a Qubit as a Resource for Feedback Control. *Physical Review Letters*, 117(6):1–6, 2016. (Cited on page 14.)
- [42] B.H. Bransden and C.J. Joachain. *Quantum Mechanics*. Prentice Hall, 2000. (Cited on pages 14 and 26.)
- [43] Michael A Nielsen and Issac L Chuang. *Quantum computation and quantum information*. Cambridge University Press, Cambridge New York, 2000. (Cited on pages 14 and 15.)
- [44] Max Born. Zur Quantenmechanik der Stoßvorgänge. *Zeitschrift für Physik*, 37(12):863–867, dec 1926. (Cited on page 15.)

- [45] Andrew N. Jordan and Alexander N. Korotkov. Uncollapsing the wavefunction by undoing quantum measurements. *Contemporary Physics*, 51(2):125–147, mar 2010. (Cited on page 15.)
- [46] Todd A. Brun. A simple model of quantum trajectories. 2001. (Cited on page 15.)
- [47] Kurt Jacobs and Howard Wiseman. An Entangled Web of Crime: Bell’s Theorem as a Short Story. (August 2004):8, 2005. (Cited on page 15.)
- [48] J Von Neumann. *Mathematische Grundlagen der Quantenmechanik*. Die Grundlehren der mathematischen Wissenschaften in Einzeldarstellungen. J. Springer, 1932. (Cited on page 16.)
- [49] Kurt Jacobs and Daniel A. Steck. A straightforward introduction to continuous quantum measurement. *Contemporary Physics*, 47(5):279–303, 2006. (Cited on pages 16 and 68.)
- [50] K Jacobs. *Quantum Measurement Theory and its Applications*. Cambridge University Press, 2014. (Cited on pages 17 and 97.)
- [51] Alexandre Blais, Ren Shou Huang, Andreas Wallraff, S. M. Girvin, and R. J. Schoelkopf. Cavity quantum electrodynamics for superconducting electrical circuits: An architecture for quantum computation. *Physical Review A - Atomic, Molecular, and Optical Physics*, 69(6):1–14, 2004. (Cited on page 17.)
- [52] John M. Martinis, K. B. Cooper, R. McDermott, Matthias Steffen, Markus Ansmann, K. D. Osborn, K. Cicak, Seongshik Oh, D. P. Pappas, R. W. Simmonds, and Clare C. Yu. Decoherence in Josephson qubits from dielectric Loss. *Physical Review Letters*, 95(21):1–4, 2005. (Cited on pages 18, 50, 51, and 57.)
- [53] M. J.A. Stoutimore, M. S. Khalil, C. J. Lobb, and K. D. Osborn. A Josephson junction defect spectrometer for measuring two-level systems. *Applied Physics Letters*, 101(6):1–4, 2012. (Cited on pages 18, 50, and 51.)
- [54] Clemens Müller, Jürgen Lisenfeld, Alexander Shnirman, and Stefano Poletto. Interacting two-level defects as sources of fluctuating high-frequency noise in superconducting circuits. *Physical Review B - Condensed Matter and Materials Physics*, 92(3), 2015. (Cited on pages 19 and 52.)
- [55] P. V. Klimov, J. Kelly, Z. Chen, M. Neeley, A. Megrant, B. Burkett, R. Barends, K. Arya, B. Chiaro, Yu Chen, A. Dunsworth, A. Fowler, B. Foxen, C. Gidney, M. Giustina, R. Graff, T. Huang, E. Jeffrey, Erik Lucero, J. Y. Mutus, O. Naaman, C. Neill, C. Quintana, P. Roushan, Daniel Sank, A. Vainsencher, J. Wenner, T. C. White, S. Boixo, R. Babbush, V. N. Smelyanskiy, H. Neven, and John M. Martinis. Fluctuations of Energy-Relaxation Times in Superconducting Qubits. *Physical Review Letters*, 121(9):90502, 2018. (Cited on pages 19, 50, and 52.)

- [56] Jonathan J. Burnett, Andreas Bengtsson, Marco Scigliuzzo, David Niepce, Marina Kudra, Per Delsing, and Jonas Bylander. Decoherence benchmarking of superconducting qubits. *npj Quantum Information*, 5(1):1–8, 2019. (Cited on pages 19 and 52.)
- [57] Corey Rae Harrington McRae, Haozhi Wang, Jiansong Gao, Michael Vissers, Teresa Brecht, Andrew Dunsworth, David Pappas, and Josh Mutus. Materials loss measurements using superconducting microwave resonators. *arXiv*, (1), jun 2020. (Cited on pages 19, 53, and 54.)
- [58] N. Daniilidis, S. Narayanan, S. A. Möller, R. Clark, T. E. Lee, P. J. Leek, A. Wallraff, St Schulz, F. Schmidt-Kaler, and H. Häffner. Fabrication and heating rate study of microscopic surface electrode ion traps. *New Journal of Physics*, 13(1):013032, jan 2011. (Cited on page 19.)
- [59] Abigail Shearrow, Gerwin Koolstra, Samuel J. Whiteley, Nathan Earnest, Peter S. Barry, F. Joseph Heremans, David D. Awschalom, Erik Shirokoff, and David I. Schuster. Atomic layer deposition of titanium nitride for quantum circuits. *Applied Physics Letters*, 113(21), 2018. (Cited on page 19.)
- [60] William D. Oliver and Paul B. Welander. Materials in superconducting quantum bits. *MRS Bulletin*, 38(10):816–825, 2013. (Cited on page 19.)
- [61] T. Lindström, J. E. Healey, M. S. Colclough, C. M. Muirhead, and A. Ya Tzalenchuk. Properties of superconducting planar resonators at millikelvin temperatures. *Physical Review B - Condensed Matter and Materials Physics*, 80(13):2–5, 2009. (Cited on page 19.)
- [62] C. R.H. McRae, R. E. Lake, J. L. Long, M. Bal, X. Wu, B. Jugdersuren, T. H. Metcalf, X. Liu, and D. P. Pappas. Dielectric loss extraction for superconducting microwave resonators. *arXiv*, 194003(May):6–11, 2019. (Cited on page 19.)
- [63] Jonas Zmuidzinis. Superconducting microresonators: Physics and applications. *Annual Review of Condensed Matter Physics*, 3(1):169–214, 2012. (Cited on page 19.)
- [64] Michael R. Vissers, Jeffrey S. Kline, Jiansong Gao, David S. Wisbey, and David P. Pappas. Reduced microwave loss in trenched superconducting coplanar waveguides. *Applied Physics Letters*, 100(8):082602, feb 2012. (Cited on page 19.)
- [65] A. Bruno, G. de Lange, S. Asaad, K. L. van der Enden, N. K. Langford, and L. DiCarlo. Reducing intrinsic loss in superconducting resonators by surface treatment and deep etching of silicon substrates. *Applied Physics Letters*, 106(18):1–4, may 2015. (Cited on page 19.)
- [66] G. Calusine, A. Melville, W. Woods, R. Das, C. Stull, V. Bolkhovsky, D. Braje, D. Hover, D. K. Kim, X. Miloshi, D. Rosenberg, A. Sevi, J. L. Yoder, E. Dauler, and W. D. Oliver. Analysis and mitigation of interface losses in trenched superconducting coplanar waveguide resonators. *Applied Physics Letters*, 112(6), 2018. (Cited on pages 19 and 20.)

- [67] W. Woods, G. Calusine, A. Melville, A. Sevi, E. Golden, D. K. Kim, D. Rosenberg, J. L. Yoder, and W. D. Oliver. Determining Interface Dielectric Losses in Superconducting Coplanar-Waveguide Resonators. *Physical Review Applied*, 12(1):1, 2019. (Cited on pages 19, 20, and 57.)
- [68] Ani Nersisyan, Stefano Poletto, Nasser Alidoust, Riccardo Manenti, Russ Renzas, Cat-Vu Bui, Kim Vu, Tyler Whyland, Yuvraj Mohan, Eyob A. Sete, Sam Stanwyck, Andrew Bestwick, and Matthew Reagor. Manufacturing low dissipation superconducting quantum processors. *arXiv preprint*, 94710, 2019. (Cited on pages 19, 20, 53, and 54.)
- [69] R. Barends, N. Verduyn, A. Endo, P. J. De Visser, T. Zijlstra, T. M. Klapwijk, P. Diener, S. J.C. Yates, and J. J.A. Baselmans. Minimal resonator loss for circuit quantum electrodynamics. *Applied Physics Letters*, 97(2):4–6, 2010. (Cited on page 19.)
- [70] K. Geerlings, S. Shankar, E. Edwards, L. Frunzio, R. J. Schoelkopf, and M. H. Devoret. Improving the quality factor of microwave compact resonators by optimizing their geometrical parameters. *Applied Physics Letters*, 100(19):8–10, may 2012. (Cited on page 19.)
- [71] Yirong Jin, Hui Deng, Xueyi Guo, Yarui Zheng, Keqiang Huang, Luhui Ning, and Dongning Zheng. High Quality Stepped-Impedance Resonators Suitable for Circuit-QED Measurement of Superconducting Artificial Atoms. *IEEE Transactions on Applied Superconductivity*, 27(4):1–1, 2017. (Cited on page 19.)
- [72] David Niepce, Jonathan J. Burnett, Martí Gutierrez Latorre, and Jonas Bylander. Geometric scaling of two-level-system loss in superconducting resonators. *Superconductor Science and Technology*, 33(2):025013, jan 2020. (Cited on page 19.)
- [73] Y. Chu, C. Axline, C. Wang, T. Brecht, Y. Y. Gao, L. Frunzio, and R. J. Schoelkopf. Suspending superconducting qubits by silicon micromachining. *Applied Physics Letters*, 109(11), 2016. (Cited on page 19.)
- [74] C. Wang, C. Axline, Y. Y. Gao, T. Brecht, Y. Chu, L. Frunzio, M. H. Devoret, and R. J. Schoelkopf. Surface participation and dielectric loss in superconducting qubits. *Applied Physics Letters*, 107(16), 2015. (Cited on pages 20, 54, and 57.)
- [75] Oliver Dial, Douglas T. McClure, Stefano Poletto, Jay M. Gambetta, David W. Abraham, Jerry M. Chow, Matthias Steffen, G A Keefe, Mary Beth Rothwell, Jay M. Gambetta, David W. Abraham, Jerry M. Chow, and Steffen Matthias. Bulk and surface loss in superconducting transmon qubits. *Superconductor Science and Technology*, 29(4):44001, 2016. (Cited on page 20.)
- [76] Hanhee Paik, D. I. Schuster, Lev S. Bishop, G. Kirchmair, G. Catelani, A. P. Sears, B. R. Johnson, M. J. Reagor, L. Frunzio, L. I. Glazman, S. M. Girvin, M. H. Devoret, and R. J. Schoelkopf. Observation of high coherence in Josephson junction qubits

- measured in a three-dimensional circuit QED architecture. *Physical Review Letters*, 107(24):1–5, 2011. (Cited on page 20.)
- [77] R. Zhao, S. Park, T. Zhao, M. Bal, C. R.H. McRae, J. Long, and D. P. Pappas. Merged-Element Transmon. *Physical Review Applied*, 14(6):1, 2020. (Cited on page 20.)
- [78] H. J. Mamin, E. Huang, S. Carnevale, C. T. Rettner, N. Arellano, M. H. Sherwood, C. Kurter, B. Trimm, M. Sandberg, R. M. Shelby, M. A. Mueed, B. A. Madon, A. Pushp, M. Steffen, and D. Rugar. Merged-Element Transmons: Design and Qubit Performance. pages 1–7, 2021. (Cited on page 20.)
- [79] Jiansong Gao, Miguel Daal, Anastasios Vayonakis, Shwetank Kumar, Jonas Zmuidzinas, Bernard Sadoulet, Benjamin A. Mazin, Peter K. Day, and Henry G. Leduc. Experimental evidence for a surface distribution of two-level systems in superconducting lithographed microwave resonators. *Applied Physics Letters*, 92(15), 2008. (Cited on page 20.)
- [80] Jürgen Lisenfeld, Alexander Bilmes, Anthony Megrant, Rami Barends, Julian Kelly, Paul Klimov, Georg Weiss, John M. Martinis, and Alexey V. Ustinov. Electric field spectroscopy of material defects in transmon qubits. *npj Quantum Information*, 5(1):1–6, 2019. (Cited on pages 20 and 52.)
- [81] Alexander Bilmes, Anthony Megrant, Paul Klimov, Georg Weiss, John M. Martinis, Alexey V. Ustinov, and Jürgen Lisenfeld. Resolving the positions of defects in superconducting quantum bits. *Scientific Reports*, 10(1):1–6, 2020. (Cited on pages 20 and 53.)
- [82] L J Zeng, S Nik, T Greibe, P Krantz, C M Wilson, P Delsing, and E Olsson. Direct observation of the thickness distribution of ultra thin AlO_x barriers in Al/AlO_x/Al Josephson junctions. *Journal of Physics D: Applied Physics*, 48(39):395308, oct 2015. (Cited on pages 20, 23, 27, 42, and 47.)
- [83] M. Virginia P. Altoé, Archan Banerjee, Cassidy Berk, Ahmed Hajr, Adam Schwartzberg, Chengyu Song, Mohammed Al Ghadeer, Shaul Aloni, Michael J. Elowson, John Mark Kreikebaum, Ed K. Wong, Sinead Griffin, Saleem Rao, Alexander Weber-Bargioni, Andrew M. Minor, David I. Santiago, Stefano Cabrini, Irfan Siddiqi, and D. Frank Ogletree. Localization and reduction of superconducting quantum coherent circuit losses. *arXiv preprint*, pages 1–20, dec 2020. (Cited on pages 20 and 53.)
- [84] Lukas Grünhaupt, Uwe von Lüpke, Daria Gusenkova, Sebastian T. Skacel, Nataliya Maleeva, Steffen Schlör, Alexander Bilmes, Hannes Rotzinger, Alexey V. Ustinov, Martin Weides, and Ioan M. Pop. An argon ion beam milling process for native AlO_x layers enabling coherent superconducting contacts. pages 1–9, 2017. (Cited on page 20.)
- [85] A. Dunsworth, A. Megrant, C. Quintana, Zijun Chen, R. Barends, B. Burkett, B. Foxen, Yu Chen, B. Chiaro, A. Fowler, R. Graff, E. Jeffrey, J. Kelly, E. Lucero, J. Y. Mutus, M. Neeley, C. Neill, P. Roushan, D. Sank, A. Vainsencher, J. Wenner, T. C. White,

- and John M. Martinis. Characterization and reduction of capacitive loss induced by sub-micron Josephson junction fabrication in superconducting qubits. *Applied Physics Letters*, 111(2), 2017. (Cited on page 20.)
- [86] A. Osman, J. Simon, A. Bengtsson, S. Kosen, P. Krantz, D. P. Lozano, M. Scigliuzzo, P. Delsing, Jonas Bylander, and A. Fadavi Roudsari. Simplified Josephson-junction fabrication process for reproducibly high-performance superconducting qubits. *Applied Physics Letters*, 118(6):064002, feb 2021. (Cited on page 20.)
- [87] Jonathan Burnett, Andreas Bengtsson, David Niepce, and Jonas Bylander. Noise and loss of superconducting aluminium resonators at single photon energies. *Journal of Physics: Conference Series*, 969:012131, mar 2018. (Cited on page 20.)
- [88] J. Bardeen, L. N. Cooper, and J. R. Schrieffer. Theory of superconductivity. *Phys. Rev.*, 108:1175–1204, Dec 1957. (Cited on page 20.)
- [89] John M. Martinis. Course 13 Superconducting Qubits and the Physics of Josephson Junctions. In *Les Houches Summer School Proceedings*, volume 79, pages 487–520. 2004. (Cited on pages 20, 22, and 23.)
- [90] Kyle Serniak. Nonequilibrium Quasiparticles in Superconducting Qubits. *Thesis*, 2019. (Cited on pages 22, 56, and 57.)
- [91] N Cabrera and N F Mott. Theory of the oxidation of metals. *Reports on Progress in Physics*, 12(1):308, jan 1949. (Cited on page 23.)
- [92] A. Atkinson. Transport processes during the growth of oxide films at elevated temperature. *Reviews of Modern Physics*, 57(2):437–470, 1985. (Cited on page 23.)
- [93] B. E. Hayden, W. Wyrobisch, W. Oppermann, S. Hachicha, P. Hofmann, and A. M. Bradshaw. The interaction of oxygen with aluminium: Mainly ellipsometric aspects. *Surface Science*, 109(1):207–220, 1981. (Cited on page 23.)
- [94] L. P.H. Jeurgens, W. G. Sloof, F. D. Tichelaar, and E. J. Mittemeijer. Growth kinetics and mechanisms of aluminum-oxide films formed by thermal oxidation of aluminum. *Journal of Applied Physics*, 92(3):1649–1656, 2002. (Cited on page 23.)
- [95] Xinjie Kang, Liliang Ying, Hai Wang, Guofeng Zhang, Wei Peng, Xiangyan Kong, Xiaoming Xie, and Zhen Wang. Measurements of tunneling barrier thicknesses for Nb/Al-AlOx/Nb tunnel junctions. *Physica C: Superconductivity and its Applications*, 503:29–32, 2014. (Cited on pages 23, 42, and 47.)
- [96] Jürgen Gorobez, Björn Maack, and Niklas Nilus. Growth of Self-Passivating Oxide Layers on Aluminum—Pressure and Temperature Dependence. *Physica Status Solidi (B) Basic Research*, page 2000559, jan 2021. (Cited on pages 23, 25, 42, and 47.)

- [97] R. Stratton. Volt-current characteristics for tunneling through insulating films. *Journal of Physics and Chemistry of Solids*, 23(9):1177–1190, 1962. (Cited on page 26.)
- [98] John G. Simmons. Generalized Formula for the Electric Tunnel Effect between Similar Electrodes Separated by a Thin Insulating Film. *Journal of Applied Physics*, 34(6):1793–1803, 1963. (Cited on pages 26, 27, and 42.)
- [99] M. E. Paramonov, L. V. Filippenko, P. N. Dmitriev, M. Yu Fominsky, and V. P. Koshelets. Determination of the Parameters of Tunneling Barriers of Superconducting Tunnel Structures for Submillimeter Receivers. *Journal of Communications Technology and Electronics*, 64(10):1144–1148, 2019. (Cited on page 27.)
- [100] Chang Eun Kim, Keith G. Ray, and Vincenzo Lordi. A density-functional theory study of the Al/AlO_x/Al tunnel junction. *Journal of Applied Physics*, 128(15), 2020. (Cited on pages 27 and 46.)
- [101] Vinay Ambegaokar and Alexis Baratoff. Tunneling Between Superconductors. *Physical Review Letters*, 10(11):486–489, jun 1963. (Cited on page 27.)
- [102] Charles R. Hicks and Kenneth V. Turner Jr. *Fundamental Concepts in the Design of Experiments*. Oxford University Press, New York, 5 edition, 1999. (Cited on page 28.)
- [103] G. J. Dolan. Offset masks for lift-off photoprocessing. *Applied Physics Letters*, 31(5):337–339, 1977. (Cited on page 31.)
- [104] A. Potts, G. J. Parker, J. J. Baumberg, and P. A.J. De Groot. CMOS compatible fabrication methods for submicron Josephson junction qubits. *IEE Proceedings: Science, Measurement and Technology*, 148(5):225–228, 2001. (Cited on pages 31 and 36.)
- [105] Marius V. Costache, Germàn Bridoux, Ingmar Neumann, and Sergio O. Valenzuela. Lateral metallic devices made by a multiangle shadow evaporation technique. *Journal of Vacuum Science and Technology B, Nanotechnology and Microelectronics: Materials, Processing, Measurement, and Phenomena*, 30(4):04E105, 2012. (Cited on pages 31 and 36.)
- [106] Ke Zhang, Meng Meng Li, Qiang Liu, Hai Feng Yu, and Yang Yu. Bridge-free fabrication process for Al/AlO_x/Al Josephson junctions. *Chinese Physics B*, 26(7), 2017. (Cited on pages 31 and 36.)
- [107] J. M. Kreikebaum, K P O’Brien, A Morvan, and I. Siddiqi. Improving wafer-scale Josephson junction resistance variation in superconducting quantum coherent circuits. *Superconductor Science and Technology*, 33(6):06LT02, jun 2020. (Cited on page 38.)
- [108] Anjali Premkumar, Conan Weiland, Sooyeon Hwang, Berthold Jaeck, Alexander P. M. Place, Iradwikanari Waluyo, Adrian Hunt, Valentina Bisogni, Jonathan Pellicciari, Andi Barbour, Mike S. Miller, Paola Russo, Fernando Camino, Kim Kisslinger, Xiao Tong,

- Mark S. Hybertsen, Andrew A. Houck, and Ignace Jarrige. Microscopic Relaxation Channels in Materials for Superconducting Qubits. apr 2020. (Cited on page 38.)
- [109] K.R. Williams, Kishan Gupta, and Matthew Wasilik. Etch rates for micromachining processing-part II. *Journal of Microelectromechanical Systems*, 12(6):761–778, dec 2003. (Cited on page 40.)
- [110] R. Vijay, M. H. Devoret, and I. Siddiqi. Invited Review Article: The Josephson bifurcation amplifier. *Review of Scientific Instruments*, 80(11):111101, nov 2009. (Cited on page 42.)
- [111] D H Slichter. Quantum Jumps and Measurement Backaction in a Superconducting Qubit by Daniel Huber Slichter. *Thesis*, 2011. (Cited on page 42.)
- [112] Chris Macklin, K O’Brien, D Hover, M. E. Schwartz, V Bolkhovskiy, X Zhang, W. D. Oliver, and I Siddiqi. A near – quantum-limited Josephson traveling-wave parametric amplifier. *Science*, 350(6258):307, 2015. (Cited on page 42.)
- [113] J. T. Monroe, D. Kowsari, K. Zheng, C. Gaikwad, J. Brewster, D. S. Wisbey, and K. W. Murch. Optical Direct Write of Dolan–Niemeyer-Bridge Junctions for Transmon Qubits. 1:1–6, 2021. (Cited on page 43.)
- [114] Filipp Mueller, Raymond N. Schouten, Matthias Brauns, Tian Gang, Wee Han Lim, Nai Shyan Lai, Andrew S. Dzurak, Wilfred G. van der Wiel, and Floris A. Zwanenburg. Printed circuit board metal powder filters for low electron temperatures. *Review of Scientific Instruments*, 84(4):044706, apr 2013. (Cited on page 50.)
- [115] W. A. Phillips. Two-level states in glasses. *Reports on Progress in Physics*, 50(12):1657–1708, 1987. (Cited on page 51.)
- [116] Clemens Müller, Jared H. Cole, and Jürgen Lisenfeld. Towards understanding two-level-systems in amorphous solids - Insights from quantum circuits. pages 1–34, 2017. (Cited on pages 51, 53, and 54.)
- [117] L. J. Zeng, P. Krantz, S. Nik, P. Delsing, and E. Olsson. The atomic details of the interfacial interaction between the bottom electrode of Al/AlO_x/Al Josephson junctions and HF-treated Si substrates. *Journal of Applied Physics*, 117(16), 2015. (Cited on page 53.)
- [118] Andrew J. Keller, Paul B. Dieterle, Michael Fang, Brett Berger, Johannes M. Fink, and Oskar Painter. Al transmon qubits on silicon-on-insulator for quantum device integration. *Applied Physics Letters*, 111(4), 2017. (Cited on page 53.)
- [119] Q.S. Shu, K. Gendreau, W. Hartung, J. Kirchgessner, D Moffat, R Noer, H Padamsee, D.L. Rubin, and J Sears. Influence of condensed gases on field emission and the performance of superconducting RF cavities. *IEEE Transactions on Magnetics*, 25(2):1868–1872, mar 1989. (Cited on page 55.)

- [120] R. L. Geng and H. Padamsee. Condensation/adsorption and evacuation of residual gases in the SRF system for the CESR luminosity upgrade. *Proceedings of the IEEE Particle Accelerator Conference*, 2:983–985, 1999. (Cited on page 55.)
- [121] J. M. Vogt, O. Kugeler, and J. Knobloch. Impact of cool-down conditions at T_c on the superconducting rf cavity quality factor. *Physical Review Special Topics - Accelerators and Beams*, 16(10):1–8, 2013. (Cited on page 55.)
- [122] Christopher James Axline. Building Blocks for Modular Circuit QED Quantum Computing. *Thesis*, page 285, 2018. (Cited on pages 55, 56, and 57.)
- [123] John M. Martinis and A. Megrant. UCSB final report for the CSQ program: Review of decoherence and materials physics for superconducting qubits. oct 2014. (Cited on page 56.)
- [124] M. Lenander, H. Wang, Radoslaw C. Bialczak, Erik Lucero, Matteo Mariantoni, M. Neeley, A. D. O’Connell, D. Sank, M. Weides, J. Wenner, T. Yamamoto, Y. Yin, J. Zhao, A. N. Cleland, and John M. Martinis. Measurement of energy decay in superconducting qubits from nonequilibrium quasiparticles. *Physical Review B - Condensed Matter and Materials Physics*, 84(2):1–10, 2011. (Cited on page 56.)
- [125] G. Catelani, S. E. Nigg, S. M. Girvin, R. J. Schoelkopf, and L. I. Glazman. Decoherence of superconducting qubits caused by quasiparticle tunneling. *Physical Review B - Condensed Matter and Materials Physics*, 86(18):1–17, 2012. (Cited on page 56.)
- [126] E. M. Levenson-Falk, F. Kos, R. Vijay, L. Glazman, and I. Siddiqi. Single-quasiparticle trapping in aluminum nanobridge josephson junctions. *Physical Review Letters*, 112(4):1–5, 2014. (Cited on page 56.)
- [127] K. Serniak, S. Diamond, M. Hays, V. Fatemi, S. Shankar, L. Frunzio, R. J. Schoelkopf, and M. H. Devoret. Direct Dispersive Monitoring of Charge Parity in Offset-Charge-Sensitive Transmons. *Physical Review Applied*, 12(1):1, 2019. (Cited on page 56.)
- [128] R. Barends, J. Wenner, M. Lenander, Y. Chen, R. C. Bialczak, J. Kelly, E. Lucero, P. O’Malley, M. Mariantoni, D. Sank, H. Wang, T. C. White, Y. Yin, J. Zhao, A. N. Cleland, John M. Martinis, and J. J. A. Baselmans. Minimizing quasiparticle generation from stray infrared light in superconducting quantum circuits. *Applied Physics Letters*, 99(11):113507, sep 2011. (Cited on page 57.)
- [129] Antonio D. Córcoles, Jerry M. Chow, Jay M. Gambetta, Chad Rigetti, J. R. Rozen, George A. Keefe, Mary Beth Rothwell, Mark B. Ketchen, and M. Steffen. Protecting superconducting qubits from radiation. *Applied Physics Letters*, 99(18):1–3, 2011. (Cited on page 57.)
- [130] J. M. Kreikebaum, A. Dove, W. Livingston, E. Kim, and I. Siddiqi. Optimization of infrared and magnetic shielding of superconducting TiN and Al coplanar microwave resonators. *Superconductor Science and Technology*, 29(10), 2016. (Cited on page 57.)

- [131] E. J. Wollack, D. J. Fixsen, R. Henry, A. Kogut, M. Limon, and P. Mirel. Electromagnetic and thermal properties of a conductively loaded epoxy. *International Journal of Infrared and Millimeter Waves*, 29(1):51–61, 2008. (Cited on page 57.)
- [132] Z. Kim, B. Suri, V. Zaretsky, S. Novikov, K. D. Osborn, A. Mizel, F. C. Wellstood, and B. S. Palmer. Decoupling a Cooper-pair box to enhance the lifetime to 0.2 ms. *Physical Review Letters*, 106(12):1–4, 2011. (Cited on page 57.)
- [133] Chad Rigetti, Jay M. Gambetta, Stefano Poletto, B. L.T. Plourde, Jerry M. Chow, A. D. Córcoles, John A. Smolin, Seth T. Merkel, J. R. Rozen, George A. Keefe, Mary B. Rothwell, Mark B. Ketchen, and M. Steffen. Superconducting qubit in a waveguide cavity with a coherence time approaching 0.1 ms. *Physical Review B - Condensed Matter and Materials Physics*, 86(10):1–5, 2012. (Cited on page 57.)
- [134] K. W. Murch, S. J. Weber, E. M. Levenson-Falk, R. Vijay, and I. Siddiqi. $1/f$ noise of Josephson-junction-embedded microwave resonators at single photon energies and millikelvin temperatures. *Applied Physics Letters*, 100(14):142601, apr 2012. (Cited on page 57.)
- [135] Jerzy Krupka, Jonathan Breeze, Neil McN. Alford, Anthony E. Centeno, Leif Jensen, and Thomas Claussen. Measurements of Permittivity and Dielectric Loss Tangent of High Resistivity Float Zone Silicon at Microwave Frequencies. In *2006 International Conference on Microwaves, Radar and Wireless Communications*, volume 54, pages 1097–1100. IEEE, may 2006. (Cited on page 57.)
- [136] Cameron J. Kopas, Justin Gonzales, Shengke Zhang, Daniel R. Queen, Brian Wagner, Mac Robinson, James Huffman, and Nate Newman. Low microwave loss in deposited Si and Ge thin-film dielectrics at near single-photon power and low temperatures. *Journal of Chemical Information and Modeling*, 53(9):1689–1699, nov 2020. (Cited on page 57.)
- [137] V. B. Braginsky, V. S. Ilchenko, and Kh S. Bagdassarov. Experimental observation of fundamental microwave absorption in high-quality dielectric crystals. *Physics Letters A*, 120(6):300–305, 1987. (Cited on page 57.)
- [138] Archana Kamal, Jonilyn L. Yoder, Fei Yan, Theodore J. Gudmundsen, David Hover, Adam P. Sears, Paul Welandar, Terry P. Orlando, Simon Gustavsson, and William D. Oliver. Improved superconducting qubit coherence with high-temperature substrate annealing. jun 2016. (Cited on page 57.)
- [139] Z. K. Mineev, I. M. Pop, and M. H. Devoret. Planar superconducting whispering gallery mode resonators. *Applied Physics Letters*, 103(14):1–4, 2013. (Cited on page 57.)
- [140] Chunqing Deng, M. Otto, and A. Lupascu. Characterization of low-temperature microwave loss of thin aluminum oxide formed by plasma oxidation. *Applied Physics Letters*, 104(4):2012–2015, 2014. (Cited on page 57.)

- [141] Aaron D. O’Connell, M. Ansmann, R. C. Bialczak, M. Hofheinz, N. Katz, Erik Lucero, C. McKenney, M. Neeley, H. Wang, E. M. Weig, A. N. Cleland, and J. M. Martinis. Microwave dielectric loss at single photon energies and millikelvin temperatures. *Applied Physics Letters*, 92(11):1–4, 2008. (Cited on page 57.)
- [142] Ligo Collaboration. Enhanced sensitivity of the LIGO gravitational wave detector by using squeezed states of light. *Nature Photonics*, 7:613–619, 2013. (Cited on page 58.)
- [143] C. L. Degen, F. Reinhard, and P. Cappellaro. Quantum sensing. *Reviews of Modern Physics*, 89(3):1–39, 2017. (Cited on page 58.)
- [144] Carlton M. Caves. Quantum limits on noise in linear amplifiers. *Physical Review D*, 26(8):1817–1839, 1982. (Cited on page 58.)
- [145] A. A. Clerk, M. H. Devoret, S. M. Girvin, Florian Marquardt, and R. J. Schoelkopf. Introduction to quantum noise, measurement, and amplification. *Reviews of Modern Physics*, 82(2):1155–1208, 2010. (Cited on page 58.)
- [146] W. Heisenberg. Über den anschaulichen Inhalt der quantentheoretischen Kinematik und Mechanik. *Zeitschrift für Physik*, 43(3-4):172–198, 1927. (Cited on page 58.)
- [147] H. P. Robertson. The Uncertainty Principle. *Physical Review*, 34(1):163–164, jul 1929. (Cited on page 58.)
- [148] David Deutsch. Uncertainty in quantum measurements. *Physical Review Letters*, 50(9):631–633, 1983. (Cited on pages 59, 60, and 65.)
- [149] Iwo Białynicki-Birula and Łukasz Rudnicki. Entropic Uncertainty Relations in Quantum Physics. In *Statistical Complexity*, pages 1–34. Springer Netherlands, Dordrecht, 2011. (Cited on page 59.)
- [150] Y. Fukuda, T. Hayakawa, E. Ichihara, K. Inoue, K. Ishihara, H. Ishino, Y. Itow, T. Kajita, J. Kameda, S. Kasuga, K. Kobayashi, Y. Kobayashi, Y. Koshio, M. Miura, Masayuki Nakahata, S. Nakayama, A. Okada, K. Okumura, N. Sakurai, M. Shiozawa, Y. Suzuki, Y. Takeuchi, Y. Totsuka, S. Yamada, M. Earl, A. Habig, E. Kearns, M. D. Messier, K. Scholberg, J. L. Stone, L. R. Sulak, C. W. Walter, M. Goldhaber, T. Barszczak, D. Casper, W. Gajewski, P. G. Halverson, J. Hsu, W. R. Kropp, L. R. Price, F. Reines, M. Smy, H. W. Sobel, M. R. Vagins, K. S. Ganezer, W. E. Keig, R. W. Ellsworth, S. Tasaka, J. W. Flanagan, A. Kibayashi, J. G. Learned, S. Matsuno, V. J. Stenger, D. Takemori, T. Ishii, J. Kanzaki, T. Kobayashi, S. Mine, K. Nakamura, K. Nishikawa, Y. Oyama, A. Sakai, M. Sakuda, O. Sasaki, S. Echigo, M. Kohama, A. T. Suzuki, T. J. Haines, E. Blaufuss, B. K. Kim, R. Sanford, R. Svoboda, M. L. Chen, Z. Conner, J. A. Goodman, G. W. Sullivan, J. Hill, C. K. Jung, K. Martens, C. Mauger, C. McGrew, E. Sharkey, B. Viren, C. Yanagisawa, W. Doki, K. Miyano, H. Okazawa, C. Saji, M. Takahata, Y. Nagashima, M. Takita, T. Yamaguchi, M. Yoshida, S. B. Kim, M. Etoh, K. Fujita, A. Hasegawa, T. Hasegawa, S. Hatakeyama, T. Iwamoto, M. Koga,

- T. Maruyama, H. Ogawa, J. Shirai, A. Suzuki, F. Tsushima, M. Koshihara, M. Nemoto, K. Nishijima, T. Futagami, Y. Hayato, Y. Kanaya, K. Kaneyuki, Y. Watanabe, D. Kielczewska, R. A. Doyle, J. S. George, A. L. Stachyra, L. L. Wai, R. J. Wilkes, and K. K. Young. Evidence for Oscillation of Atmospheric Neutrinos. *Physical Review Letters*, 81(8):1562–1567, aug 1998. (Cited on page 59.)
- [151] Patrick J. Coles and Marco Piani. Complementary sequential measurements generate entanglement. *Physical Review A - Atomic, Molecular, and Optical Physics*, 89(1):1–5, 2014. (Cited on page 59.)
- [152] Marco Tomamichel. A Framework for Non-Asymptotic Quantum Information Theory. *Thesis*, (20213), 2012. (Cited on pages 60, 61, and 67.)
- [153] Patrick J. Coles, Mario Berta, Marco Tomamichel, and Stephanie Wehner. Entropic uncertainty relations and their applications. *Reviews of Modern Physics*, 89(1), 2017. (Cited on pages 60, 61, and 62.)
- [154] Hans Maassen and J. B M Uffink. Generalized entropic uncertainty relations. *Physical Review Letters*, 60(12):1103–1106, 1988. (Cited on pages 61 and 66.)
- [155] Chuan Feng Li, Jin Shi Xu, Xiao Ye Xu, Ke Li, and Guang Can Guo. Experimental investigation of the entanglement-assisted entropic uncertainty principle. *Nature Physics*, 7(10):752–756, 2011. (Cited on page 62.)
- [156] Robert Prevedel, Deny R. Hamel, Roger Colbeck, Kent Fisher, and Kevin J. Resch. Experimental investigation of the uncertainty principle in the presence of quantum memory and its application to witnessing entanglement. *Nature Physics*, 7(10):757–761, 2011. (Cited on page 62.)
- [157] Jian Xing, Yu-Ran Zhang, Shang Liu, Yan-Chun Chang, Jie-Dong Yue, Heng Fan, and Xin-Yu Pan. Experimental investigation of quantum entropic uncertainty relations for multiple measurements in pure diamond. *Scientific Reports*, 7(1):2563, dec 2017. (Cited on page 62.)
- [158] Lee A. Rozema, Ardavan Darabi, Dylan H. Mahler, Alex Hayat, Yasaman Soudagar, and Aephraim M. Steinberg. Violation of Heisenberg’s measurement-disturbance relationship by weak measurements. *Physical Review Letters*, 109(10):1–5, 2012. (Cited on page 62.)
- [159] I. I. Hirschman. A Note on Entropy. *American Journal of Mathematics*, 79(1):152, jan 1957. (Cited on page 64.)
- [160] Nicole Yunger Halpern. Jarzynski-like equality for the out-of-time-ordered correlator. *Physical Review A*, 95(1):1–9, 2017. (Cited on pages 67 and 68.)
- [161] M Krishna and K R Parthasarathy. An Entropic Uncertainty Principle for Quantum Measurements. *arXiv*, oct 2001. (Cited on page 67.)

- [162] Nicole Yunger Halpern, Anthony Bartolotta, and Jason Pollack. Entropic uncertainty relations for quantum information scrambling. *Communications Physics*, 2(1):92, dec 2019. (Cited on page 69.)
- [163] Jonathan T. Monroe, Nicole Yunger Halpern, Taeho Lee, and Kater W. Murch. Weak Measurement of a Superconducting Qubit Reconciles Incompatible Operators. *Physical Review Letters*, 126(10):100403, mar 2021. (Cited on page 70.)
- [164] Y. Aharonov and L. Vaidman. Aharonov and Vaidman reply. *Physical Review Letters*, 62(19):2327–2327, may 1989. (Cited on page 83.)
- [165] Sreenath K. Manikandan, Cyril Elouard, and Andrew N. Jordan. Fluctuation theorems for continuous quantum measurements and absolute irreversibility. *Physical Review A*, 99(2):022117, feb 2019. (Cited on page 89.)
- [166] Robert Alicki, David Gelbwaser-Klimovsky, and Gershon Kurizski. Periodically driven quantum open systems: Tutorial. *arXiv*, (1):1–6, may 2012. (Cited on page 89.)
- [167] Michele Campisi, Peter Hänggi, and Peter Talkner. Colloquium: Quantum fluctuation relations: Foundations and applications. *Reviews of Modern Physics*, 83(3):771–791, 2011. (Cited on page 89.)
- [168] Patrice A. Camati and Roberto M. Serra. Verifying detailed fluctuation relations for discrete feedback-controlled quantum dynamics. *Physical Review A*, 97(4), 2018. (Cited on page 89.)
- [169] Luca Mancino, Vasco Cavina, Antonella De Pasquale, Marco Sbroscia, Robert I. Booth, Emanuele Rocca, Ilaria Gianani, Vittorio Giovannetti, and Marco Barbieri. Geometrical Bounds on Irreversibility in Open Quantum Systems. *Physical Review Letters*, 121(16):160602, oct 2018. (Cited on page 89.)
- [170] Zoë Holmes, Sebastian Weidt, David Jennings, Janet Anders, and Florian Mintert. Coherent fluctuation relations: from the abstract to the concrete. *Quantum*, 3:124, feb 2019. (Cited on page 89.)
- [171] Denis J. Evans and Debra J. Searles. Equilibrium microstates which generate second law violating steady states. *Physical Review E*, 50(2):1645–1648, aug 1994. (Cited on page 90.)
- [172] Joel L Lebowitz. Boltzmann’s Entropy and Time’s Arrow. *Physics Today*, 46(9):32–38, sep 1993. (Cited on pages 90 and 95.)
- [173] Michele Campisi and Peter Hanggi. Fluctuation, dissipation and the arrow of time. *Entropy*, 13(12):2024–2035, 2011. (Cited on pages 90 and 95.)
- [174] E M Sevick, R Prabhakar, S R Williams, and D J Searles. Fluctuation theorems. *Annual Review of Physical Chemistry*, 59:603–633, 2008. (Cited on page 90.)

- [175] Sebastian Deffner. Nonequilibrium entropy production in open and closed quantum systems. *Thesis*, 2011. (Cited on page 90.)
- [176] Raam Uzdin. Additional energy-information relations in thermodynamics of small systems. *Physical Review E*, 96(3):032128, sep 2017. (Cited on page 90.)
- [177] G. M. Wang, E. M. Sevick, Emil Mittag, Debra J. Searles, and Denis J. Evans. Experimental Demonstration of Violations of the Second Law of Thermodynamics for Small Systems and Short Time Scales. *Physical Review Letters*, 89(5):1–4, 2002. (Cited on page 90.)
- [178] D. M. Carberry, J. C. Reid, G. M. Wang, E. M. Sevick, Debra J. Searles, and Denis J. Evans. Fluctuations and irreversibility: An experimental demonstration of a second-law-like theorem using a colloidal particle held in an optical trap. *Physical Review Letters*, 92(14):1–4, 2004. (Cited on page 90.)
- [179] Thomas Risler, Aurélien Peilloux, and Jacques Prost. Homeostatic Fluctuations of a Tissue Surface. *Physical Review Letters*, 115(25):258104, dec 2015. (Cited on page 90.)
- [180] Arben Kalziqi, David Yanni, Jacob Thomas, Siu Lung Ng, Skanda Vivek, Brian K. Hammer, and Peter J. Yunker. Immobile Active Matter: Activity from Death and Reproduction. *Physical Review Letters*, 120(1):18101, 2018. (Cited on page 90.)
- [181] Andrea Hofmann, Ville F. Maisi, Julien Basset, Christian Reichl, Werner Wegscheider, Thomas Ihn, Klaus Ensslin, and Christopher Jarzynski. Heat dissipation and fluctuations in a driven quantum dot. *physica status solidi (b)*, 254(3):1600546, mar 2017. (Cited on page 90.)
- [182] M Brunelli, L Fusco, R Landig, W Wiczorek, J. Hoelscher-Obermaier, G Landi, F L Semião, A Ferraro, N Kiesel, T Donner, G. De Chiara, and M Paternostro. Experimental Determination of Irreversible Entropy Production in out-of-Equilibrium Mesoscopic Quantum Systems. *Physical Review Letters*, 121(16):160604, 2018. (Cited on page 90.)
- [183] P. M. Harrington, D. Tan, M. Naghiloo, and K. W. Murch. Characterizing a Statistical Arrow of Time in Quantum Measurement Dynamics. *Physical Review Letters*, 123(2):020502, jul 2019. (Cited on pages 90, 97, 103, and 104.)
- [184] C Van Den Broeck. *Stochastic thermodynamics: a brief introduction*. 2013. (Cited on pages 90 and 93.)
- [185] Udo Seifert. Entropy production along a stochastic trajectory and an integral fluctuation theorem. *Physical Review Letters*, 95(4):1–4, 2005. (Cited on pages 92 and 94.)
- [186] Udo Seifert. Stochastic thermodynamics, fluctuation theorems and molecular machines. *Reports on Progress in Physics*, 75(12), 2012. (Cited on pages 92 and 94.)

- [187] Gavin E Crooks. Excursions in Statistical Dynamics. *Thesis*, page 117, 1999. (Cited on page 93.)
- [188] Matteo Smerlak. Stochastic thermodynamics of entropic transport. *arXiv*, 2:3, jul 2012. (Cited on page 94.)
- [189] Denis Evans. *Fundamentals of Classical Statistical Thermodynamics*. Wiley-VCH Verlag GmbH and Co. KGaA, Weinheim, Germany, jul 2016. (Cited on page 94.)
- [190] Benjamin Hertz Shargel. The measure-theoretic identity underlying transient fluctuation theorems. *Journal of Physics A: Mathematical and Theoretical*, 43(13):135002, apr 2010. (Cited on page 94.)
- [191] Fernando Brandão, Michał Horodecki, Nelly Ng, Jonathan Oppenheim, and Stephanie Wehner. The second laws of quantum thermodynamics. *Proceedings of the National Academy of Sciences*, 112(11):3275–3279, mar 2015. (Cited on page 95.)
- [192] Anthony Bartolotta, Sean M. Carroll, Stefan Leichenauer, and Jason Pollack. Bayesian second law of thermodynamics. *Physical Review E*, 94(2):1–19, 2016. (Cited on page 95.)
- [193] Takahiro Sagawa and Masahito Ueda. Second law of thermodynamics with discrete quantum feedback control. *Physical Review Letters*, 100(8):1–4, 2008. (Cited on page 96.)
- [194] Takahiro Sagawa and Masahito Ueda. Generalized Jarzynski equality under nonequilibrium feedback control. *Physical Review Letters*, 104(9):1–4, 2010. (Cited on page 96.)
- [195] Christopher W. Wächtler, Philipp Strasberg, and Tobias Brandes. Stochastic thermodynamics based on incomplete information: generalized Jarzynski equality with measurement errors with or without feedback. *New Journal of Physics*, 18(11):113042, nov 2016. (Cited on page 96.)
- [196] Justin Dressel, Areeya Chantasri, Andrew N. Jordan, and Alexander N. Korotkov. Arrow of Time for Continuous Quantum Measurement. *Physical Review Letters*, 119(22):220507, dec 2017. (Cited on pages 97, 101, and 103.)
- [197] Álvaro M. Alhambra, Lluís Masanes, Jonathan Oppenheim, and Christopher Perry. Fluctuating work: From quantum thermodynamical identities to a second law equality. *Physical Review X*, 6(4):1–14, 2016. (Cited on page 98.)
- [198] Johan Åberg. Fully Quantum Fluctuation Theorems. *Physical Review X*, 8(1):11019, 2018. (Cited on page 98.)
- [199] Alexander N. Korotkov. Quantum Bayesian approach to circuit QED measurement with moderate bandwidth. *Physical Review A - Atomic, Molecular, and Optical Physics*, 94(4), 2016. (Cited on page 100.)

- [200] Denis J. Evans and Debra J. Searles. Causality, response theory, and the second law of thermodynamics. *Physical Review E*, 53(6):5808–5815, 1996. (Cited on page 107.)
- [201] John F. Donoghue and Gabriel Menezes. Quantum causality and the arrows of time and thermodynamics. *Progress in Particle and Nuclear Physics*, 115:103812, nov 2020. (Cited on page 107.)
- [202] Sang Wook Kim, Takahiro Sagawa, Simone De Liberato, and Masahito Ueda. Quantum szilard engine. *Physical Review Letters*, 106(7):7–9, 2011. (Cited on page 107.)
- [203] David Felce and Vlatko Vedral. Quantum Refrigeration with Indefinite Causal Order. *Physical Review Letters*, 125(7):70603, 2020. (Cited on page 107.)
- [204] Leo Szilard. On the decrease of entropy in a thermodynamic system by the intervention of intelligent beings. *Behavioral Science*, 9(4):301–310, 1964. (Cited on page 107.)